Spinor Bose-Einstein Comagnetometer and Interhyperfine Interactions in ^{87}Rb

Pau Gómez Kabelka

A thesis submitted for the degree of Doctor of Philosophy

ICFO - The Institute of Photonic Sciences
UPC - Universitat Politècnica de Catalunya

Thesis Advisor: Prof. Dr. Morgan W. Mitchell

July, 2021

Spinor Bose-Einstein Comagnetometer and Interhyperfine Interactions in ^{87}Rb

... to my grandparents
Omi & Opi and Yaya & Yayo

Abstract

In this work we demonstrate the first realization of a comagnetormeter in the ultracold regime. In comparison to regular magnetometers, which are designed to maximize their magnetic field sensitivity, a comagnetometer uses paired magnetometers in a differential configuration to cancel the effects of the magnetic field and resolve weak dynamics that differently affect its constituents. Here, we implement a comagnetometer within the $f = 1$ and $f = 2$ ground state hyperfine manifolds of a ^{87}Rb spinor Bose-Einstein condensate (SBEC). The hyperfine manifolds feature nearly opposite gyromagnetic ratios and thus the sum of their precession angles is only weakly coupled to external magnetic fields, while being highly sensitive to any effect that rotates both manifolds in the same way.

A fundamental limitation of the comagnetometer is $f = 2 \rightarrow f = 1$ hyperfine relaxing collisions, where the liberated kinetic energy expels colliding atoms from the optical trap. These collisions are state-dependent and can be avoided by preserving the $f = 2$ spin state in a stretched configuration. We show how this can be achieved at low magnetic fields, where the spin-dependent contact interaction is the dominant energy contribution and stabilizes the spin orientation of the SBEC. Under these conditions, the comagnetometer coherence time can be extended to $\sim 1\,\mathrm{s}$ and the observed common magnetic field suppression is $44.0(8)\,\mathrm{dB}$. The technique is applied to precision measurement of the interhyperfine interaction in ^{87}Rb. The uncertainty in the obtained interhyperfine scattering lengths is reduced by more than a factor three with respect to previously reported values. We also present preliminary studies on phase-resolved parametric amplification within a SBEC comagnetometer. In this case, the $f = 2$ manifold undergoes parametric amplification, while the $f = 1$ manifold keeps track of the rotating reference frame induced by the applied external magnetic field.

We describe technical improvements to the experimental system in two areas: magnetic control and manipulation, and optical trapping and probing. The first group of improvements includes the implementation of radiofrequency (rf) and microwave (mw) driving and the development of a real-time rf source. The second group of improvements includes a pulsed optical trapping technique, a digital implementation of the laser locking scheme, and a hyperfine-selective Faraday probing method.

Resum

Aquesta tesi demostra el primer comagnetòmetre implementat en un sistema d'àtoms ultrafreds. Els magnetòmetres són altament sensibles a canvis en el camp magnètic. Els comagnetòmetres, en canvi, utlitzen magnetòmetres aparellats diferencialment per a cancel·lar la dependència del camp magnètic extern i discernir camps o interaccions que afecten de forma diferent als seus constituents. En aquest treball, s'implementa un comagnetòmetre mitjançant una superposició coherent dels estats hiperfins $f = 1$ i $f = 2$ d'un condensat spinorial de Bose-Einstein de ^{87}Rb. Aquests estats tenen fraccions giromagnètiques gairebé oposades, de manera que la suma dels seus angles de precessió no depèn del camp magnètic però es veu doblement afectada per interaccions que roten els dos estats en la mateixa direcció.

Les col·lisions de relaxació hiperfina $f = 2 \rightarrow f = 1$ limiten el temps de coherència del comagnetòmetre. En concret, els àtoms que hi participen són expulsats de la trampa òptica degut a l'energia cinètica alliberada en la col·lisó. Aquest tipus de col·lisó depenen de l'estat de spin i es cancel·len per a estats que maximitzen el spin a $f = 2$. En aquesta tesis demostrem la cancel·lació de collisions de relaxació hiperfina a camps magenètics baixos, on la interacció de spin és la contribució energètica dominant i estabilitza l'estat a $f = 2$. Sota aquestes condicions, el temps de coherència del comagnetòmetre s'exten fins a $\sim 1\,\mathrm{s}$ i el soroll de camp magnètic es veu atenuat per $44.0(8)\,\mathrm{dB}$. El comagnetòmetre s'ha usat per caracteritzar la interacció hiperfina en àtoms de ^{87}Rb. En compracació a estudis experimentals anteriors, s'ha aconseguit reduir en un factor tres la incertesa en les longituds de dispersió entre estats hiperfins. També presentem experiments preliminars d'amplificació paramètrica amb resolució de phase, on l'amplificació paramètrica té lloc a $f = 2$ i les rotacions magnètiques del sistema de referència són mesurades de forma simultània a $f = 1$.

Els avenços tècnics es divideixen en millores del control i de la manipulació magnètica, així com en millores del confinament i de la detecció òptica. Els primers inclouen els sistemes de manipulació atòmica mitjançant radiofreqüència i microones, com també el desenvolupament d'una font de radiofreqüència amb control en temps real. Els segons inclouen una tècnica de confinament polsat, la digitalització del sistema d'estabilització làser i la detecció òptica d'ambdós estats hiperfins.

Contents

Abbreviations

API	Application Programming Interface
BEC	Bose-Einstein Condensate
CMOT	Compressed Magneto-Optical Trap
ECDL	External Cavity Diode Laser
EDFA	Erbium-Doped Fiber Amplifier
ODT	Optical Dipole Trap
GUI	Graphical User Interface
LZS	Linear Zeeman Splitting
MOT	Magneto-Optical Trap
MTS	Modulation Transfer Spectroscopy
mw	Microwave
NIR	Near Infrared
NMR	Nuclear Magnetic Resonance
ODE	Ordinary Differential Equation
PLL	Phase-Locked Loop
PWM	Pulse-Width Modulation
QND	Quantum Nondemolition
QZS	Quadratic Zeeman Splitting
rf	Radiofrequency
RWA	Rotating Wave Approximation
SBEC	Spinor Bose-Einstein Condensate
SMA	Single-Mode Approximation
SPI	Serial Peripheral Interface
TF	Thomas-Fermi
TTL	Transistor-Transistor Logic
VCO	Voltage-Controlled Oscillator

1 Introduction

The research on Bose-Einstein Condensation (BEC) in ultracold quantum gases has undergone an explosive evolution since its first realisations in 1995 [1, 2, 3]. While the early publications were centred around the *smoking-gun* signatures of BECs and distinct magnetic trapping techniques [1, 2, 3, 4, 5, 6], the experimental research rapidly moved to explore low-energy excitations [7, 8, 9], superfluidity and vortices [10, 11], interference between BECs [12, 13], non-linear interactions and soliton oscillations [14, 15]... In fact, reference text books and review articles that address the full research on BECs in ultracold atomic gases (e.g. [16, 17, 18, 19]) date back to the early 2000s, beyond which the explorations branched into different subfields. This work belongs to the subfield of Spinor Bose-Einstein Condensates (SBECs), i.e. BECs with multiple internal spin states. The experimental realisation of SBECs required the simultaneous trapping of multiple spin states, which was initially achieved by magnetically trapping spin states with similar gyromagnetic ratios [13, 20] and by the introduction of optical trapping techniques [21, 22]. The latter method became the workhorse for future SBEC studies in ultracold atoms, including all-optical formation of SBECs [23]. A thorough review on the theoretical and experimental advances in SBEC can be found in [24] and [25], respectively. Relevant to this thesis are SBEC magnetometry, studies on intra- and interhyperfine interaction parameters and parametric spin amplification. Advances in these fields are outlined in the following.

Magnetometry. Spinor Bose-Einstein Condensates feature $\gtrsim 1\,\mathrm{s}$ long coherence times and typical spin domains below $\lesssim 10\,\mu\mathrm{m}$, which result in spin dynamics that are highly sensitive to the magnitude and spatial distribution of the applied magnetic field. These unique properties are leveraged by SBEC magnetometers. Based on the underlying spin readout technique, we distinguish between SBEC magnetometers using absorption imaging and those using dispersive light-atom interaction. While absorption imaging is a destructive technique, dispersive imaging reveals the *in-situ* atomic spin dynamics without hindering the evolution of the SBEC. Magnetometers based on absorption imaging have been used to explore magnetic field structures in the vicinity of atomic chip traps [26, 27], to

investigate local magnetic fields induced by dipole-dipole interactions [28] and to characterize AC magnetic fields [29]. On the other hand, polarization-dependent phase-contrast imaging [30] has been used for high precision magnetometry [31] and for revealing helical spin structures in presence of external magnetic field gradients [32]. Another dispersive imaging technique is collective Faraday probing, which has been applied to magnetometers implemented on single-domain SBECs [33]. Magnetometers operating in this regime offer unprecedented volume-adjusted sensitivity [34].

Characterisation of intra- and interhyperfine interaction parameters. The spin dynamics and ground state properties of SBECs not only depend on the external magnetic field, they are also strongly influenced by the interactions among the different spin components [24]. These are typically parametrized through intra- and interhyperfine s-wave scattering lengths, which describe the two-body collisional interaction between spin states within the same and distinct hyperfine manifolds. The scattering lengths can be estimated by comparing the measured SBEC spin dynamics to their theoretical model. In the case of intrahypefine scattering lengths this has been done for spin changing collisions and collisionally induced Rabi oscillations between two-particle Zeeman states in an optical lattice [35], spin mixing dynamics [36, 37] and by studying spin domain boundaries [22]. Further examples are the work by Harber *et al.* [38], where the ^{87}Rb intrahyperfine scattering lengths were characterised by resolving meanfield shifts through spectroscopy, and the work by Knoop *et al.* [39], where ^{23}Na Feshbach resonances were experimentally determined, yielding a better estimation of the underlying collision potentials and the s-wave intrahyperfine scattering lengths. Intrahyperfine scattering lengths have gathered less attention. In the particular case of ^{87}Rb the immiscibility between states $|f = 1, m_f = -1\rangle$ and $|2, 1\rangle$ has been quantitatively studied via ring excitations [40] and collective trap oscillations [41]. These measurements reported a single scattering length to characterise the interaction between hyperfine manifolds. The full set of spin-dependent intrahyperfine scattering lengths and the corresponding ground state diagram were recently characterised by Eto *et al.* [42, 43].

Parametric amplification. One of the unique assets of SBECs is the non-linear interaction among spin components which, in analogy to an optical medium exhibiting a $\chi^{(2)}$ non-linearity, can lead to degenerate parametric amplification and sub-Poissonian statistics, a.k.a. squeezing [44]. The process is intuitively understood for a $f = 1$ SBEC initially prepared in $|f = 1, m_f = 0\rangle$. Spin mixing couples the spin pair configurations $|1, 0\rangle \otimes |1, 0\rangle$ and $|1, -1\rangle \otimes |1, +1\rangle$. When both configuration have similar energies, the coupling becomes resonant and results in a phase-sensitive amplification of the atomic populations in $|1, -1\rangle$ and $|1, +1\rangle$. At the same time, the pair-wise creation of atoms in $|1, -1\rangle$ and $|1, +1\rangle$ yields correlations and squeezing in their relative atom numbers. The first experimen-

tal realization of a SBEC parametric amplifier was reported by Leslie *et al.* [45], demonstrating up to 30 dB amplification in the initial spin fluctuations across the condensate. These initial spin fluctuations or *seeds* can be of classical or quantum nature. Classical seeds are typically originated by radio frequency noise and share the same spatial wavefunction as the original SBEC field. On the other hand, quantum seeds arise from vacuum fluctuations and contribute equally to all spatial modes. Klempt *et al.* [46] reported parametric amplification seeded by vacuum fluctuations and the attendant spontaneous breaking of spatial and spin symmetry [47]. Parametric amplification also finds application in precision metrology and quantum-enhanced SU(1,1) interferometers, which use *non-linear beam splitters* to reach sensitivities close to the Heisenberg limit [48]. This has been experimentally demonstrated for SBECs initially prepared in the unstable $|2,0\rangle$ state of ^{87}Rb [49, 50] and more recently for single mode BECs of ^{23}Na in the $|1,0\rangle$ state [51]. In these works, the dynamics were sensitive to seedings in the $|f,\pm1\rangle$ states with relative atom numbers as low as $0.6/400 \approx 0.15\%$ and $35/(3\times10^4) \approx 0.12\%$, respectively.

About this thesis

In this thesis we extend the single-mode SBEC magnetometer reported by Palacios *et al.* [33] to create a SBEC comagnetometer, i.e. a pair of co-placed magnetometers implemented within a single SBEC. While magnetometers feature high magnetic field sensitivities, in a comagnetometer the common magnetic field contributions are strongly suppressed through a differential measurement. A comagnetometer retains sensitivity to effects that couple to its internal constituents differently than does the magnetic field. These contributions are typically weak and *buried* under the magnetic field noise of regular magnetometers. Comagnetometers have been used since the late 1960s for searches of new type of physics including anomalous spin interactions, spin-gravity couplings, Lorentz invariance and CPT violation, as well as for gyroscopy (see Chapter 6 for relevant references). Our SBEC comagnetometer is implemented on a coherent superposition of the $f = 1$ and $f = 2$ hyperfine manifolds, which operate as independent magnetic sensors but share the same spatial wavefunction. The development of the SBEC comagnetometer was reported in [52] and yielded a magnetic field suppression of 44.0(8) dB and coherence times of ~ 1 s.

Motivated by the the work of Eto *et al.* [42], we have applied the SBEC comagnetometer strategy for precision measurements of the interhyperfine scattering lengths of ^{87}Rb. The work was reported in [53] and additionally tackles a recurrent systematic uncertainty in cold atom experiments: the uncertainty in the trap conditions and mean density. The interhyperfine interaction parameters as well as for the calibration of the trap conditions are obtained as best estimates

from single-mode meanfield simulations fitted to the observed SBEC dynamics.

One of the original goals of this work was the development of a phase-resolving parametric spin amplifier. In fact, although we only present preliminary results on this topic, it was the driving force for developing our SBEC comagnetometer. The here presented spin amplifier uses a coherent superposition of the ^{87}Rb groundstate hyperfine manifolds, where $f = 2$ undergoes parametric amplification of the modes in $|2, \pm 1\rangle$, while $f = 1$ keeps track of the rotating reference frame and allows to retrieve the phase of the original seeds. We observe deterministic amplification of the $|2, \pm 1\rangle$ populations with relative seeds as low as $\sim 5/10^5 = 0.005\%$, close to an order of magnitude smaller than the values reported in [49, 50, 51].

The thesis is organized as follows. Chapter 2 provides the theoretical background for a SBEC that spans the $f = 1$ and $f = 2$ manifolds of ^{87}Rb. Chapter 3 describes the dispersive light-atom interaction and provides the theoretical background for Faraday rotation probing. Chapter 4 introduces coherent spin manipulations, applicable to radiofrequency drivings of Zeeman substates within $f = 1$ and $f = 2$ as well as to microwave drivings between manifolds. Chapter 5 presents the technical developments of this thesis. The key contributions are the development of a real-time radiofrequency source, the digitization of the laser locking scheme and the implementation of hyperfine-selective Faraday probing. Chapter 6 and Chapter 7 cover the SBEC comagnetometer and its application to the estimation of the interhyperfine scattering lengths in ^{87}Rb, closely following the discussions in [52, 53]. Chapter 8 is devoted to the conclusions and outlook.

The discussion is complemented with details on the calculations for the effective volume (Appendix A), code examples for the real-time rf source and digital PLL laser locks (Appendices B and C), preliminary results on phase-resolving parametric amplification (Appendix D) and supplementary information on the experimental sequences (Appendix E).

2

Description of a Spinor Bose-Einstein condensate

Although the pioneering Bose-Einstein experiments [1, 2, 3] were realized in spin-1 and spin-2 systems, with 3 and 5 respective Zeeman substates, the magnetic trapping limited the dynamics to the most *low-field seeking* Zeeman substate. These realizations fall into the category of scalar Bose-Einstein condensates and are described by a scalar order parameter. A spinor Bose Einstein (SBEC) extends the concept of macroscopic matterwaves to systems that are allowed to explore their spin degree of freedom, which became accessible through the development of spin-insensitive optical trapping techniques [22, 54].

In this section we revisit the frameworks for describing a spinor Bose-Einstein condensate in mean-field theory and under the single-mode approximation. Under these simplifications the state of the system is given by a complex ($\mathbb{C}^N$) vector and many spin dynamics are intuitively mapped to a Bloch sphere. We will define the single-particle, intrahyperfine and interhyperfine contributions to the mean-field energy and how to compute from them the dynamics of the system.

2.1. Mean-field formalism

A SBEC is generaly described by a vectorial field operator $\hat{\mathbf{\Psi}}(\mathbf{r})$ that fulfils the canonical commutation relation $[\hat{\Psi}_m^{(f)}(\mathbf{r}), \hat{\Psi}_{m'}^{(f')}(\mathbf{r}')^\dagger] = \delta_{m,m'}\delta_{f,f'}\delta(\mathbf{r}-\mathbf{r}')$, where $\delta_{i,j}$ and $\delta(\mathbf{r})$ are the Kronecker delta function and the Dirac delta distribution, respectively [17, 55, 56]. The components of the vector order parameter are labeled by superindex f and subindex $m = -f, ...f$, which represent the total spin and its projection along the $\mathbf{z}$ axis. The vectorial order parameter is suited to express the Hamiltonian of ultracold many-body system. Including one-body (non-

interacting) and two-body (interacting) contributions, the Hamiltonian reads

$$\begin{aligned}
\hat{H} &= \hat{H}_{\text{no-int}} + \hat{H}_{\text{int}} \,, \\
\hat{H}_{\text{no-int}} &= \int d\mathbf{r} \left[\sum_{f,m} \hat{\Psi}_m^{(f)}(\mathbf{r})^\dagger \left[-\frac{\hbar^2}{2M} \nabla^2 \right] \hat{\Psi}_m^{(f)}(\mathbf{r}) + \sum_{\mathbf{f},\mathbf{m}} V_{\mathbf{m}}^{(\mathbf{f})}(\mathbf{r})\; \hat{\Psi}_{m_1}^{(f_1)}(\mathbf{r})^\dagger\; \hat{\Psi}_{m_2}^{(f_2)}(\mathbf{r}) \right] , \\
\hat{H}_{\text{int}} &= \iint d\mathbf{r}\; d\mathbf{r}' \sum_{\mathbf{F},\mathbf{M}} U_{\mathbf{M}}^{(\mathbf{F})}(\mathbf{r},\mathbf{r}')\; \hat{\Psi}_{m_1}^{(f_1)}(\mathbf{r})^\dagger\; \hat{\Psi}_{m_2}^{(f_2)}(\mathbf{r}')^\dagger\; \hat{\Psi}_{m_3}^{(f_3)}(\mathbf{r})\; \hat{\Psi}_{m_4}^{(f_4)}(\mathbf{r}') \,,
\end{aligned} \tag{2.1}$$

where M is the atomic mass and $\hbar$ the reduced Planck constant. We write the one-body (non-interacting) potential as $V_{\mathbf{m}}^{(\mathbf{f})}(\mathbf{r})$, where $\mathbf{f} = (f_1, f_2)$ and $\mathbf{m} = (m_1, m_2)$. Similarly, we write the two-body interaction terms as $U_{\mathbf{M}}^{(\mathbf{F})}(\mathbf{r},\mathbf{r}')$ and their indices as $\mathbf{F} = (f_1, f_2, f_3, f_4)$ and $\mathbf{M} = (m_1, m_2, m_3, m_4)$.

We follow [16, 24, 25] and introduce the mean-field approximation where the operators $\hat{\Psi}_m^{(f)}(\mathbf{r})$ forming the vectorial order parameter are substituted by $\mathbb{C}$ functions representing their locally evaluated expectation (*mean*) values with respect to the many-body ground state. Under this simplification, the vectorial order parameter and Hamiltonian in Eq. (2.1) transform into

$$\hat{\Psi}_m^{(f)}(\mathbf{r}) \longrightarrow \Psi_m^{(f)}(\mathbf{r}) \equiv \langle \hat{\Psi}_m^{(f)}(\mathbf{r}) \rangle \,, \tag{2.2a}$$

$$\hat{H} \longrightarrow E \equiv \langle \hat{H} \rangle \,. \tag{2.2b}$$

We refer to $\Psi_m^{(f)}$ and E as the mean-field order parameter and the mean-field energy, respectively. Under this simplification, the density of atoms $n(\mathbf{r})$ and the total number of atoms N_A become:

$$n(\mathbf{r}) = \sum_{f,m} |\Psi_m^{(f)}(\mathbf{r})|^2 \,, \tag{2.3a}$$

$$N_A = \int d\mathbf{r}\; n(\mathbf{r}) \,. \tag{2.3b}$$

Applying the prescriptions in Eqs. (2.2) to the Hamiltonian in Eqs. (2.1) yields:

$$\begin{aligned}
E &= E_{\text{no-int}} + E_{\text{int}} \,, \\
E_{\text{no-int}} &= \int d\mathbf{r} \left[\sum_{f,m} \Psi_m^{(f)}(\mathbf{r})^* \left[-\frac{\hbar^2}{2M} \nabla^2 \right] \Psi_m^{(f)}(\mathbf{r}) + \sum_{\mathbf{f},\mathbf{m}} V_{\mathbf{m}}^{(\mathbf{f})}(\mathbf{r})\; \Psi_m^{(f)}(\mathbf{r})^*\; \Psi_{m'}^{(f)}(\mathbf{r}) \right] , \\
E_{\text{int}} &= \iint d\mathbf{r}\; d\mathbf{r}' \sum_{\mathbf{F},\mathbf{M}} U_{\mathbf{M}}^{(\mathbf{F})}(\mathbf{r},\mathbf{r}')\; \Psi_{m_1}^{(f_1)}(\mathbf{r})^*\; \Psi_{m_2}^{(f_2)}(\mathbf{r}')^*\; \Psi_{m_3}^{(f_3)}(\mathbf{r})\; \Psi_{m_4}^{(f_4)}(\mathbf{r}') \,.
\end{aligned} \tag{2.4}$$

Note that the terms $E_{\text{no-int}}$ and E_{int}, which are the one-body (non-interacting) and two-body (interacting) mean-field energies, scale differently with respect the atom number N_A. In fact, their energy contributions are of order $\mathcal{O}(N_A)^1$ and $\mathcal{O}(N_A)^2$, respectively.

While the above Eqs. (2.4) are written in a very general form, we use them to illustrate the effect of a further simplification of the mean-field treatment in case the spatial and spin part of the order parameter factorize. This simplification is known as the single mode approximation (SMA) and applies to systems in which the spin-dependent interaction energy is much weaker than the kinetic energy contribution such that it is energetically costly to develop spin textures [24]. Under the SMA, the mean-field order parameter becomes

$$\Psi_m^{(f)}(\mathbf{r},t) = \Psi_{\text{SMA}}(\mathbf{r})\,\xi_m^{(f)}(t)\;, \tag{2.5}$$

where $\Psi_{\text{SMA}}(\mathbf{r})$ describes the spatial distribution of the condensate and $\xi_m^{(f)}(t)$ the time-dependent spin amplitudes. They are normalized as follows:

$$\int d\mathbf{r}|\Psi_{\text{SMA}}(\mathbf{r})|^2 = 1\;, \tag{2.6a}$$

$$\sum_m |\xi_m^{(f)}|^2 = N_A^{(f)}\;, \tag{2.6b}$$

$$\sum_f N_A^{(f)} = N_A\;. \tag{2.6c}$$

Within the SMA and for a conserved atom number N_A, the kinetic energy becomes a constant energy contribution. Similarly, when the partial populations $N_A^{(f)}$ are independently conserved, there is a particular subset of potentials and two-body interactions terms that reduce to either a global or a f-dependent (but m-independent) constant energy contribution. We list them in Table 2.1.

These contributions result in a global or f-dependent (but m-independent) phase evolution, which are not resolved in the experiments of this work. We henceforth neglect them by explicitly removing the kinetic energy term from the mean-field energy and implicitly excluding contributions arising from terms listed in Table 2.1. This yields:

$$E = E_{\text{no-int}} + E_{\text{int}} = \sum_{\mathbf{f},\mathbf{m}} \mathcal{V}_{\mathbf{m}}^{(\mathbf{f})}\,{\xi_{m_1}^{(f_1)}}^*\xi_{m_2}^{(f_2)} + \sum_{\mathbf{F},\mathbf{M}} \frac{\mathcal{U}_{\mathbf{M}}^{(\mathbf{F})}}{V_{\text{eff}}}\,{\xi_{m_1}^{(f_1)}}^*{\xi_{m_2}^{(f_2)}}^*\xi_{m_3}^{(f_3)}\xi_{m_4}^{(f_4)}\;. \tag{2.7}$$

In Eq. (2.7), the spatial dependence has been *integrated out* and the external potential and two-body interaction are now captured by the terms $\mathcal{V}_{\mathbf{m}}^{(\mathbf{f})} \equiv \int d\mathbf{r}|\Psi_{\text{SMA}}(\mathbf{r})|^2 V_{\mathbf{m}}^{(\mathbf{f})}(\mathbf{r})$ and $\mathcal{U}_{\mathbf{M}}^{(\mathbf{F})} \equiv \iint d\mathbf{r}\,d\mathbf{r}'|\Psi_{\text{SMA}}(\mathbf{r})|^2|\Psi_{\text{SMA}}(\mathbf{r}')|^2 U_{\mathbf{M}}^{(\mathbf{F})}(\mathbf{r},\mathbf{r}')$. In

Form	Description
$V^{\mathbf{f}}_{\mathbf{m}}(\mathbf{r}) \propto \delta_{\mathbf{f}}\delta_{\mathbf{m}}$	Spin-independent potential.
$V^{\mathbf{f}}_{\mathbf{m}}(\mathbf{r}) \propto \delta_{\mathbf{f},f}\delta_{\mathbf{m}}$	Spin-f potential, m-independent.
$U^{(\mathbf{F})}_{\mathbf{M}}(\mathbf{r},\mathbf{r}') \propto \delta_{\mathbf{F}}\delta_{\mathbf{M}}$	Spin-independent interaction.
$U^{(\mathbf{F})}_{\mathbf{M}}(\mathbf{r},\mathbf{r}') \propto \delta_{\mathbf{F},f}\delta_{m_1,m_3}\delta_{m_2,m_4}$	Spin-f interaction, m-independent.
$U^{(\mathbf{F})}_{\mathbf{M}}(\mathbf{r},\mathbf{r}') \propto \delta_{f_1,f_3,f}\delta_{f_2,f_4,f'}\delta_{m_1,m_3}\delta_{m_2,m_4}$	Spin-f,f' interaction, m-independent.

Table 2.1.: Constant energy contributions to manifold f (within SMA and assuming independently conserved $N_A^{(f)}$). Concatenated Kronecker deltas are written as $\delta_{i,j,k,l,\ldots} \equiv \delta_{i,j}\delta_{i,k}\delta_{i,l}\ldots$, which yields 1 when $i = j = k = l = \ldots$ and 0 otherwise. The vectors indices are defined as $\mathbf{f} = (f_1, f_2)$, $\mathbf{m} = (m_1, m_2)$, $\mathbf{F} = (f_1, f_2, f_3, f_4)$ and $\mathbf{M} = (m_1, m_2, m_3, m_4)$.

the case of a two-body interaction described by a pseudopotential $U^{(\mathbf{F})}_{\mathbf{M}}(\mathbf{r},\mathbf{r}') = U^{(\mathbf{F})}_{\mathbf{M}}\delta(\mathbf{r}-\mathbf{r}')$, the latter integral becomes $\mathcal{U}^{(\mathbf{F})}_{\mathbf{M}} = U^{(\mathbf{F})}_{\mathbf{M}}/V_{\text{eff}}$, where the effective volume is $V_{\text{eff}} \equiv (\int dr^3 |\Psi_{\text{SMA}}(\mathbf{r})|^4)^{-1}$. The calculation of V_{eff} under the Thomas-Fermi approximation is described in Appendix A.

Eq. (2.7) also demonstrates that, within the SMA, the spin state of a SBEC as well as its energy are fully described by a complex vector, whose entries are the spin amplitudes $\xi^{(f)}_m$. Here and throughout this thesis we will restrict the description to a spinor BEC in the $5^2S_{1/2}$ ground state of ^{87}Rb, which features a hyperfine levels doublet: $f = 1$ and $f = 2$. The corresponding Zeeman sublevels span an 8-dimensional basis set in terms of which the spin order parameter is written:

$$\xi = \xi^{(1)} \oplus \xi^{(2)} = \begin{pmatrix} \xi^{(1)}_{+1} \\ \xi^{(1)}_{0} \\ \xi^{(1)}_{-1} \end{pmatrix} \oplus \begin{pmatrix} \xi^{(2)}_{+2} \\ \xi^{(2)}_{+1} \\ \xi^{(2)}_{0} \\ \xi^{(2)}_{-1} \\ \xi^{(2)}_{-2} \end{pmatrix} \tag{2.8}$$

In the following, the main contributions to $E_{\text{no-int}}$ and E_{int} (i.e. energy terms of the form $\mathcal{V}^{(\mathbf{f})}_{\mathbf{m}}$ and $\mathcal{U}^{(\mathbf{F})}_{\mathbf{M}}$) are discussed. These are the quadratic and linear Zeeman shifts and the intra- and interhyperfine interaction, respectively.

2.2. Linear and quadratic Zeeman shifts

The one-body Hamiltonian describing the hyperfine structure and the coupling to the an external magnetic field in the $5^2S_{1/2}$ groundstate of ^{87}Rb is [57]:

$$\hat{H}_{\rm hfs} + \hat{H}_B = A_{\rm hfs}\hat{\mathbf{i}}\cdot\hat{\mathbf{j}} + \mu_B\left(g_s\hat{\mathbf{s}} + g_l\hat{\mathbf{l}} + g_i\hat{\mathbf{i}}\right)\cdot\mathbf{B}\,, \tag{2.9}$$

where μ_B is the Bohr magneton and $\mathbf{B}$ the external applied magnetic field. The operators $\hat{\mathbf{l}}$,$\hat{\mathbf{i}}$,$\hat{\mathbf{s}}$ denote the orbital angular momentum, the nuclear spin and the electronic spin, respectively. The magnetic dipole constant $A_{\rm hfs}$, the Landé factors g_s, g_l, g_i and the corresponding quantum numbers for the operators above are given in Table 2.2. The total electron angular momentum is written as $\hat{\mathbf{j}} = \hat{\mathbf{l}} + \hat{\mathbf{s}}$, while for the ground state $l = 0$, so that $j = 1/2$.

Parameter	Symbol	Value	Ref.
Magnetic dipole constant	$A_{\rm hfs}$	$h \times 3.417\,341\,305\,452\,15(5)$ GHz	[58]
Spin Landé factor	g_s	2.00231930436256(35)	[59]
Orbital Landé factor	g_l	0.9999936(9)	[57]
Nuclear Landé factor	g_i	0.0009951414(10)	[60]
Electron spin	s	1/2	
Orbital ang. moment	l	0	
Nuclear spin	i	3/2	

Table 2.2.: Constants and quantum numbers describing the hyperfine structure and coupling to external magnetic fields in the $5^2S_{1/2}$ groundstate of ^{87}Rb. We denote by h the Planck constant.

We write the hyperfine angular momentum operator as $\hat{\mathbf{f}} = \hat{\mathbf{j}} + \hat{\mathbf{i}}$, where $i = 3/2$ and $f \in \{1, 2\}$. The hyperfine basis elements $\{|f, m\rangle\}$ are the eigenstates of $\hat{\mathbf{f}}^2$ and $\hat{f}_z$ (quantization axis along $\mathbf{z}$). In this basis set, the Hamiltonian becomes:

$$\begin{aligned}\langle f', m'|\,\hat{H}_{\rm hfs} + \hat{H}_B\,|f, m\rangle =& \frac{A_{\rm hfs}}{2}\left[f(f+1) - s(s+1) - i(i+1)\right]\delta_{f',f}\delta_{m',m} \\ &+\mu_B B_z \sum_{m_s,m_i}\left(g_s m_s + g_i m_i\right)\mathcal{C}^{f',m'}_{s,m_s,i,m_i}\mathcal{C}^{f,m}_{s,m_s,i,m_i}\,,\end{aligned} \tag{2.10}$$

where $\mathcal{C}^{f,m}_{s,m_s,i,m_i}$ are the Clebsch-Gordan coefficients, which under the Condon-Shortley phase convention are real valued, i.e. $\mathcal{C}^{f,m}_{s,m_s,i,m_i} = \langle s, m_s, i, m_i|f, m\rangle =$

$\langle f, m|s, m_s, i, m_i\rangle$. The running indices m_s and m_i, are the eigenvalues of $\hat{s}_z$ and $\hat{s}_i$, respectively and are constrained to $m_s \in [-s, s]$ and $m_i \in [-i, i]$.

The A_{hfs} term is the strongest energy contribution of Eq. (2.10), yielding a $h \times 6.8\,\text{GHz}$ energy splitting between $f = 1$ and $f = 2$ states. For the magnetic fields of this work ($B_z \approx 120\,\text{mG}$), the $\mu_B B_z$ term can be treated as a week perturbation ($\mu_B B_z / A_{\text{hfs}} \approx 5 \times 10^{-5}$), which breaks the degeneracy between distinct Zeeman sublevels. The resulting energy splitting is approximated into a linear ($\propto B$) and a quadratic ($\propto B^2$) term[1], which are the main contributions to the non-interacting Hamiltonian:

$$\hat{H}_{\text{no-int}} = \hat{H}^{(1)}_{\text{no-int}} \oplus \hat{H}^{(2)}_{\text{no-int}} \,, \tag{2.11a}$$

$$\hat{H}^{(f)}_{\text{no-int}} = p^{(f)} \hat{f}^{(f)}_z + q^{(f)} \hat{f}^{2(f)}_z \,, \tag{2.11b}$$

where $p^{(f)}$ and $q^{(f)}$ are the coefficients defining the linear (LZS) and quadratic (QZS) Zeeman shifts. By numerically diagonalizing Eq. (2.10) we find that $p^{(1)}$ and $p^{(2)}$ differ slightly in magnitude but are reversed in sign, while, for the precision of this work, $q^{(1)}$ and $q^{(2)}$ are simply reversed. Hence, we write the LZS and QZS as:

$$p^{(1)} = \hbar B \gamma^{(1)} \longrightarrow \gamma^{(1)} = -\gamma_0 - \gamma_s \,, \tag{2.12a}$$

$$p^{(2)} = \hbar B \gamma^{(2)} \longrightarrow \gamma^{(2)} = +\gamma_0 - \gamma_s \,, \tag{2.12b}$$

$$q^{(1)} = \hbar B^2 \beta^{(1)} \longrightarrow \beta^{(1)} = +\beta_0 \,, \tag{2.12c}$$

$$q^{(2)} = \hbar B^2 \beta^{(2)} \longrightarrow \beta^{(2)} = -\beta_0 \,. \tag{2.12d}$$

The LZS is expressed in terms of the gyromagnetic ratios $\gamma^{(1)}$ and $\gamma^{(2)}$ and the linear coupling constants $\gamma_0 \approx 2\pi \times 700.27\,\text{kHz/G}$ and $\gamma_s \approx 2\pi \times 1.39\,\text{kHz/G}$. For the QZS we have introduced the quadratic coupling constant $\beta_0 \approx 2\pi \times 71.74\,\text{Hz/G}^2$.

The single particle Hamiltonian in Eqs. 2.11 is explicitly written in a hyperfine-dependent notation, where $\hat{f}^{(f)}_i$ are the spin operators along direction $i \in \{x, y, z\}$ for $f = 1$ and $f = 2$. Of particular convenience are their matrix representation $[\hat{f}^{(f)}_i]_{mn} = \langle f, m|\hat{f}^{(f)}_i|f, n\rangle$, through which the evaluation of observables and energy contributions reduce to linear operations involving spin-f matrices and the vectorial order parameter $\xi = \xi^{(1)} \oplus \xi^{(2)}$. The corresponding spin-1 and

[1] We omit the $h \times 6.8\,\text{GHz}$ energy splitting between $f = 1$ and $f = 2$ since it is part of the constant energy contributions listed in Table 2.1.

spin-2 matrices are:

$$\hat{f}_x^{(1)} = \frac{1}{\sqrt{2}}\begin{pmatrix}0&1&0\\1&0&1\\0&1&0\end{pmatrix} \qquad \hat{f}_x^{(2)} = \frac{1}{2}\begin{pmatrix}0&2&0&0&0\\2&0&\sqrt{6}&0&0\\0&\sqrt{6}&0&\sqrt{6}&0\\0&0&\sqrt{6}&0&2\\0&0&0&2&0\end{pmatrix} \tag{2.13a}$$

$$\hat{f}_y^{(1)} = \frac{i}{\sqrt{2}}\begin{pmatrix}0&-1&0\\1&0&-1\\0&1&0\end{pmatrix} \quad \hat{f}_y^{(2)} = \frac{i}{2}\begin{pmatrix}0&-2&0&0&0\\2&0&-\sqrt{6}&0&0\\0&\sqrt{6}&0&-\sqrt{6}&0\\0&0&\sqrt{6}&0&-2\\0&0&0&2&0\end{pmatrix} \tag{2.13b}$$

$$\hat{f}_z^{(1)} = \begin{pmatrix}1&0&0\\0&0&0\\0&0&-1\end{pmatrix} \qquad \hat{f}_z^{(2)} = \begin{pmatrix}2&0&0&0&0\\0&1&0&0&0\\0&0&0&0&0\\0&0&0&-1&0\\0&0&0&0&-2\end{pmatrix} \tag{2.13c}$$

We use the spin matrices to compute the mean values of the spin operators $F_i^{(f)} \equiv \langle \hat{f}_i^{(f)} \rangle$ and $F_i^{2(f)} \equiv \langle \hat{f}_i^{2(f)} \rangle$:

$$F_i^{(f)} = \xi^{(f)^\dagger} \hat{f}_i^{(f)} \xi^{(f)} = \sum_{m,n} \xi_m^{(f)*} \xi_n^{(f)} [\hat{f}_i^{(f)}]_{mn} \ , \tag{2.14a}$$

$$F_i^{2(f)} = \xi^{(f)^\dagger} \hat{f}_i^{2(f)} \xi^{(f)} = \sum_{m,n,k} \xi_m^{(f)*} \xi_n^{(f)} [\hat{f}_i^{(f)}]_{mk} [\hat{f}_i^{(f)}]_{kn} \ . \tag{2.14b}$$

In terms of these we write the non-interacting energy resulting from Eqs. 2.11 as

$$E_{\text{no-int}}^{(f)} = p^{(f)} F_z^{(f)} + q^{(f)} F_z^{2(f)} \ . \tag{2.15}$$

Eq. (2.15) only depends on the mean spin projection along the magnetic field. The other spin projections are of importance for the spin interaction and the Faraday probing scheme, which make use of the total spin magnitude, the transverse spin magnitude and the azimuthal spin pointing angle. They are defined as

$$F^{(f)} \equiv \sqrt{F_x^{2(f)} + F_y^{2(f)} + F_z^{2(f)}} \ , \tag{2.16a}$$

$$F_\perp^{(f)} \equiv \sqrt{F_x^{2(f)} + F_y^{2(f)}} \ , \tag{2.16b}$$

$$\theta^{(f)} \equiv \arctan2\left(F_y^{(f)}, F_x^{(f)}\right) \ . \tag{2.16c}$$

The total mean spin magnitude $F^{(f)}$ should not be confused with fN_A, where f is the spin quantum number. They only coincide for $f = \frac{1}{2}$, when $\{\hat{\mathbb{1}}^{(f)}, \hat{f}_x^{(f)}, \hat{f}_y^{(f)}, \hat{f}_z^{(f)}\}$

is a complete generator set of the underlying SU$(2f+1)$ space. For larger spins $f > \frac{1}{2}$, the total spin magnitude is within the range $0 \leqslant F^{(f)} \leqslant f N_A^{(f)}$.

In the latter case, the upper and lower bounds of $F^{(f)}$ define two subsets of spin states. These are **oriented states**, describing ensembles where the total spin magnitude is maximal $F^{(f)} = f N_A^{(f)}$, and **aligned states**, describing ensembles where the total spin magnitude vanishes $F^{(f)} = 0$. While oriented stated can be visualized on a Bloch sphere, the representation of aligned states is more involved [25, 61]. Besides a distinct theoretical representation, aligned states also require one to use distinct observable for their experimental study. We generally denote these as alignment operators [62], where the relevant ones for this work are:

$$\hat{\jmath}_x^{(f)} = \hat{f}_x^{2(f)} - \hat{f}_y^{2(f)} \,, \tag{2.17a}$$

$$\hat{\jmath}_y^{(f)} = \hat{f}_x^{(f)}\,\hat{f}_y^{(f)} + \hat{f}_y^{(f)}\,\hat{f}_x^{(f)} \,, \tag{2.17b}$$

$$\hat{\jmath}_k^{(f)} = \hat{f}_x^{(f)}\,\hat{f}_z^{(f)} + \hat{f}_z^{(f)}\,\hat{f}_x^{(f)} \,, \tag{2.17c}$$

$$\hat{\jmath}_l^{(f)} = \hat{f}_y^{(f)}\,\hat{f}_z^{(f)} + \hat{f}_z^{(f)}\,\hat{f}_y^{(f)} \,, \tag{2.17d}$$

$$\hat{\jmath}_m^{(f)} = \frac{1}{\sqrt{3}} \left(2\hat{f}_z^{2(f)} - \hat{f}_x^{2(f)} - \hat{f}_y^{2(f)} \right) \,. \tag{2.17e}$$

The corresponding matrix expressions can be obtained by combining Eqs. (2.13) and Eqs. (2.17). Similar to the mean-field expressions for the spin operators, we write the mean-field values of the alignment operators as $J_i^{(f)} \equiv \langle \hat{\jmath}_i^{(f)} \rangle = \xi^{(f)^\dagger} \hat{\jmath}_i^{(f)} \xi^{(f)}$, where $i \in \{x, y, k, l, m\}$.

The classification into oriented and aligned states is of interest for studying the dynamical effect of the QZS and LZS. For this purpose, we assume an initial state perpendicularly stretched $F^{(f)} = F_\perp^{(f)} = f N_A^{(f)}$ to the external magnetic field $\mathbf{B} = B_z \mathbf{z}$. The system is driven by the Hamiltonian described in Eq. (2.11), which results in the following evolution for the spin projections:

$$F_x^{(f)}[t] = f N_A^{(f)} \cos\left(q^{(f)} t/\hbar\right)^{2f-1} \cos\left(p^{(f)} t/\hbar + \theta_0^{(f)}\right) \,, \tag{2.18a}$$

$$F_y^{(f)}[t] = f N_A^{(f)} \cos\left(q^{(f)} t/\hbar\right)^{2f-1} \sin\left(p^{(f)} t/\hbar + \theta_0^{(f)}\right) \,, \tag{2.18b}$$

$$F_z^{(f)}[t] = 0 \,, \tag{2.18c}$$

$$F_\perp^{(f)}[t] = f N_A^{(f)} \left|\cos\left(q^{(f)} t/\hbar\right)\right|^{2f-1} \,, \tag{2.18d}$$

where the azimuthal angle $\theta_0^{(f)}$ describes an arbitrary initial spin orientation. For typical magnetic field values of $B \approx 120\,\mathrm{mG}$, the LZS and QZS energy contributions differ by several orders of magnitude and have distinct effects on the

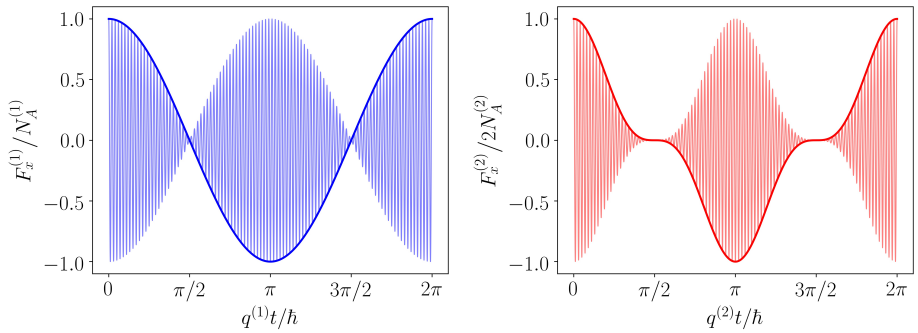

Figure 2.1.: Evolution of the spin components along x in $f = 1$ (left, blue) and $f = 2$ (right, red). The spin states are initially oriented along x ($\theta^{(f)} = 0$) and their evolution follows Eqs. 2.18. Thin lines show the spin evolution in the laboratory frame ($[F_x^{(1)}]_{\text{lab}}$ and $[F_x^{(2)}]_{\text{lab}}$) and thick lines are their equivalent in the rotating frame ($[F_x^{(1)}]_{\text{rot}}$ and $[F_x^{(2)}]_{\text{rot}}$). The carrier frequency is defined by the LZS ($p^{(f)}$) and its modulation by the QZS ($q^{(f)} \ll p^{(f)}$).

spin. The LZS introduces rapid Larmor precessions $|p^{(f)}/h| \approx 84\,\text{kHz}$ around the external magnetic field but leaves unchanged the transverse spin magnitude $F_\perp^{(f)}$. The QZS modulates of the transverse spin magnitude at a much slower frequency $|q^{(f)}/h| \approx 1\,\text{Hz}$ that drives the system from oriented to aligned states (and vice-versa). The above described dynamics are illustrated in Fig. 2.1.

It is convenient to define a rotating frame, which accounts for the rapid Larmor precessions introduced by the applied magnetic field. Since the $f = 1$ and $f = 2$ manifolds feature opposite LZS, it requires a dual rotating frame, under which the spin amplitudes transform:

$$\left[\xi_m^{(f)}(t)\right]_{\text{lab}} = e^{-ip^{(f)}t/\hbar}\left[\xi_m^{(f)}(t)\right]_{\text{rot}} . \tag{2.19}$$

While the spin state in the laboratory frame $[\xi_m^{(f)}(t)]_{\text{lab}}$ is governed by the Hamiltonian in Eq. (2.11) and has mean energy given in Eq. (2.15), the spin state in the rotating frame $[\xi_m^{(f)}(t)]_{\text{rot}}$ uses analogous expressions with $p^{(f)} = 0$. For observables which are invariant under $\mathbf{z}$ rotations, i.e. commute with $\hat{f}_z^{(f)}$, the reference frame is omitted in the notation. This applies to the mean values $F^{(f)}$, $F_\perp^{(f)}$, $F_z^{(f)}$ and $F_z^{2(f)}$. In Fig. 2.1 we can see the difference between spin observables represented in the laboratory and in the rotating frame.

We note, that although the above description of the LZS and QZS applies to

non-interacting spin-1 and spin-2 systems, they also provide an intuitive understanding of certain spin-dependent contact interactions. In fact, the following section demonstrates how the interhyperfine interaction between the $f = 1$ and $f = 2$ manifolds is equivalent to an effective LZS and QZS (see Eq. (2.28) and Eq. (2.29)).

2.3. Spin-dependent contact interaction

The contact interaction of a spin-f manifold is characterized by a set of $f + 1$ scattering lengths [24, 25]. We label these scattering lengths as $a_{\mathcal{C}}^{(\mathcal{F})}$, where $\mathcal{C}$ specifies scattering channel, i.e. the total spin quantum number of the colliding atoms, and $\mathcal{F} \in \{1, 2, 12\}$ indicates intrahyperfine ($1 \asymp 1$, $2 \asymp 2$) or interhyperfine ($1 \asymp 2$) scattering, respectively. In terms of these are defined the spin contact interaction coefficients [43]:

$$g_0^{(1)} = \frac{4\pi\hbar^2}{M} \frac{a_0^{(1)} + 2a_2^{(1)}}{3} , \tag{2.20a}$$

$$g_1^{(1)} = \frac{4\pi\hbar^2}{M} \frac{a_2^{(1)} - a_0^{(1)}}{3} , \tag{2.20b}$$

$$g_0^{(2)} = \frac{4\pi\hbar^2}{M} \frac{4a_2^{(2)} + 3a_4^{(2)}}{7} , \tag{2.20c}$$

$$g_1^{(2)} = \frac{4\pi\hbar^2}{M} \frac{a_4^{(2)} - a_2^{(2)}}{7} , \tag{2.20d}$$

$$g_2^{(2)} = \frac{4\pi\hbar^2}{M} \frac{7a_0^{(2)} - 10a_2^{(2)} + 3a_4^{(2)}}{7} , \tag{2.20e}$$

$$g_0^{(12)} = \frac{4\pi\hbar^2}{M} \frac{2a_2^{(12)} + a_3^{(12)}}{3}, \tag{2.20f}$$

$$g_1^{(12)} = \frac{4\pi\hbar^2}{M} \frac{a_3^{(12)} - a_2^{(12)}}{3} , \tag{2.20g}$$

$$g_2^{(12)} = \frac{4\pi\hbar^2}{M} \frac{3a_1^{(12)} - 5a_2^{(12)} + 2a_3^{(12)}}{3} . \tag{2.20h}$$

The values of the intra- and interhyperfine scattering lengths used for this work are given in Table 2.3.

The $f = 1$ spin contact interaction contributes an energy

$$E_{\text{int}}^{(1)} = \frac{1}{2V_{\text{eff}}} g_1^{(1)} \mathbf{F}^{(1)} \cdot \mathbf{F}^{(1)} . \tag{2.21}$$

Scattering parameter	Mean Value	Uncertainty	Ref
$a_0^{(1)}/a_0$	101.8	0.2	[63]
$(a_2^{(1)} - a_0^{(1)})/a_0$	-1.07	0.09	[35]
$a_0^{(2)}/a_0$	87.4	1	[64]
$(a_2^{(2)} - a_0^{(2)})/a_0$	3.51	0.54	[35]
$(a_4^{(2)} - a_2^{(2)})/a_0$	6.95	0.35	[35]
$(a_1^{(12)} - a_2^{(12)})/(a_2^{(1)} - a_0^{(1)})$	-1.31	0.13	[53]
$(a_3^{(12)} - a_2^{(12)})/(a_2^{(1)} - a_0^{(1)})$	-1.27	0.15	[53]

Table 2.3.: Mean values and associated uncertainties of the intrahyperfine scattering lengths ($a_{\mathcal{C}}^{(1)}$, $a_{\mathcal{C}}^{(2)}$) in terms of the Bohr radius a_0. The measurements for the interhyperfine scattering lengths ($a_{\mathcal{C}}^{(12)}$) are detailed in Chapter 7.

Similarly, the $f = 2$ manifold contributes an interaction energy energy

$$E_{\text{int}}^{(2)} = \frac{1}{2V_{\text{eff}}} \left(g_1^{(2)} \mathbf{F}^{(2)} \cdot \mathbf{F}^{(2)} + g_2^{(2)} \left| A_0^{(2)} \right|^2 \right) , \tag{2.22}$$

where $A_0^{(2)}$ is the spin-singlet scalar

$$A_0^{(2)} \equiv \frac{1}{\sqrt{5}} \left(2\xi_2^{(2)} \xi_{-2}^{(2)} - 2\xi_1^{(2)} \xi_{-1}^{(2)} + \xi_0^{(2)} \xi_0^{(2)} \right) . \tag{2.23}$$

Note that the interaction terms of the form $(g_1^{(f)}/V_{\text{eff}})\mathbf{F}^{(f)} \cdot \mathbf{F}^{(f)}$ introduce a energy splitting between aligned ($F^{(f)} = 0$) and oriented ($F^{(f)} = fN_A^{(f)}$) spin states. In Chapter 6 and Chapter 7 we will see how this energy opposes the QZS and can be used to characterize the interaction strength and infer the experimental trap conditions.

The inter-hyperfine scattering contribution has been recently described [43] and can be written as

$$E_{\text{int}}^{(12)} = \frac{1}{V_{\text{eff}}} \left(g_0^{(12)} N_A^{(1)} N_A^{(2)} + g_1^{(12)} [\mathbf{F}^{(1)}]_{\text{lab}} \cdot [\mathbf{F}^{(2)}]_{\text{lab}} + g_2^{(12)} [P_1^{(12)}]_{\text{lab}} \right) , \tag{2.24}$$

where $P_1^{(12)}$ results from interhyperfine scattering via the total-spin $\mathcal{C} = 1$:

$$\begin{aligned} P_1^{(12)} = &\left| \sqrt{\frac{1}{10}} \xi_1^{(1)} \xi_0^{(2)} - \sqrt{\frac{3}{10}} \xi_0^{(1)} \xi_1^{(2)} + \sqrt{\frac{3}{5}} \xi_{-1}^{(1)} \xi_2^{(2)} \right|^2 \\ &+ \left| \sqrt{\frac{3}{10}} \xi_1^{(1)} \xi_{-1}^{(2)} - \sqrt{\frac{2}{5}} \xi_0^{(1)} \xi_0^{(2)} + \sqrt{\frac{3}{10}} \xi_{-1}^{(1)} \xi_1^{(2)} \right|^2 \\ &+ \left| \sqrt{\frac{3}{5}} \xi_1^{(1)} \xi_{-2}^{(2)} - \sqrt{\frac{3}{10}} \xi_0^{(1)} \xi_{-1}^{(2)} + \sqrt{\frac{1}{10}} \xi_{-1}^{(1)} \xi_0^{(2)} \right|^2 \end{aligned} \tag{2.25}$$

While the intrahyperfine energy (Eq. (2.21) and Eq. (2.22)) is invariant under $\mathbf{z}$ rotations of the $f = 1$ and $f = 2$ manifolds, this is not the case of the interhyperfine interaction, which is the reason why the reference frame is specified in Eq. (2.24). The rapid relative Larmor precessions introduce oscillating energy contribution to the interhyperfine energy. These oscillating energy terms ($\sim p_0/h = 84\,\mathrm{kHz}$) are several orders of magnitudes faster than the typical timescales associated with spin dynamics driven by the two-body collisional interactions. This motivates the rotating wave approximation (RWA), i.e. dropping the rapidly oscillating terms.

The interaction $g_0^{(12)} N_A^{(1)} N_A^{(2)}$ is a constant contribution and can be excluded (see Table 2.1 and discussion around it). Under this simplification and applying the RWA, the mean interhyperfine energy becomes:

$$\overline{E_{\mathrm{int}}^{(12)}} = \frac{1}{V_{\mathrm{eff}}} \left(g_1^{(12)} F_z^{(1)} F_z^{(2)} + g_2^{(12)} \overline{P_1^{(12)}} \right) , \tag{2.26}$$

where

$$\begin{aligned} \overline{P_1^{(12)}} = &\frac{1}{10} \left| \xi_1^{(1)} \xi_0^{(2)} \right|^2 + \frac{3}{10} \left| \xi_0^{(1)} \xi_1^{(2)} \right|^2 + \frac{3}{5} \left| \xi_{-1}^{(1)} \xi_2^{(2)} \right|^2 \\ &+ \frac{3}{10} \left| \xi_1^{(1)} \xi_{-1}^{(2)} \right|^2 + \frac{2}{5} \left| \xi_0^{(1)} \xi_0^{(2)} \right|^2 + \frac{3}{10} \left| \xi_{-1}^{(1)} \xi_1^{(2)} \right|^2 \\ &+ \frac{3}{5} \left| \xi_1^{(1)} \xi_{-2}^{(2)} \right|^2 + \frac{3}{10} \left| \xi_0^{(1)} \xi_{-1}^{(2)} \right|^2 + \frac{1}{10} \left| \xi_{-1}^{(1)} \xi_0^{(2)} \right|^2 . \end{aligned} \tag{2.27}$$

Note that the RWA resolves the coexistence of distinct reference frames in Eq. (2.24). In fact, Eq. (2.26) is invariant under $\mathbf{z}$ rotations and is equally suited for describing the energy in the laboratory and in the rotating reference frame.

Intuition on the interhyperfine interaction

At first sight, the interhyperfine interaction results in a frightening combination of $f = 1$ and $f = 2$ spin amplitudes. However it can be often disentangled into an effective LZS and QZS. We write the effective changes in the LZS and QZS as $\Delta p_{\mathcal{X}}^{(f)}$ and $\Delta q_{\mathcal{X}}^{(f)}$, where f is the hyperfine manifold and $\mathcal{X} = 1$ or $\mathcal{X} = 2$ indicates the contribution arising from the $g_1^{(12)}$ or $g_2^{(12)}$ term, respectively.

The interaction due to $(g_1^{(12)}/V_{\text{eff}})F_z^{(1)}F_z^{(2)}$ describes an effective LZS of the $f = 1$ levels, with a strength proportional to $F_z^{(2)}$. The $f = 1$ magnetization similarly produces an effective LZS in the $f = 2$ manifold. This reads:

$$\begin{aligned}\Delta p_1^{(1)} &= \frac{g_1^{(12)}}{V_{\text{eff}}} F_z^{(2)} \ , \\ \Delta p_1^{(2)} &= \frac{g_1^{(12)}}{V_{\text{eff}}} F_z^{(1)} \ . \end{aligned} \tag{2.28}$$

The interaction term $(g_2^{(12)}/V_{\text{eff}})\overline{P_{12}}$ greatly simplifies when $f = 2$ is in a stretched state along or against the external magnetic field. This results in an effective LZS and QZS acting on the $f = 1$ manifold:

$$\begin{aligned}\Delta p_2^{(1)} &= \mp \frac{g_2^{(12)}}{V_{\text{eff}}} \frac{3}{10} N_A^{(2)} \ , \\ \Delta q_2^{(1)} &= \frac{g_2^{(12)}}{V_{\text{eff}}} \frac{3}{10} N_A^{(2)} \ , \end{aligned} \tag{2.29}$$

where $-$ and $+$ correspond to $f = 2$ states stretched along ($\xi_m^{(2)} = \sqrt{N_A^{(2)}}\delta_{m,2}$) and against ($\xi_m^{(2)} = \sqrt{N_A^{(2)}}\delta_{m,-2}$) the external magnetic field.

2.4. Spin dynamics

Once the intra- and interhyperfine contributions have been obtained, the dynamical evolution of the spin amplitudes $\xi_m^{(f)}$ are computed by differentiating the total energy:

$$i\hbar \frac{\partial \xi_m^{(f)}}{\partial t} = \frac{\partial E}{\partial \xi_m^{(f)*}} \ , \tag{2.30}$$

where $E = E_{\text{no-int}}^{(1)} + E_{\text{no-int}}^{(2)} + E_{\text{int}}^{(1)} + E_{\text{int}}^{(2)} + \overline{E_{\text{int}}^{(12)}}$. The right-hand side of Eq. (2.30) is computed analytically but the resulting set of eight non-linear ODEs is typically solved through numerical techniques. In this work we use numerical integration via the ODEPACK routine LSODA [65].

2.5. Inclusion of atom loss mechanisms

The lifetime of ultracold atomic ensembles is generally limited by collision processes that not only affect the internal spin state but couple to the kinetic energy of the cooled atoms. The liberated kinetic energy is typically several orders of magnitude greater that the trap depth, such that the colliding atoms are expelled from the confining potential. Depending on the number of trapped atoms involved in each type of collision, we distinguish between one-, two- and three-body losses. Examples are background gas collisions, hyperfine relaxing collisions and three-body recombination and molecule formation, respectively. In this section we will focus on one- and two-body losses which are captured by the inclusion of imaginary terms in the expression for the non-interaction energy, as well as in the expressions for the intra- and interhyperfine interaction energies.

One-body losses are primarily caused by collision with the background ^{87}Rb atoms of the vacuum chamber. While a higher background gas pressure favors the loading of the atomic ensemble and reduces the temporal overhead of state preparation, it also diminishes the lifetime of cooled atomic ensembles. For compact experiments operating in a single vacuum chamber, this results in a optimal background pressure which is a compromise between a short cycling time and a long lifetime time, both being of metrological relevance. On the other hand, experiments using separate *loading* and *science* vacuum chambers circumvent this issue by connecting them via a differential pumping section that decouples the pressures of the two regions.

We denote the typical one-body lifetime of the ensemble as τ, which is defined by $dN_A/dt = -\tau^{-1}N_A$. We can include one-body losses into Eq. (2.15) as

$$E^{(f)}_{\text{no-int}} = -\frac{i\hbar}{2\tau}N^{(f)}_A + p^{(f)}F^{(f)}_z + q^{(f)}\big[F^{(f)}_z\big]^2 \tag{2.31}$$

Two-body losses are primarily caused by hyperfine relaxing collisions, between $f = 2$ and $f = 2$ or $f = 1$ and $f = 2$ atoms. The rates of these collisions not only depend on the density of the atomic cloud but also on its spin state. We follow the formalism introduced in [66] and describe hyperfine relaxing collisions by including imaginary components in the scattering amplitudes. Under this prescription, the scattering amplitudes $a^{(\mathcal{F})}_{\mathcal{C}}$ and the interaction coefficients $g^{(\mathcal{F})}_{\mathcal{X}}$ defined in Eqs. (2.20) transform:

$$a^{(\mathcal{F})}_{\mathcal{C}} \to a^{(\mathcal{F})}_{\mathcal{C}} - i\tilde{a}^{(\mathcal{F})}_{\mathcal{C}} \,, \tag{2.32}$$

$$g^{(\mathcal{F})}_{\mathcal{X}} \to g^{(\mathcal{F})}_{\mathcal{X}} - i\tilde{g}^{(\mathcal{F})}_{\mathcal{X}} \,, \tag{2.33}$$

The imaginary components $\tilde{a}^{(\mathcal{F})}_{\mathcal{C}}$ and $\tilde{g}^{(\mathcal{F})}_{\mathcal{X}}$ are non-zero for $\mathcal{F} \in \{2, 12\}$ but vanish for the absolute hyperfine ground state, i.e. $\mathcal{F} = 1$. Hence, the inclusion

of hyperfine relaxation leaves the $f = 1$ interaction energy unchanged but for $f = 2$ we get

$$E_{\rm int}^{(2)} = \frac{1}{2V_{\rm eff}}\left(-i\tilde{g}_0^{(1)}N_A^{(1)}N_A^{(2)} + (g_1^{(2)} - i\tilde{g}_1^{(2)})\mathbf{F}^{(2)}\cdot\mathbf{F}^{(2)} + (g_2^{(2)} - i\tilde{g}_2^{(2)})\left|A_0^{(2)}\right|^2\right). \tag{2.34}$$

Similarly, the interhyperfine interaction energy becomes

$$\overline{E_{\rm int}^{(12)}} = \frac{1}{V_{\rm eff}}\left(-i\tilde{g}_0^{(12)}N_A^{(1)}N_A^{(2)} + (g_1^{(12)} - \tilde{g}_1^{(12)})F_z^{(1)}F_z^{(2)} + (g_2^{(12)} - \tilde{g}_2^{(12)})\overline{P_1^{(12)}}\right). \tag{2.35}$$

Note that the terms $N_A^{(2)}N_A^{(2)}$ and $N_A^{(1)}N_A^{(2)}$ in Eq. (2.34) and Eq. (2.35) only include imaginary scatting components. Their real counterparts are neglected since they belong to the energy contributions listed in Table 2.1

For **dynamical simulations** in the presence of incoherent (imaginary) energy contributions, the numerical integration introduced in Section 2.4 has to be performed under the following prescriptions:

(i) The atom numbers $N_A^{(1)}$, $N_A^{(2)}$, N_A as well as the effective volume $V_{\rm eff}$ (see Appendix A) are evolving quantities and have to be evaluated in each time step of the numerical integration.

(ii) The effective volume, which is a prefactor of the two-body interaction energy $E_{\rm int}\propto 1/V_{\rm eff}$, should be excluded from the differentiation in Eq. (2.30). That is, spin dynamics are evaluated through:

$$i\hbar\frac{\partial\xi_m^{(f)}}{\partial t} = \frac{\partial\left[E_{\text{no-int}}^{(1)} + E_{\text{no-int}}^{(2)}\right]}{\partial\xi_m^{(f)\,*}} + \frac{1}{V_{\rm eff}}\frac{\partial\left[V_{\rm eff}\left(E_{\rm int}^{(1)} + E_{\rm int}^{(2)} + E_{\rm int}^{(12)}\right)\right]}{\partial\xi_m^{(f)\,*}}. \tag{2.36}$$

3

Dispersive light-atom interaction

The off-resonant light-atom interaction is at the heart of any optical quantum nondemolition (QND) measurement. Prominent examples are found in cavity QED experiments [67] as well as in cold [68] and ultracold atomic ensembles [69]. In this chapter we will follow the latter examples, where the atomic magnetization is transferred to the probe polarization via the vector light-atom interaction.

We start by introducing the ground and excited spin states of the $\mathcal{D}_2$-line in ^{87}Rb. The light field and its polarization are expressed through the Stokes operators in second quantization. We describe the dispersive light-atom coupling via the scattering Hamiltonian, featuring a scalar, vectorial and tensorial contribution. We will comment on the absorptive counterpart, which sets an upper bound on the sensitivity of QND spin readouts.

3.1. Energy structure of the $\mathcal{D}_2$-line transition

While Chapter 2 is devoted to the $f = 1$ and $f = 2$ ground state manifolds, the light-atom interaction requires to introduce the optically accessible excited energy levels. For the purpose of this work, we will focus on the states belonging to the $\mathcal{D}_2$ line, which are the $5^2S_{1/2}$ (ground states) and $5^2P_{3/2}$ levels (optically excited states).

The $\mathcal{D}_2$ line is shown in Fig. 3.1, which highlights the very distinct transition energies (frequencies) between rotational states, hyperfine levels and Zeeman sublevels. The first are in the $\sim 10^{14}$ Hz range, located in the NIR part of the electromagnetic spectrum. The hyperfine interaction introduces energy splitting of $\sim 10^8 - 10^{10}$ Hz, and their manipulation require microwave (mw) driving techniques. For the magnetic fields of this work, the LZS introduces shifts of $\sim 10^5$ Hz, allowing to couple distinct Zeeman sublevels by means of radio frequency (rf) radiation. Besides separate driving techniques, these transitions also feature distinct decay rates (Γ). This is illustrated by Fermi's Golden Rule [44], showing a dependence of the form $\Gamma_{j\to i} \propto (\omega_0^{(ij)})^3$, where $\omega_0^{(ij)}$ is the resonant transition frequency between state i and a higher energy state j. As a result,

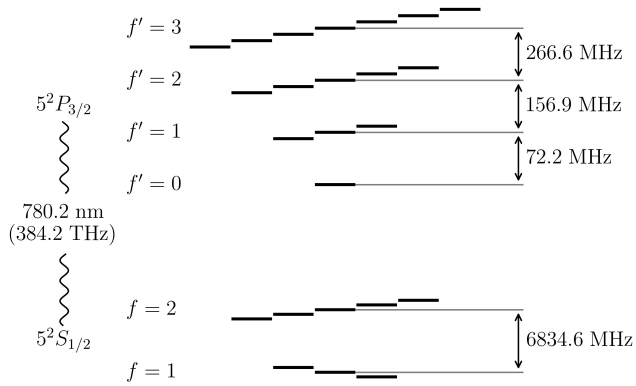

Figure 3.1.: Energy levels of the ^{87}Rb $\mathcal{D}_2$ line [57, 71, 58]. The strongest magnetic contribution is introduced by the LZS, represented by the *step-like* shifts among the different Zeeman sublevels within each hyperfine manifold. For the $5^2S_{1/2}$ levels, this has been calculated in Section 2.2 and neglecting the differential LZS results in $\pm 0.7\,\mathrm{MHz/G}$. For the $5^2S_{1/2}$ levels the LZS is $0.9\,\mathrm{MHz/G}$. Level spacings are not to scale.

rf and mw transitions have negligible spontaneous emission decay rates but the optical $\mathcal{D}_2$ line transitions exhibit a natural line width of $\Gamma = 2\pi \times 6.065(9)\,\mathrm{MHz}$ [70].

We will refer again to the level splitting of the $\mathcal{D}_2$ in the description of the apparatus and the laser systems (Chapter 5). In particular, we will label as *cooler*[1] the laser operating close to the $f = 2 \leftrightarrow f' = \{1, 2, 3\}$ transitions. Similarly, we denote as *repumper*[2] the laser operating close to the $f = 1 \leftrightarrow f' = \{0, 1, 2\}$ transitions.

[1] In reference to the cooling light field of the Magneto Optical Trap, which is red detuned to the $f = 2 \leftrightarrow f' = 3$ cycling transition.

[2] In reference to the repump light field of the Magneto Optical Trap, which is resonant to the $f = 1 \leftrightarrow f' = 2$ transition.

3.2. Quantum description of light

The quantization of the light field can be intuitively motivated by decomposing a classical field in terms of its frequency components, where the radiation field amplitudes are substituted with suitable creation and annihilation operators [72, 73]. For a monochromatic electric field at frequency ω, wavenumber k and propagation direction along $\mathbf{z}$ this reads:

$$\hat{\mathbf{E}}^{+}(\mathbf{r},\mathbf{t}) = \sqrt{\hbar Q}\sum_{\nu}\mathbf{u}_{\nu}\hat{a}_{\nu}e^{-i\omega t+ikz}\ , \tag{3.1a}$$

$$\hat{\mathbf{E}}^{-}(\mathbf{r},\mathbf{t}) = \sqrt{\hbar Q}\sum_{\nu}\mathbf{u}^{*}_{\nu}\hat{a}^{\dagger}_{\nu}e^{i\omega t-ikz}\ , \tag{3.1b}$$

with +(-) indexing the positive (negative) component of the electric field and $Q = \omega/2\epsilon_0 V$ being the form factor, expressed in terms of the vacuum permittivity ϵ_0 and the quantization volume V. The summation is taken over complementary polarization components ν. Depending on the chosen polarization basis we have $\nu \in \{H, V\}$ for horizontal and vertical linear polarizations, $\nu \in \{+45, -45\}$ for $+45°$ and $-45°$ linear polarizations, or $\nu \in \{+, -\}$ for σ^{+} and σ^{-} circular polarizations. More precisely, in terms of the $\mathbf{x}$ and $\mathbf{y}$ unitary vectors we have $\{\mathbf{u}_H, \mathbf{u}_V\} = \{\mathbf{x}, \mathbf{y}\}$, $\{\mathbf{u}_{+45}, \mathbf{u}_{-45}\} = \{(\mathbf{x}+\mathbf{y})/\sqrt{2}, (\mathbf{x}-\mathbf{y})/\sqrt{2}\}$ and $\{\mathbf{u}_{+}, \mathbf{u}_{-}\} = \{(\mathbf{x}+i\mathbf{y})/\sqrt{2}, (\mathbf{x}-i\mathbf{y})/\sqrt{2}\}$.

The annihilation $\hat{a}_{\nu}$ and creation $\hat{a}^{\dagger}_{\nu}$ operators, which *annihilate* or *create* a photon with polarization ν, obey the commutation relations:

$$[\hat{a}_{\nu}, \hat{a}^{\dagger}_{\nu'}] = \delta_{\nu,\nu'}\ . \tag{3.2}$$

In Chapter 2 we have discussed the representation of spin systems and we have highlighted that two level systems (spin $f = \frac{1}{2}$) can always be mapped on a Bloch sphere. This provides an intuitive representation of amplitudes and coherences of a quantum state. Similarly, polarizations can be mapped on the Poincaré sphere, showing the expectation values of the Stokes operators. They measure the photon imbalance between H/V, $+45°/-45°$, or $+/-$ polarization components and we write them as:

$$\hat{s}_x = \frac{1}{2}\left(\hat{a}^{\dagger}_{H}\hat{a}_{H} - \hat{a}^{\dagger}_{V}\hat{a}_{V}\right)\ , \tag{3.3a}$$

$$\hat{s}_y = \frac{1}{2}\left(\hat{a}^{\dagger}_{+45}\hat{a}_{+45} - \hat{a}^{\dagger}_{-45}\hat{a}_{-45}\right)\ , \tag{3.3b}$$

$$\hat{s}_z = \frac{1}{2}\left(\hat{a}^{\dagger}_{+}\hat{a}_{+} - \hat{a}^{\dagger}_{-}\hat{a}_{-}\right)\ . \tag{3.3c}$$

The Stokes operator associated to the total number of photons can be expressed independently of the chosen polarization basis as:

$$\hat{s}_0 = \frac{1}{2}\left(\hat{a}_\nu^\dagger \hat{a}_\nu + \hat{a}_{\nu'}^\dagger \hat{a}_{\nu'}\right) , \tag{3.4}$$

where ν and ν' are orthogonal basis elements. Here and throughout the rest of this manuscript, our preferred choice is the circular polarization basis $\nu \in \{+, -\}$. In this basis, the Stokes operators in Eq. (3.3) become

$$\hat{s}_i = \frac{1}{2}\hat{\mathbf{a}}^\dagger \sigma_i \hat{\mathbf{a}} , \tag{3.5a}$$

where $\hat{\mathbf{a}} = (\hat{a}_+, \hat{a}_-)^T$ and σ_i are the corresponding Pauli matrix for $i \in \{x, y, z\}$ and the 2×2 identity matrix for $i = 0$.

In analogy to the spin orientation and alignment operators, the Stokes operators have equivalent mean-field expressions which are well suited to describe coherent photon states [72] with mean photon numbers $N_L \gg 1$. We write the mean-field Stokes values as $S_i \equiv \langle \hat{s}_i \rangle$, where $i \in \{x, y, z, 0\}$ and the average is taken over the coherent photon state.

3.3. Off-resonant light-atom interaction

The rapidly oscillating electromagnetic field and the atomic spin degrees of freedom are coupled through the electric-dipole interaction. This section is devoted to the dispersive regime, where the light field is far detuned from the atomic transitions and their coupling can be approximated through first order time-dependent perturbation theory. As a result, the atomic populations are considered to remain in the ground state hyperfine manifolds and the light fields are only weakly perturbed. We follow the formalism introduced in [73] and provide the light-atom scattering Hamiltonians in second quantization. The corresponding mean-field dynamics are introduced in Section 3.5.

The energy shifts experienced by the atomic spins and the light field have spin-dependent as well as spin-independent contributions. Similarly, these shifts may depend only on the mean number of photons or on the particular polarization mode they are in. To disentangle the contributions, the light-atom interaction Hamiltonian is preferably represented in terms of its irreducible spherical tensor components, where each tensor components features a characteristic interaction strength and interaction dynamics. In this form, the off-resonant scattering Hamiltonian reads:

$$\hat{H}_s = \hat{H}_{s,0} + \hat{H}_{s,1} + \hat{H}_{s,2} . \tag{3.6}$$

The subscripts in Eq. (3.6) label the rank of the irreducible contributions. Hence, $\hat{H}_{s,0}$ is the scalar Hamiltonian, while $\hat{H}_{s,1}$ and $\hat{H}_{s,2}$ are the vector and tensor Hamiltonian, respectively. In a their most general form, we have [73]

$$\hat{H}_{s,j} = \sum_{f,f'} \hat{\mathbf{E}}^{-} \frac{\hat{\alpha}_j^{(ff')}}{\hbar \Delta^{(ff')}} \hat{\mathbf{E}}^{+} \ , \tag{3.7}$$

where $\hat{\alpha}_j^{(ff')}$ is the irreducible representation of the atomic polarizability tensor. The detuning between the light frequency ω and the transition frequency $\omega_0^{(ff')}$ is defined as $\Delta^{(ff')} = \omega - \omega_0^{(ff')}$. We follow the notation introduced in Fig. 3.1 and label the ground state hyperfine manifolds as $f \in \{1, 2\}$ and the excited ones as $f' \in \{0, 1, 2, 3\}$.

3.3.1. Cross-sectional interaction area

Eq. (3.7) inherits the form factor Q, which was introduced for the quantized electric operators and depends on the mode volume V (see below Eqs. 3.1). For the light-matter interaction, the mode volume relates to the spatial overlap between the light field and the atomic ensemble. We can define a characteristic cross-sectional area A, which yields the observed interaction when both the light intensity and the atomic column density are homogeneously distributed across A. As a result, for a light pulse of duration τ and wavelength λ the mode volume and form factor become $V = A \cdot c\tau$ and $Q = \pi/\epsilon_0 \lambda A \tau$.
We can more generally define the effective cross-sectional interaction area A as

$$A = \frac{\int dxdy\, \mathcal{I}(x,y) \int dxdy\, n_c(x,y)}{\int dxdy\, \mathcal{I}(x,y) n_c(x,y)} \ , \tag{3.8}$$

where the column density is obtained by integrating out the $\mathbf{z}$ direction, i.e. $n_c(x,y) = \int dz\, n(x,y,z)$. The transverse intensity distribution $\mathcal{I}(x,y)$ is explicitly independent of z as happens in the vicinity of the beam waist of a Gaussian laser beam propagating along that direction. We write a general Gaussian intensity profile as [74]:

$$\mathcal{I}(x,y,z) = \frac{2\mathcal{P}}{\pi w^2(z)} e^{-2(x^2+y^2)/w^2(z)} \ , \tag{3.9a}$$

$$w(z) = w_0 \sqrt{1 + (z/z_R)^2} \ , \tag{3.9b}$$

$$z_R = \frac{\pi w_0^2}{\lambda} \ , \tag{3.9c}$$

where $\mathcal{P}$ is total optical power, $w(z)$ the beam radius, w_0 the beam waist and z_R the Rayleigh range. In the vicinity of the beam waist $z \ll z_R$, the Gaussian

beam is collimated and the intensity profile is independent of z: $w(z) \to w_0$ and $\mathcal{I}(x,y,z) \to \mathcal{I}(x,y)$. Under this condition and a spherical atomic cloud with a Thomas Fermi radius r_{TF} (see Appendix A) we have:

$$\mathcal{I}(x,y) = \frac{2\mathcal{P}}{\pi w_0^2} e^{-2(x^2+y^2)/w_0^2} \,, \tag{3.10}$$

$$n(x,y) = N_A \frac{5(r_{\mathrm{TF}}^2 - x^2 - y^2)^{3/2}}{2\pi r_{\mathrm{TF}}^5} \,, \tag{3.11}$$

$$A = \pi r_{\mathrm{TF}}^2 \frac{16/5}{8 - 6\kappa^2 + 3\sqrt{2}\kappa^3 \mathcal{F}(\sqrt{2}\kappa^{-1})} \,, \tag{3.12}$$

where $\mathcal{F}$ is the Dawson integral and $\kappa \equiv w_0/r_{\mathrm{TF}}$.

In Fig. 3.2 we show the cross-sectional area for distinct ratios between the spatial extents of the Gaussian and the atomic cloud. When the beam waist is much smaller than the atomic ensemble ($\kappa \ll 1$), the photons only interact with the central column density such that $A \to 2/5 \times \pi r_{\mathrm{TF}}^2$. On the other hand, when $\kappa \gg 1$, the atoms only interact with central part of the Gaussian beam and $A \to \pi w_0^2/2 = \kappa^2/2 \times \pi r_{\mathrm{TF}}^2$.

3.3.2. Scalar scattering Hamiltonian

The scalar scattering Hamiltonian reads [73]

$$\hat{H}_{s,0}^{(f)} = \frac{\hbar}{\tau} G_0^{(f)} \hat{s}_0 \hat{\mathbb{1}}^{(f)} \,, \tag{3.13}$$

$$\tag{3.14}$$

where $\hat{\mathbb{1}}^{(f)}$ is the identity operator of hyperfine manifold f. We compute the scalar light-atom coupling $G_0^{(f)}$ factor for $f = 1$ and $f = 2$, yielding

$$G_0^{(1)} = \frac{\lambda_0^3}{\pi\lambda A} \times \frac{3\Gamma}{72} \left(\frac{2}{\Delta^{(10')}} + \frac{5}{\Delta^{(11')}} + \frac{5}{\Delta^{(12')}} \right) \,, \tag{3.15a}$$

$$G_0^{(2)} = \frac{\lambda_0^3}{\pi\lambda A} \times \frac{3\Gamma}{120} \left(\frac{1}{\Delta^{(21')}} + \frac{5}{\Delta^{(22')}} + \frac{14}{\Delta^{(23')}} \right) \,. \tag{3.15b}$$

where λ is the light wavelength and Γ and λ_0 are the resonant linewidth and wavelength given in Section 3.1. For detunings much larger than the excited state hyperfine splitting the scalar light-atom coupling factor converges to $G_0^{(f)} \to (\lambda_0^3/\pi\lambda A) \times (\Gamma/2\Delta^{(f)})$.

The scalar scattering interaction is independent of the atomic spin and light polarization. This results in a density dependent change in the refractive index,

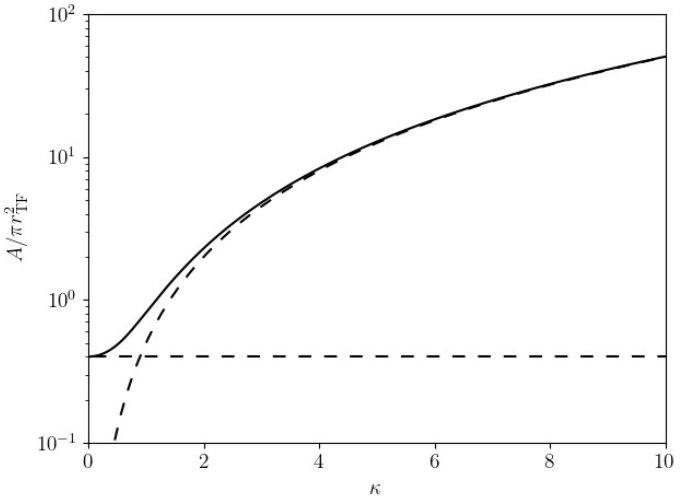

Figure 3.2.: Cross-sectional interaction area as a function of the ratio between beam waist and Thomas-Fermi radius $\kappa = w_0/r_{\mathrm{TF}}$. The area is expressed in terms of the SBEC cross section πr_{TF}^2. Dashed lines indicate the limits for $\kappa \ll 1$ and $\kappa \gg 1$ where $A \to 2/5 \times \pi r_{\mathrm{TF}}^2$ and $A \to \pi w_0^2/2 = \kappa^2/2 \times \pi r_{\mathrm{TF}}^2$, respectively.

which has been observed in cavity QED experiments with single atoms [67] as well as trapped BECs [75]. From the perspective of the atomic ensemble it is more convenient to express the Stokes parameter through its classical limit as $(2\hbar\omega/A\tau)\hat{s}_0 \to \mathcal{I}(x,y)$. Including this into Eq. (3.13) we obtain an energy shift depending on the local light intensity, which in the vicinity of the beam waist ($|z| \ll w_0 \ll z_r$) corresponds to a harmonic potential. In the limit of large detunigs and trapping beams that exceed the size of the SBEC, i.e. $G_0^{(f)} \to (\lambda_0^3/\pi\lambda A) \times (\Gamma/2\Delta^{(f)})$ and $A \to \pi w_0^2/2$, we have:

$$\hat{H}_{s,0}^{(f)} \approx -V_0^{(f)} + \frac{1}{2} m \sum_i [\omega_i^{(f)} i]^2 \,, \tag{3.16a}$$

$$V_0^{(f)} = -\frac{\Gamma\lambda_0^3}{8\pi^2 c} \frac{\mathcal{I}(x,y,z)}{\Delta^{(f)}}\bigg|_{(x,y,z)=\mathbf{0}} \,, \tag{3.16b}$$

$$\omega_i^{(f)} = \sqrt{\frac{1}{m}\frac{\partial^2}{\partial i^2}\left[\frac{\Gamma\lambda_0^3}{8\pi^2 c}\frac{\mathcal{I}(x,y,z)}{\Delta^{(f)}}\right]\bigg|_{(x,y,z)=\mathbf{0}}} \tag{3.16c}$$

where $V_0^{(f)}$ is the trap depth and the spatial coordinates are indexed as $i \in \{x, y, z\}$. For the particular case of a gaussian beam with an intensity profile as described in Eqs. (3.9) we get

$$V_0^{(f)} = -\frac{\Gamma\lambda_0^3}{4\pi^3 c w_0^2}\frac{\mathcal{P}}{\Delta^{(f)}} \,. \tag{3.17a}$$

$$\omega_{x,y}^{(f)} = \sqrt{-\frac{\Gamma\lambda_0^3}{mc\pi^3 w_0^4}\frac{\mathcal{P}}{\Delta^{(f)}}} \,, \tag{3.17b}$$

$$\omega_z^{(f)} = \sqrt{\frac{1}{2\pi^2}}\frac{\lambda}{w_0}\omega_{x,y}^{(f)} \,. \tag{3.17c}$$

For typical dipole traps $\lambda \sim 1\,\mu\text{m}$ and $w_0 \sim 10 - 100\mu\text{m}$, which results in 10 to 100 times weaker trapping frequencies along the propagation direction than along the tightly confined transverse directions.

3.3.3. Vector scattering Hamiltonian

The vector scattering Hamiltonian is of the form [73]

$$\hat{H}_{s,1}^{(f)} = \frac{\hbar}{\tau} G_1^{(f)} \hat{s}_z \hat{f}_z^{(f)} \tag{3.18}$$

where the vector light-atom coupling constants are

$$G_1^{(1)} = \frac{\lambda_0^3}{\pi\lambda A} \times \frac{\Gamma}{32}\left(-\frac{4}{\Delta^{(10')}} - \frac{5}{\Delta^{(11')}} + \frac{5}{\Delta^{(12')}}\right) \,, \tag{3.19a}$$

$$G_1^{(2)} = \frac{\lambda_0^3}{\pi\lambda A} \times \frac{\Gamma}{160}\left(-\frac{3}{\Delta^{(21')}} - \frac{5}{\Delta^{(22')}} + \frac{28}{\Delta^{(23')}}\right) \,. \tag{3.19b}$$

In the limit of large detunings we have $G_1^{(1)} \to -(\lambda_0^3/\pi\lambda A) \times (\Gamma/8\Delta^{(1)})$ and $G_1^{(2)} \to +(\lambda_0^3/\pi\lambda A) \times (\Gamma/8\Delta^{(2)})$.

The physical interpretation of the vector-light coupling is twofold. On the light polarization side, it induces circular birefringence proportional to the spin orientation along the light propagation axis. This effect has a strong analogy to magneticaly induced Faraday rotation [76], describing the difference in phase shifts for σ^+ and σ^- polarizations traveling through an atomic medium under an external magnetic field. In this case, the linear Zeeman splitting differently detunes the allowed σ^+ and σ^- optical transitions which results in a distinct phase shift for each polarization. For the interaction described in Eq. (3.18) the rotation depends on the atomic population of the distinct Zeeman sublevels and can be used for quantum nondemolition (QND) measurements. We refer

to this technique as **Faraday rotation probing** and it will be explained in detail in Section 5.3.4. As regards the atomic ensemble, the vector scattering Hamiltonian introduces an effective linear Zeeman splitting proportional to $\hat{S}_z$, which is proportional to the imbalance between the σ^+ and the σ^- components of the light field.

In Fig. 3.3 we show the vector coupling constants as a function of detuning. Outside the central region, the $f = 1$ vector light-atom coupling is strongest below the closed transition $f = 1 \leftrightarrow f' = 0$. Similarly, for $f = 2$ the interaction is significant above the closed transition $f = 2 \leftrightarrow f' = 3$. The operational detunings of the Faraday rotation probing were chosen within these ranges.

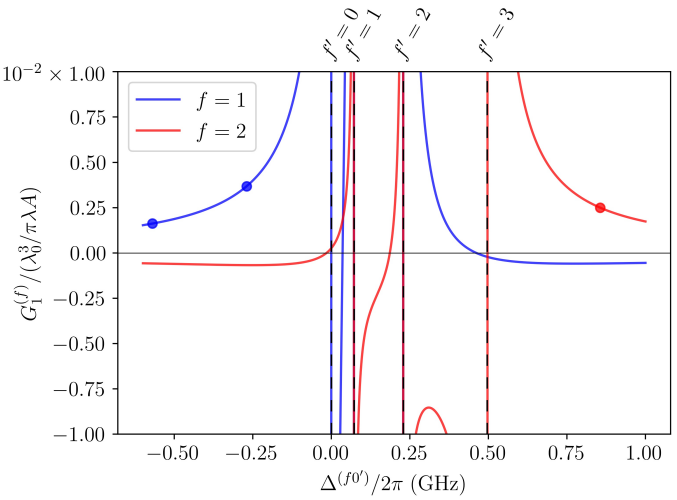

Figure 3.3.: Vector coupling constant $G_1^{(f)}$ for $f = 1(2)$ in blue (red) as a function of the detuning referenced to the $f = 1(2) \leftrightarrow f' = 0$ transition. Dashed lines indicate the position of the excited $f' = \{0, 1, 2, 3\}$ hyperfine levels. The full blue and red circles indicate the operational point for the Faraday rotation probing of $f = 1$ and $f = 2$: $\Delta^{(10')}/2\pi \in \{-570\,\text{MHz}, -270\,\text{MHz}\}$ and $\Delta^{(23')}/2\pi = 360\,\text{MHz}$.

3.3.4. Tensor scattering Hamiltonian

We write the tensor scattering Hamiltonian as [73]

$$\hat{H}_{s,2}^{(f)} = \frac{\hbar}{\tau} G_2^{(f)} \left(\hat{s}_x \hat{j}_x^{(f)} + \hat{s}_y \hat{j}_y^{(f)} + \frac{1}{\sqrt{3}} \hat{s}_0 \hat{j}_m^{(f)} \right) , \tag{3.20}$$

where the tensor coupling constants are

$$G_2^{(1)} = \frac{\lambda_0^3}{\pi\lambda A} \times \frac{\Gamma}{32}\left(\frac{4}{\Delta^{(10')}} - \frac{5}{\Delta^{(11')}} + \frac{1}{\Delta^{(12')}}\right) , \tag{3.21a}$$

$$G_2^{(2)} = \frac{\lambda_0^3}{\pi\lambda A} \times \frac{\Gamma}{160}\left(\frac{1}{\Delta^{(21')}} - \frac{5}{\Delta^{(22')}} + \frac{4}{\Delta^{(23')}}\right) . \tag{3.21b}$$

For large detunings, the tensor light shift scales as $G_2^{(1)} \to (\lambda_0^3/\pi\lambda A)\times\Gamma(-4\omega_0^{(0'1')} + \omega_0^{(1'2')})/32(\Delta^{(1)})^2$ and $G_2^{(2)} \to (\lambda_0^3/\pi\lambda A) \times \Gamma(-\omega_0^{(2'1')} + 4\omega_0^{(3'2')})/160(\Delta^{(2)})^2$.

The tensor scattering Hamiltonian couples the light polarization to the alignment spin components, introduced in Chapter 2. Similar to the QZS, the tensorial light shift introduces orientation to alignment conversion that hinders Faraday rotation measurements based on the vector light-atom interaction. This effect can be avoided in two ways. First, in the presence of an external magnetic field, the polarization can be adjusted such that the tensorial light shift averages out over one Larmor precession period. For a linearly polarized light field this is achieved at the *magic angle*, when the polarization is tilted by 54.7° with respect to the applied magnetic field [77]. Second, the use of alternating probe polarizations results in a dynamical decoupling that has shown to mitigate the contribution of the tensorial light-atom interaction [78].

In Fig. 3.4 we represent the ratio between the tensor and vector coupling constants for $f = 1$ and $f = 2$ as a function of detuning. We see that, for the detunings of this work, the tensorial coupling is at least one order of magnitude weaker than its vectorial counterpart.

3.4. Off-resonant photon absorption

Photon absorption and subsequent spontaneous emission events introduce loss of coherence and depolarization, which reduce the visibility of coherent light-atom interactions and ultimately limits the Faraday rotation readout. At the same time, the associated *recoil-kicks* introduce a significant footprint on the temperature of the atomic cloud, prepared at temperatures below the recoil temperature $k_B T_{\text{recoil}} = \hbar^2\omega^2/2mc^2$, where k_B is the Boltzmann constant.

In the limit of small absorptions, the number of decohered atoms δN_A is [79]

$$\delta N_A^{(f)} = \frac{\sigma N_L N_A^{(f)}}{A} , \tag{3.22}$$

where σ is the scattering cross section and A is the light-atom interaction area defined in Eq. (3.8). We note that $\delta N_A^{(f)}$ depends on the spatial overlap between the light field and the atomic ensemble (described by A), but also on the light

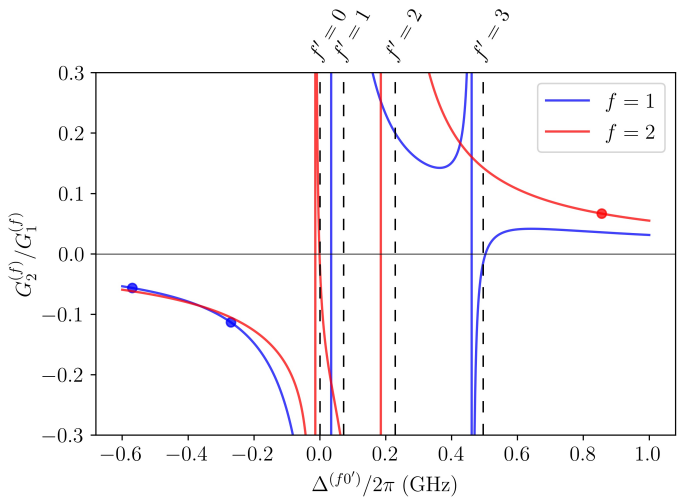

Figure 3.4.: Ratio between tensor and vector coupling constants $G_2^{(f)}/G_1^{(f)}$ for $f = 1(2)$ in blue (red) as a function of the detuning referenced to the $f = 1(2) \leftrightarrow f' = 0$ transition. Dashed lines indicate the position of the excited $f' = \{0, 1, 2, 3\}$ hyperfine levels. The full blue and red circles indicate the operational point for the Faraday rotation probing of $f = 1$ and $f = 2$: $\Delta^{(10')}/2\pi \in \{-570\,\text{MHz}, -270\,\text{MHz}\}$ and $\Delta^{(23')}/2\pi = 360\,\text{MHz}$.

polarization, detuning, atomic polarizability and atomic spin state, which are encoded in σ.

By decomposing the scattering cross section into its individual contributions, the loss of coherence in each individual Zeeman sublevel can be found, as well as the associated degradation of the macroscopic spin, *aka* depolarization. To this purpose, we will compute the scattering cross section σ for a simple two level atom and extend the formalism to capture the $f = 1$ and $f = 2$ hyperfine manifolds and their Zeeman sublevels.

For a two level atom, the scattering cross section between ground state f and excited state f' is equal to [57, 80]

$$\sigma = \frac{\sigma_0}{1 + 4(\Delta/\Gamma)^2 + (I/I_{sat})}\,, \tag{3.23}$$

where $\Delta = \omega - \omega_0$ is the detuning between the light frequency ω and the atomic resonance frequency ω_0. The resonant scattering cross section σ_0, the saturation

intensity I_{sat} and the natural linewidth Γ satisfy:

$$\sigma_0 = \frac{\hbar\omega_0\Gamma}{2I_{\mathrm{sat}}} , \tag{3.24}$$

$$I_{\mathrm{sat}} = \frac{c\epsilon_0\hbar^2\Gamma^2}{4|\langle f|\mathbf{u}\cdot\hat{\mathbf{d}}|f'\rangle|^2} , \tag{3.25}$$

$$\Gamma = \frac{\omega_0^3}{3\pi\epsilon_0\hbar c^3}\frac{2j+1}{2j'+1}|\langle j||\hat{\mathbf{d}}||j'\rangle|^2 . \tag{3.26}$$

The unit vector $\mathbf{u}$ points along the polarization axis and projects onto it the dipole operator $\hat{\mathbf{d}} = -e\hat{\mathbf{r}}$, where e is the electron charge. The quantum numbers for the total electron angular momentum of the ground and excited states are given by j and j', respectively. They are used to compute $\langle j||\hat{\mathbf{d}}||j'\rangle$, the reduced matrix element of the dipole operator. We note that in the limit of weak intensities, the power broadening introduced by the term $I/I_{\mathrm{sat}} \ll 1$ is negligible. Under this approximation and combining Eqs. 3.23-3.26 we get

$$\sigma = \frac{3\lambda^2}{2\pi}\frac{2j'+1}{2j+1}\frac{|\langle f|\mathbf{u}\cdot\hat{\mathbf{d}}|f'\rangle|^2}{|\langle j||\hat{\mathbf{d}}||j'\rangle|^2}\frac{1}{1+4(\Delta/\Gamma)^2} , \tag{3.27}$$

Eq. (3.27) can be extended to a multilevel atom by adding the contributions of each allowed ground to excited state transition:

$$\sigma = \sum_f \sigma^{(f)} , \tag{3.28a}$$

$$\sigma^{(f)} = \sum_m \rho_m^{(f)}\sigma_m^{(f)} , \tag{3.28b}$$

$$\sigma_m^{(f)} = \sum_{f'm'} \sigma_{mm'}^{(ff')} , \tag{3.28c}$$

$$\sigma_{mm'}^{(ff')} = \frac{3\lambda^2}{2\pi}\frac{2j'+1}{2j+1}\frac{|\langle f,m|\mathbf{u}\cdot\hat{\mathbf{d}}|f',m'\rangle|^2}{|\langle j||\hat{\mathbf{d}}||j'\rangle|^2}\frac{1}{1+4(\Delta^{(ff')}/\Gamma)^2} . \tag{3.28d}$$

Eqs. (3.28) have been constructed incrementally. The inner most terms is $\sigma_{mm'}^{(ff')}$, yielding the the scattering-cross section between the ground state $|f,m\rangle$ and the excited state $|f',m'\rangle$. By summing over all excited states, $\sigma_m^{(f)}$ is obtained, which represents the total cross-section for a givenground state $|f,m\rangle$. The hyperfine-dependent and overall cross-sections, $\sigma^{(f)}$ and σ, are obtained by a weighted summation over the different $\sigma_m^{(f)}$. The weighting coefficients are the relative spin populations $\rho_m^{(f)} = |\xi_m^{(f)}|^2/N_A$.

Photon absorption and spontaneous emission events shuffle the atomic populations (diagonal terms in the density matrix) and reduce the coherences of the

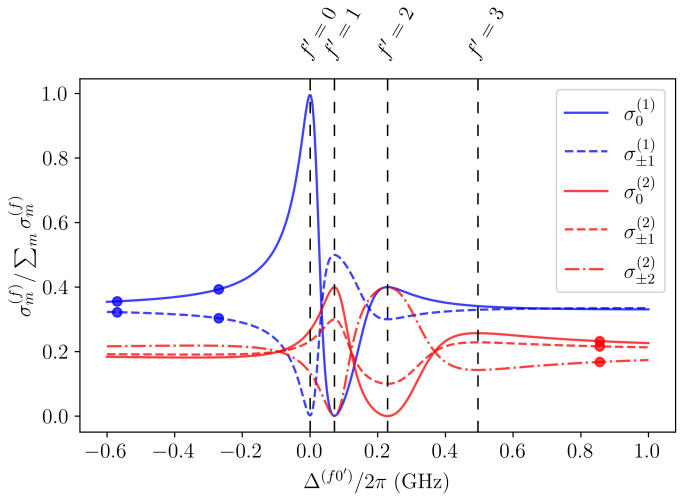

Figure 3.5.: Relative contribution of the scattering cross-section $\sigma_m^{(f)}$ for $f = 1(2)$ in blue (red). Dashed lines indicate the position of the excited $f' = \{0, 1, 2, 3\}$ hyperfine levels. The full blue and red circles indicate the operational point for the Faraday rotation probing of $f = 1$ and $f = 2$: $\Delta^{(10')}/2\pi \in \{-570\,\mathrm{MHz}, -270\,\mathrm{MHz}\}$ and $\Delta^{(23')}/2\pi = 360\,\mathrm{MHz}$.

ensemble (off-diagonal terms in the density matrix). Only the latter terms are relevant for the transverse magnetisation $F_\perp^{(f)}$ and the loss of coherence can be modelled by an effective attenuation of the spinor order parameter. This reads[3]

$$\xi_m^{(f)} = \xi_{m,0}^{(f)}\, e^{-N_L \sigma_m^{(f)}/2A}\,, \tag{3.29}$$

where $\xi_{m,0}^{(f)}$ are the initial spin amplitudes before the absorptive light-atom interaction.

The effective attenuation factor in Eq. (3.29) is proportional to $\sigma_m^{(f)}$, which generally depends on the particular ground state $|f, m\rangle$, the light polarization and its detuning. Fig. 3.5 shows the relative scattering cross-sections $\sigma_m^{(f)} / \sum_m \sigma_m^{(f)}$ for the distinct Zeeman sublevels in $f = 1$ and $f = 2$ and linear light polarization (along $\mathbf{z}$). We observe a large variability in the relative strength be-

[3]The effective attenuation in the mean-field parameter is only valid to compute expectation values for off-diagonal observables, e.g $F_x^{(f)}$, $F_y^{(f)}$ and $F_\perp^{(f)}$. But should not be used to estimate the expectation values for observables that include diagonal terms, e.g $F_z^{(f)}$ and $N_A^{(f)}$. For a general discussion on depolarization dynamics, we refer to [79].

tween the different $\sigma_m^{(f)}$ for detunings near the $\mathcal{D}_2$-line resonances. On the other hand, for large detunigs, the contribution of each Zeeman substate tends to $\sigma_m^{(f)} \to \lambda^2\Gamma^2/4\pi(\Delta_f)^2$. This implies $\sigma_m^{(f)}/\sum_m \sigma_m^{(f)} \to 1/(2f+1)$, which through Eq. (3.29) describes an equal effective attenuation factor within each hyperfine level.

We use the effective attenuation of the spin order parameter to describe the transverse depolarization, i.e. decay in $F_\perp^{(f)}$, during a dispersive Faraday rotation probing. The effective exponential attenuation in the spin order parameter is translated into an exponential attenuation of $F_\perp^{(f)}$. For weak depolarization, the net effect can be captured by a depolarization constant $N_{L,\mathrm{dep}}^{(f)}$, such that

$$F_\perp^{(f)} = F_{\perp,0}^{(f)}\, e^{-N_L/N_{L,\mathrm{dep}}^{(f)}} , \tag{3.30}$$

where $F_{\perp,0}^{(f)}$ is the transverse spin before the dispersive light-atom interaction. It is important to remark that $N_{L,\mathrm{dep}}^{(f)}$ depends on the particular atomic state described by $\xi_{m,0}^{(f)}$. In this thesis, a large variety of spin states are used, ranging from states that only populate $f=1$ or $f=2$, to superpositions between both. For this reason, we do not calibrate $N_{L,\mathrm{dep}}^{(f)}$, but include it into the Faraday readout analysis as a free fit parameter (see Section 5.3.4).

Similar to the depolarization constant $N_{L,\mathrm{dep}}^{(f)}$, also the hyperfine-dependent scattering lengths $\sigma^{(f)}$ depend on the spin populations. We explicitly compute $\sigma^{(f)}$ for linearly polarized light, where

$$\begin{aligned}
\sigma^{(1)} = \frac{3\lambda^2}{\pi}\Bigg[&\left(\rho_0^{(1)}\frac{1}{6}\right)\frac{1}{1+4(\Delta^{(10')}/\Gamma)^2} \\
&+\left(\rho_{-1}^{(1)}\frac{5}{24}+\rho_1^{(1)}\frac{5}{24}\right)\frac{1}{1+4(\Delta^{(11')}/\Gamma)^2} \\
&+\left(\rho_{-1}^{(1)}\frac{1}{8}+\rho_0^{(1)}\frac{1}{6}+\rho_1^{(1)}\frac{1}{8}\right)\frac{1}{1+4(\Delta^{(12')}/\Gamma)^2}\Bigg] ,
\end{aligned} \tag{3.31a}$$

$$\begin{aligned}
\sigma^{(2)} = \frac{3\lambda^2}{\pi}\Bigg[&\left(\rho_{-1}^{(2)}\frac{1}{40}+\rho_0^{(2)}\frac{1}{30}+\rho_1^{(2)}\frac{1}{40}\right)\frac{1}{1+4(\Delta^{(21')}/\Gamma)^2} \\
&+\left(\rho_{-2}^{(2)}\frac{1}{6}+\rho_{-1}^{(2)}\frac{1}{24}+\rho_1^{(2)}\frac{1}{24}+\rho_2^{(2)}\frac{1}{6}\right)\frac{1}{1+4(\Delta^{(22')}/\Gamma)^2} \\
&+\left(\rho_{-2}^{(2)}\frac{1}{6}+\rho_{-1}^{(2)}\frac{4}{15}+\rho_0^{(2)}\frac{3}{10}+\rho_1^{(2)}\frac{4}{15}+\rho_2^{(2)}\frac{1}{6}\right)\frac{1}{1+4(\Delta^{(23')}/\Gamma)^2}\Bigg] .
\end{aligned} \tag{3.31b}$$

In Fig. 3.6 we evaluate Eqs. (3.31) for transversely oriented states in $f = 1$ and $f = 2$. At the operational points of the Faraday probing, photon absorption is reduced by a factor $\sim 10^{-4}$ with respect to resonance.

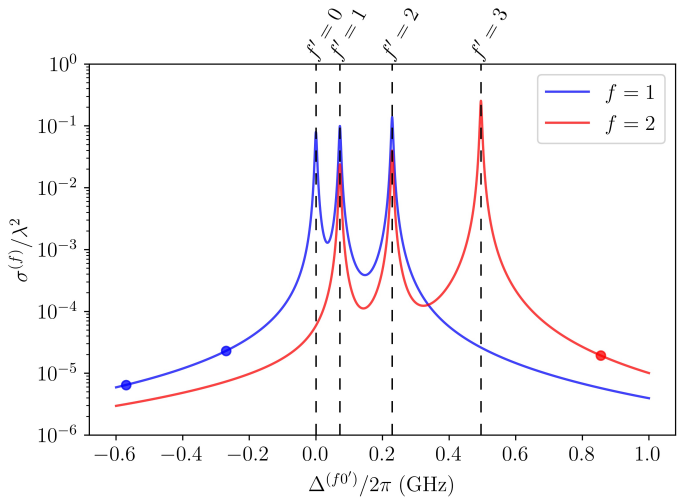

Figure 3.6.: Scattering cross section $\sigma^{(f)}$ in units of λ^2 for $f = 1(2)$ in blue (red) as a function of the detuning referenced to the $f = 1(2) \leftrightarrow f' = 0$ transition. We assume transversely oriented spin states in $f = 1$ or $f = 2$ exclusively, i.e $\rho^{(1)} = (\frac{1}{4}, \frac{1}{2}, \frac{1}{4})$ and $\rho^{(2)} = \mathbf{0}_5$ for the blue curve, while $\rho^{(1)} = \mathbf{0}_3$ and $\rho_m^{(2)} = (\frac{1}{16}, \frac{1}{4}, \frac{3}{8}, \frac{1}{4}, \frac{1}{16})$ for the red one. Dashed lines indicate the position of the excited $f' = \{0, 1, 2, 3\}$ hyperfine levels. The full blue and red circles indicate the operational point for the QND Faraday probing of $f = 1$ and $f = 2$: $\Delta^{(10')}/2\pi \in \{-570\,\mathrm{MHz}, -270\,\mathrm{MHz}\}$ and $\Delta^{(23')}/2\pi = 360\,\mathrm{MHz}$.

3.5. Dynamical evolution

We evaluate the dynamical evolution of the light polarization and the atomic spin in the Heisenberg picture by computing the commutator of the observables of interest and the total light-atom interaction Hamiltonian. In this work, we neglect the coherent back-action onto the atomic ensemble. We assume that the atomic spins are freely evolving and only suffer and exponential damping in the spin amplitude due to off-resonant photon absorption as introduced in Eq. (3.30).

We justify this omission as follows:

(i) From the atomic perspective, the scalar coupling is only relevant for the intense dipole trapping beams and included through the trapping frequencies and attendant effective volume, defined in Eq. (3.17) and Eq. (A.3), respectively. The power, detuning and geometry of the Faraday probe beam result in characteristic transverse trapping frequencies of $|\omega_{x,y}| \sim 2\pi \times 100\,\mathrm{Hz}$ during the Fraday probing. We neglect this contribution because of its short duration $\tau \sim 40\,\mu\mathrm{s}$.

(ii) The vectorial light coupling onto the atomic ensemble is negligible because of two reasons. First, we use linearly polarized Faraday probe beams and thus we have $S_z = 0$. Second, the light propagation direction is perpendicular to the externally applied magnetic field. Hence, the effective magnetic field resulting from a residual circular polarization component is perpendicular to the bias field and can be regarded as a second order perturbation to the LZS.

(iii) We cancel the average contribution of the tensorial light shift on the atomic ensemble by operating the system at the magic angle [77].

Under these assumptions we compute the dynamical evolution of the Stokes operator in the mean-field picture. This is, we use $\partial_t \hat{s}_i = (i\hbar)^{-1}[\hat{s}_i, \sum_{n,f} \hat{H}_{s,n}^{(f)}]$ but express the results in terms of the mean spin orientation $F_i^{(f)} \equiv \langle \hat{f}_i^{(f)} \rangle$ and Stokes vectors $S_i^{(f)} \equiv \langle \hat{s}_i^{(f)} \rangle$:

$$\partial_t S_x = \frac{1}{\tau} \sum_f \left[-G_1^{(f)} S_y F_z^{(f)} + G_2^{(f)} S_z J_y^{(f)} \right] , \tag{3.32a}$$

$$\partial_t S_y = \frac{1}{\tau} \sum_f \left[G_1^{(f)} S_x F_z^{(f)} - G_2^{(f)} S_z J_x^{(f)} \right] , \tag{3.32b}$$

$$\partial_t S_z = \frac{1}{\tau} \sum_f \left[G_2^{(f)} \left(S_y J_x^{(f)} - S_x J_y^{(f)} \right) \right] . \tag{3.32c}$$

It is important to remark that the axis convention of this section does not necessarily coincide with Chapter 2, where the quantization axis of the atomic spin state is set along the external magnetic field. In contrast, in the current section the quantization axis is defined by the light propagation direction. Our particular arrangement of bias fields and probing beams will be introduced in Chapter 5, however we already present here a suitable expression for Eqs. (3.32) in accordance with the chosen coordinate system. We use separate coordinate systems for the atomic (A) and light (L) operators and their cartesian coordinates are

linked as follows:

$$\mathbf{x}_L = \mathbf{y}_A \ , \tag{3.33a}$$

$$\mathbf{y}_L = \mathbf{z}_A \ , \tag{3.33b}$$

$$\mathbf{z}_L = \mathbf{x}_A \ . \tag{3.33c}$$

The time evolution of the Stokes vectors in Eqs. (3.32) is written exclusively in the light reference frame. Combining Eqs. (3.33) and Eqs. (2.17), we can rewrite the atomic spin operators in the atomic reference frame while keeping the Stokes vectors in the light reference frame. This is $F_i \equiv \left[F_i\right]_A$, $J_i \equiv \left[J_i\right]_A$, $S_i \equiv \left[S_i\right]_L$ and the time evolution of the Stokes vectors becomes:

$$\partial_t S_x = \frac{1}{\tau} \sum_f \left[-G_1^{(f)} S_y F_x^{(f)} + G_2^{(f)} S_z J_l^{(f)} \right] \ , \tag{3.34a}$$

$$\partial_t S_y = \frac{1}{\tau} \sum_f \left[G_1^{(f)} S_x F_x^{(f)} + G_2^{(f)} S_z \frac{J_x^{(f)} + \sqrt{3} J_m^{(f)}}{2} \right] \ , \tag{3.34b}$$

$$\partial_t S_z = \frac{1}{\tau} \sum_f \left[G_2^{(f)} \left(-S_y \frac{J_x^{(f)} + \sqrt{3} J_m^{(f)}}{2} - S_x J_l^{(f)} \right) \right] \ . \tag{3.34c}$$

We will refer back to Eqs. (3.34) in Section 5.3.4, which describes the Faraday rotation setup and the resulting input (output) relations between the Stokes vectors describing the probe light polarization before (after) the light atom-interaction.

4

Coherent spin-state manipulation

Coherent manipulations of SBECs take advantage of multi-second coherence and lifetimes [33]. Hence, single- as well as multi-pulse manipulations, with typical timescales below $< 1\,\mathrm{ms}$, are free of loss and decoherence mechanisms. This greatly simplifies the theoretical framework and most mw and rf manipulations are described through rotations or driving of a spin-f system.

This chapter reviews the theoretical framework for coherent spin-f rotations and the dynamics arising from the magnetic dipole interaction between the atomic spins and AC magnetic fields. The discussion is tailored to rf drivings within $f = 1$ and $f = 2$ and to the microwave drivings between them. The highlighted applications are single-pulse and composite-pulse resonant spin manipulations, as well as adiabatic spin manipulations.

4.1. Ground state radiofrequency and microwave transitions in ^{87}Rb

The radiofrequency (rf) transitions within $f = 1$ and $f = 2$, as well as most of the microwave (mw) transitions between hyperfine levels, are magnetically sensitive. This results from the linear and quadratic Zeeman shifts, which affect all Zeeman substates except those with $m = 0$. We write the energy of state $|f, m\rangle$ as $E_m^{(f)}$ and the corresponding coupling resonance frequency between states as $\omega_{0,mm'}^{(ff')} \equiv \hbar^{-1}(E_{m'}^{(f')} - E_m^{(f)})$. In Fig. 4.1 we show resonance frequencies of the rf and mw transitions within and between $f = 1$ and $f = 2$. For simplicity, we have omitted the QZS ($\pm m^2\beta_0 B^2$) and the differential LZS between $f = 1$ and $f = 2$ ($-m\gamma_s B$), which are both negligible for most of the coherent manipulations in this thesis. Within this approximation, the energy splitting between neighbouring Zeeman sublevels $f = 1$ and $f = 2$ are reversed, i.e. $\omega_0^{(1)} \equiv \omega_{0,m\,m+1}^{(11)} = -\omega_0$ and $\omega_0^{(2)} \equiv \omega_{0,m\,m+1}^{(22)} = +\omega_0$, where $\omega_0 = \gamma_0 B$. As regards the interhyperfine transitions, the resonances are spaced by multiples of ω_0 and we use the clock transition $\omega_{0,00}^{(12)} = 2A_{\mathrm{hfs}}/\hbar = 2\pi \times 6834.6\,\mathrm{MHz}$ as reference. Fig. 4.1 also illustrates the required

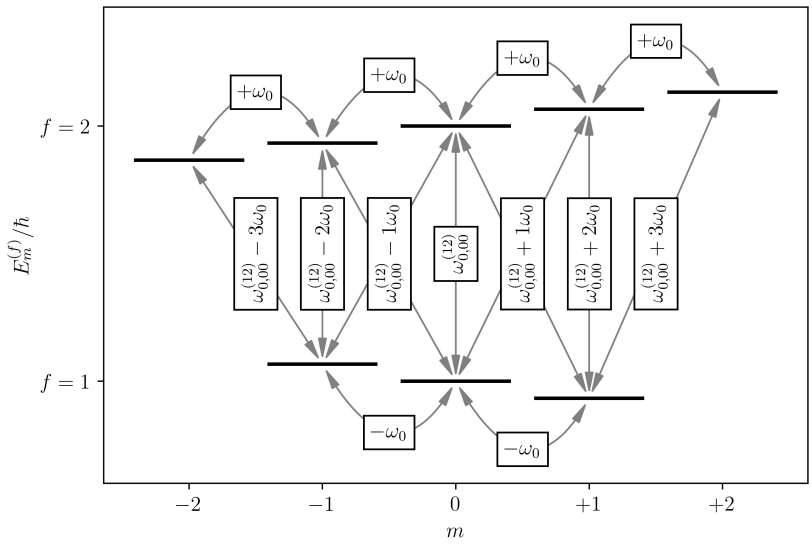

Figure 4.1.: Energy splitting $E_m^{(f)}$ and resonant frequencies for the rf coupling (horizontal labels) and mw coupling (vertical labels). The rf resonance frequencies are $\omega_0^{(1)} = -\omega_0$ and $\omega_0^{(2)} = +\omega_0$ for $f = 1$ and $f = 2$, respectively. The mw resonance frequencies are $\omega_{0,mm'}^{(12)} = \omega_{0,00}^{(12)} + \omega_0(m + m')$. Based on Section 2.2, we have $\omega_0/B = 2\pi \times 700.27\,\mathrm{kHzG^{-1}}$ and $\omega_{0,00}^{(12)} = 2A_{\mathrm{hfs}}/\hbar = 2\pi \times 6834.6\,\mathrm{MHz}$. Energy levels spacing are not to scale.

change in angular momentum for the distinct transitions. Rf transitions between neighbouring Zeeman sublevels increase or decrease by one quantum the angular momentum along the quantization axis and couple to the circular polarization components of the driving fields. The situation is different for the mw driving, where the polarization depends on the particular transition $|1, m\rangle \leftrightarrow |2, m'\rangle$. The driving field has to include σ^-, π or σ^+ polarization components for $m' = m - 1$, $m' = m$ or $m' = m + 1$.

4.2. Magnetic rf drivings within hyperfine manifolds

In this section we study the magnetic coupling to transverse oscillating magnetic fields within a single hyperfine manifold. By keeping the spin of the system as a

free parameter f the results equally apply to $f = 1$ and $f = 2$.

The linear magnetic interaction Hamiltonian for a spin-f system embedded in a DC magnetic field (along $\mathbf{z}$) and a transverse AC driving field (within $\mathbf{x} - \mathbf{y}$ plane) reads:

$$\hat{H}_B^{(f)} = \hbar\gamma^{(f)}\mathbf{B}\cdot\hat{\mathbf{f}}^{(f)} \,, \tag{4.1a}$$

$$\mathbf{B} = \left(\tilde{B}_x\cos(\omega t+\phi_x), \tilde{B}_y\cos(\omega t+\phi_y), B_z\right)^T \,, \tag{4.1b}$$

where B_i, $\tilde{B}_i$ and ϕ_i are the DC field amplitude, AC field amplitude and phase offset along $i \in \{x, y, z\}$. The gyromagnetic ratio $\gamma^{(f)}$ has been defined in Eq. (2.12) and the driving frequency is, for simplicity, positive defined $\omega > 0$.

The Hamiltonian above is more conveniently expressed when using a circular basis set for the transverse magnetic fields. To this end, we introduce the subscripts $+$ and $-$ to label circular σ^+ and σ^- field components and rewrite Eqs. (4.1) as

$$\begin{aligned}\hat{H}_B^{(f)} = \frac{\hbar\gamma^{(f)}}{2}\Big[B_z\hat{f}_z^{(f)} + \Big(&\tilde{B}_+ e^{i(+\omega t+\phi_+)} \\ &+ \tilde{B}_- e^{i(-\omega t+\phi_-)}\Big)\Big(\hat{f}_x^{(f)} - i\hat{f}_y^{(f)}\Big)\Big] + \text{h.c.} \,,\end{aligned} \tag{4.2a}$$

$$\begin{bmatrix}\tilde{B}_+ e^{+i\phi_+}\\ \tilde{B}_- e^{-i\phi_-}\end{bmatrix} = \frac{1}{2}\begin{bmatrix}1 & +i\\ 1 & -i\end{bmatrix}\begin{bmatrix}\tilde{B}_x e^{i\phi_x}\\ \tilde{B}_y e^{i\phi_y}\end{bmatrix} \,. \tag{4.2b}$$

We distinguish three separate contributions to the Hamiltonian in Eq. (4.2a). First, the $\propto B_z$ term is responsible for rapid Larmor precession around the applied DC magnetic field at a frequency $\omega_0^{(f)} = \gamma^{(f)}B_z$. This frequency is typically known as the resonance frequency. Second and third, the $\propto\tilde{B}_+$ and $\propto\tilde{B}_-$ terms describe circularly polarized transverse rf fields rotating at a frequency $+\omega$ (σ_+ polarization) and $-\omega$ (σ_- polarization), respectively. Near the resonance frequency $|(\omega - \omega_0^{(f)})/\omega_0^{(f)}| \ll 1$, only the σ_+ (σ_-) component contribute to the dynamics for $\omega_0^{(f)} > 0$ ($\omega_0^{(f)} < 0$), while the σ_- (σ_+) component is typically neglected by means of the Rotating Wave Approximation (RWA) [44]. Under this approximation, the time dependence in Eq. (4.2a) can be removed by introducing a reference frame that co-rotates with the $\tilde{B}_+$ ($\tilde{B}_-$) field. The Hamiltonian in the rotating frame reads:

$$\left[\hat{H}_B^{(f)}\right]_{\text{rot}} = \hbar\Omega_\pm^{(f)}\mathbf{u}_\pm^{(f)}\cdot\hat{\mathbf{f}}^{(f)} \,, \tag{4.3a}$$

$$\Omega_\pm^{(f)} = \sqrt{\left(\Omega_{0,\pm}^{(f)}\right)^2 + \left(\Delta_\pm^{(f)}\right)^2} \,, \tag{4.3b}$$

$$\Omega_{0,\pm}^{(f)} = \gamma^{(f)} \tilde{B}_{\pm} \ , \tag{4.3c}$$

$$\Delta_{\pm}^{(f)} = \pm\omega - \omega_0^{(f)} \ , \tag{4.3d}$$

$$\mathbf{u}_{\pm}^{(f)} = \frac{1}{\Omega_{\pm}^{(f)}} \left(\Omega_{0,\pm}^{(f)} \cos(\phi_{\pm}), \Omega_{0,\pm}^{(f)} \sin(\phi_{\pm}), -\Delta_{\pm}^{(f)} \right)^T \ , \tag{4.3e}$$

where the + (−) subscript applies for $\omega_0^{(f)} > 0$ ($\omega_0^{(f)} < 0$). The dynamics introduced by Eq. (4.3a) corresponds to an effective rotation around the unit vector $\mathbf{u}_{\pm}^{(f)}$ at a rate given by the generalized Rabi frequency $\Omega_{\pm}^{(f)}$. The generalized Rabi frequency is expressed in terms of the detuning $\Delta_{\pm}^{(f)}$ and the resonant Rabi frequency $\Omega_{0,\pm}^{(f)}$.

4.3. Magnetic mw drivings between hyperfine manifolds

The interaction between the spin state and the external magnetic fields is captured by the hyperfine and magnetic Hamiltonian in Eq. (2.9). While for rf transitions within hyperfine manifolds it suffices to consider the LZS (see Eqs. (4.1)), this simplification does not apply to mw transitions between manifold. For a general magnetic field $\mathbf{B}$, the matrix representation of the hyperfine and magnetic Hamiltonian becomes:

$$\begin{aligned} \langle f, m | \, \hat{H}_{\text{hfs}} + \hat{H}_B \, | f', m' \rangle \approx & A_{\text{hfs}} \left[\frac{f(f+1)}{2} - 2 \right] \delta_{f,f'} \delta_{m,m'} \\ & + \mu_B \sum_{\substack{m_s, m_i \\ m_s', m_i'}} \langle 1/2, m_s | \, \mathbf{B} \cdot \hat{\sigma} \, | 1/2, m_s' \rangle \mathcal{C}_{s,m_s,i,m_i}^{f',m'} \mathcal{C}_{s,m_s,i,m_i}^{f,m} \ , \end{aligned} \tag{4.4}$$

where $\hat{\sigma} = (\hat{\sigma}_x, \hat{\sigma}_y, \hat{\sigma}_z)^T$ is the Pauli vector and $\mathcal{C}_{s,m_s,i,m_i}^{f,m} = \langle s, m_s, i, m_i | f, m \rangle = \langle f, m | s, m_s, i, m_i \rangle$ are the real-valued Clebsch-Gordan coefficients. The summation is taken over $m_s, m_s' \in \{-s, s\}$ and $m_i, m_i' \in \{-i, ..., i\}$ for $s = 1/2$ and $i = 3/2$. Note, that we have shifted the overall energy to yield a symmetric hyperfine splitting between $f = 1$ and $f = 2$, and we have approximated $g_s \approx 2$ and $g_i \approx 0$. This simplification results in a $\sim 10^{-3}$ change in the matrix elements, which is negligible for the purpose of this section.

A further simplification applies for interhyperfine transitions between $f = 1$ and $f = 2$, where Eq. (4.4) can be rewritten in terms of pseudo spin-$\frac{1}{2}$ subsystems,

spanned by the ground and excited states $|g\rangle \equiv |1,m\rangle$ and $|e\rangle \equiv |2,m'\rangle$. The Hamiltonian of such a spin-$\frac{1}{2}$ system reads:

$$\hat{H}^{(12)}_{mm'} = \hbar\omega^{(12)}_{0,mm'}\hat{f}^{(\frac{1}{2})}_z + \mu_B \sum_i B_i \left(\alpha^{(12)}_{i,mm'}\hat{f}^{(\frac{1}{2})}_x + \beta^{(12)}_{i,mm'}\hat{f}^{(\frac{1}{2})}_y\right). \tag{4.5}$$

The summation is taken over $i \in \{x,y,z\}$ and the terms $\alpha^{(12)}_{i,mm'}$ and $\beta^{(12)}_{i,mm'}$ scale the interaction to the magnetic field components. This representation is particularly suited to obtain the couplings to the different magnetic field polarizations and the corresponding resonant Rabi frequency $\Omega^{(12)}_{0,mm'}$. When $\alpha^{(12)}_{i,mm'} = \alpha\delta_{i,x}$ and $\beta^{(12)}_{i,mm'} = \pm\alpha\delta_{i,y}$, the transition couples to transverse $\sigma^{\pm}$ drivings and $\Omega^{(12)}_{0,mm'} = \mu_B\alpha\tilde{B}_{\pm}/\hbar$. Similarly, when $\alpha^{(12)}_{i,mm'} = \alpha\delta_{i,z}$ while $\beta^{(12)}_{i,mm'} = 0$, the transition couples to longitudinal π drivings and $\Omega^{(12)}_{0,mm'} = \mu_B\alpha\tilde{B}_z/2\hbar$. The magnetic couplings and resonant Rabi frequencies for the full set of $f = 1$ and $f = 2$ hyperfine transitions are listed in Table 4.1.

In analogy to the rf drivings within $f = 1$ and $f = 2$, we can introduce a rotating frame to describe mw drivings for every spin-$\frac{1}{2}$ subsystem. In this case,

$\|g\rangle$	$\|e\rangle$	$\alpha^{(12)}_{i,mm'}$	$\beta^{(12)}_{i,mm'}$	Pol.	$\hbar\Omega^{(12)}_{mm'}/\mu_B$
$\|1,+1\rangle$	$\|2,+2\rangle$	$-\sqrt{3}\delta_{i,x}$	$-\sqrt{3}\delta_{i,y}$	σ^+	$-\tilde{B}_+\sqrt{3}$
$\|1,0\rangle$	$\|2,+1\rangle$	$-\sqrt{3/2}\delta_{i,x}$	$-\sqrt{3/2}\delta_{i,y}$	σ^+	$-\tilde{B}_+\sqrt{3/2}$
$\|1,-1\rangle$	$\|2,0\rangle$	$-\sqrt{1/2}\delta_{i,x}$	$-\sqrt{1/2}\delta_{i,y}$	σ^+	$-\tilde{B}_+\sqrt{1/2}$
$\|1,+1\rangle$	$\|2,0\rangle$	$+\sqrt{1/2}\delta_{i,x}$	$-\sqrt{1/2}\delta_{i,x}$	σ^-	$+\tilde{B}_-\sqrt{1/2}$
$\|1,0\rangle$	$\|2,-1\rangle$	$+\sqrt{3/2}\delta_{i,x}$	$-\sqrt{3/2}\delta_{i,y}$	σ^-	$+\tilde{B}_-\sqrt{3/2}$
$\|1,-1\rangle$	$\|2,-2\rangle$	$+\sqrt{3}\delta_{i,x}$	$-\sqrt{3}\delta_{i,y}$	σ^-	$+\tilde{B}_-\sqrt{3}$
$\|1,-1\rangle$	$\|2,-1\rangle$	$+\sqrt{3}\delta_{i,z}$	0	π	$+\tilde{B}_z\sqrt{3}/2$
$\|1,0\rangle$	$\|2,0\rangle$	$+2\delta_{i,z}$	0	π	$+\tilde{B}_z$
$\|1,+1\rangle$	$\|2,+1\rangle$	$+\sqrt{3}\delta_{i,z}$	0	π	$+\tilde{B}_z\sqrt{3}/2$

Table 4.1.: Microwave transitions and magnetic couplings between the $f = 1$ and $f = 2$ hyperfine manifolds. The values for $\alpha^{(12)}_{i,mm'}$ and $\beta^{(12)}_{i,mm'}$ have been obtained by casting Eq. (4.4) into effective spin-$\frac{1}{2}$ subsystems described by Eq. (4.5). Based on these, the resonant polarization (σ^+, σ^- or π) and resonant Rabi frequency ($\Omega^{(12)}_{0,mm'}$) are obtained.

we get:

$$\left[\hat{H}^{(12)}_{mm'}\right]_{\text{rot}} = \hbar\Omega^{(12)}_{mm'}\mathbf{u}^{(12)}_{mm'}\cdot\hat{\mathbf{f}}^{(\frac{1}{2})} \ , \tag{4.6a}$$

$$\Omega^{(12)}_{mm'} = \sqrt{\left(\Omega^{(12)}_{0,mm'}\right)^2 + \left(\Delta^{(12)}_{mm'}\right)^2} \ , \tag{4.6b}$$

$$\Delta^{(12)}_{mm'} = \omega - \omega^{(12)}_{mm'} \ , \tag{4.6c}$$

$$\mathbf{u}^{(12)}_{mm'} = \frac{1}{\Omega^{(12)}_{mm'}}\left(\Omega^{(12)}_{0,mm'}\cos(\phi_{\pm,z}), \Omega^{(12)}_{0,mm'}\sin(\phi_{\pm,z}), -\Delta^{(12)}_{mm'}\right)^T \ , \tag{4.6d}$$

where the applied magnetic field is of the form $\mathbf{B} = (\tilde{B}_+\cos(\omega t+\phi_+), \tilde{B}_+\sin(\omega t+\phi_+), B_z)^T$, $\mathbf{B} = (\tilde{B}_-\cos(\omega t+\phi_-), \tilde{B}_-\sin(-\omega t+\phi_-), B_z)^T$ or $\mathbf{B} = (0, 0, B_z + \tilde{B}_z\cos(\omega t+\phi_z))$ for σ^+, σ^- or π drivings, respectively. The overall interpretation and dynamics resulting from Eqs. (4.6) are equivalent to the rf drivings described below Eqs. (4.3).

4.4. Resonant and off-resonant coherent manipulations

We have seen that, within the rotating frame, the magnetic rf and mw interaction have analogous Hamiltonians. For this reason, in the rest of this chapter we will simplify the notation and write Eqs. (4.3) and Eqs. (4.6) as

$$\left[\hat{H}\right]_{\text{rot}} = \hbar\Omega\mathbf{u}\cdot\hat{\mathbf{f}} \ , \tag{4.7a}$$

$$\Omega = \sqrt{\Omega_0^2 + \Delta^2} \ , \tag{4.7b}$$

$$\mathbf{u} = \frac{1}{\Omega}\left(\Omega_0\cos(\phi), \Omega_0\sin(\phi), -\Delta\right)^T \ , \tag{4.7c}$$

where, $\hat{\mathbf{f}}$ is a spin $f = 1, 2$ operator for rf drivings and a spin $f = \frac{1}{2}$ operator for mw drivings. A more intuitive representation of the dynamics can obtained for the normalized spin projections $f_i \equiv F_i^{(f)}/fN_A$, which follow the equation of motion of a classical rotor:

$$\partial_t\left[\mathbf{f}\right]_{\text{rot}} = \Omega\mathbf{u}\times\left[\mathbf{f}\right]_{\text{rot}} \ , \tag{4.8}$$

Contrary to the Hamiltonian in Eqs. (4.7), which is described in terms of $(2f + 1)\times(2f + 1)$ dimensional spin matrices, the normalized spin equation of motion in Eq. (4.8) does not alter its structure for distinct f quantum numbers and is suited to visualize coherent manipulations regardless of the underlying spin manifold. For observables that are invariant under $\mathbf{z}$ rotations (see discussion

below Eq. (2.19)) we omit the subscript indicating the reference frame, which in this chapter applies to f_z and $f_\perp$.

The dynamics resulting from rf and mw couplings can be described through an effective rotation, where both the rotation axis and the rotation speed are influenced by the detuning $\Delta = \omega - \omega_0$. While the stability of the driving frequency ω and the resonant Rabi frequency Ω_0 are inherited from the rf and mw synthesizer of the experiment, the resonant frequency ω_0 generally depend on the applied magnetic field. Magnetic field fluctuation and the resulting fluctuations in the detuning strongly affect the outcome of coherent spin manipulations.

In the following, we illustrate the effect of distinct detunings on the coherent driving of spin ensembles. To this purpose, we assume all spins initially oriented along $\mathbf{f}(t=0) = (0,0,-1)^T$ and use Eq. (4.8) for the spin dynamics in f_z:

$$f_z(t) = -1 + 2\left[\frac{\Omega}{\Omega_0}\sin\left(\frac{\Omega t}{2}\right)\right]^2 . \tag{4.9}$$

For a resonant driving, Eq. (4.9) describes full oscillation cycles between $f_z = \pm 1$ at a frequency $\Omega = \Omega_0$. On the other hand, for detunigs $\Delta \neq 0$, the oscillation cycles decrease in amplitude but increase their frequency.

In Fig. 4.2 we evaluate the dependency on the detuning in f_z and $f_\perp$. Results are shown for $\Omega_0 t = \pi$ and $\Omega_0 t = \pi/2$, corresponding to a resonant π rad and $\pi/2$ rad rotation of the initial spin. Rf and mw pulses with the above durations are commonly known as π and $\pi/2$ pulses, respectively. We observe that the stability order[1] of f_z for π pulses is $\mathcal{O}(\Delta/\Omega_0)^2$, while for $f_\perp$ and $\pi/2$ pulses the stability order is $\mathcal{O}(\Delta/\Omega_0)^4$.

4.4.1. Composite spin manipulations

So far we have focused on single pulse manipulations and the attendant rotations in the spin orientation. An extension are composite rotations [81], formed by sequences of rf and mw pulse with distinct length and relative phase relations. We target two applications of such pulse sequences.

The first one is the generation of effective rotations where a particular subset of spin observables is stabilized against perturbations. In particular, they palliate fluctuations and inhomogeneities in the driving field and its detuning [82, 83]. In Table 4.2 we show single pulses and composite pulses with an equivalent net rotation of π and $\pi/2$ rad. We write individual rotations as $R_\alpha[\beta]$, where β is the rotation angle and α is the azimuth angle of the rotation axis. For a π and $\pi/2$ rotation around $\mathbf{x}$, we have $R_0[\pi]$ and $R_0[\pi/2]$, or equivalently $R_0[180]$ and $R_0[90]$ when expressing the angles in degrees.

[1] Order of the first non-zero derivative $\partial^n(f_i)/\partial(\Delta)^n \neq 0$ evaluated at $\Delta = 0$.

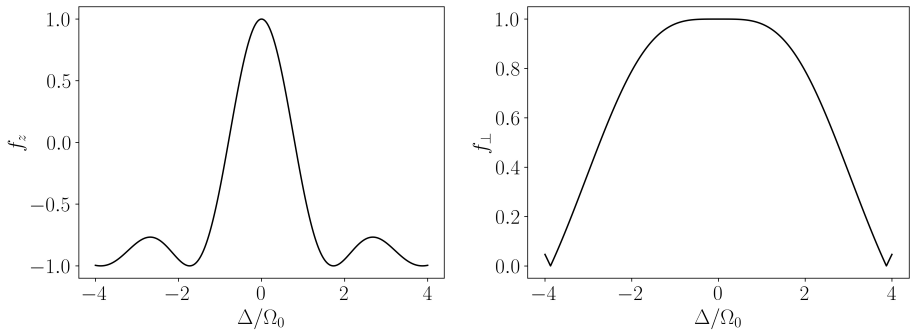

Figure 4.2.: Dependence of f_z (left) and $f_\perp$ (right) on the detuning for a π (left) and $\pi/2$ (right) pulses applied to a spin system initially oriented along $-\mathbf{z}$.

Deviations from ideal π and $\pi/2$ pulses are primarily caused by magnetic field drifts that move the driving out of resonance $\Delta \neq 0$. We quantify this effect by the deviation angle χ, which is the angle between the obtained $\mathbf{f}|_{\Delta\neq 0}$ and the ideal $\mathbf{f}|_{\Delta=0}$ spin orientations. In Table 4.2 we show the detuning range for which $\chi \leqslant 10\,\text{deg}$, which is our metric for the performance of the distinct pulse sequences.

The performance of these composite pulse sequences is also given in Fig. 4.3, where besides the spin projections f_z and $f_\perp$ we shown the angular deviation χ. For small detunings $|\Delta/\Omega_0| \ll 1$ the composite pulse sequences show a reduced

Label	Net rotation	Sequence ($\leftarrow$)	Stability range (Δ/Ω_0)
$\mathcal{R}_\pi$	π	$R_0[180]$	± 0.09
$\mathcal{R}_\text{I}$	π	$R_0[315]R_{180}[225]R_0[90]$	± 0.23
$\mathcal{R}_\text{II}$	π	$R_{180}[59]R_0[298]R_{180}[59]$	± 0.69
$\mathcal{R}_{\pi/2}$	$\pi/2$	$R_0[90]$	± 0.17
$\mathcal{R}_\text{III}$	$\pi/2$	$R_0[25]R_{180}[320]R_0[385]$	± 0.36

Table 4.2.: Single and composite π and $\pi/2$ pulses [81]. Individual rotations are written as $R_\alpha[\beta]$, where β is the rotation angle and α is the azimuth angle of the rotation axis (in degrees). Composite pulse sequences are read in inverse order, from right to left ($\leftarrow$). The stability range is defined as the interval of detunings for which the angle between $\mathbf{f}|_{\Delta\neq 0}$ and $\mathbf{f}|_{\Delta=0}$ is $\chi \leqslant 10\,\text{deg}$.

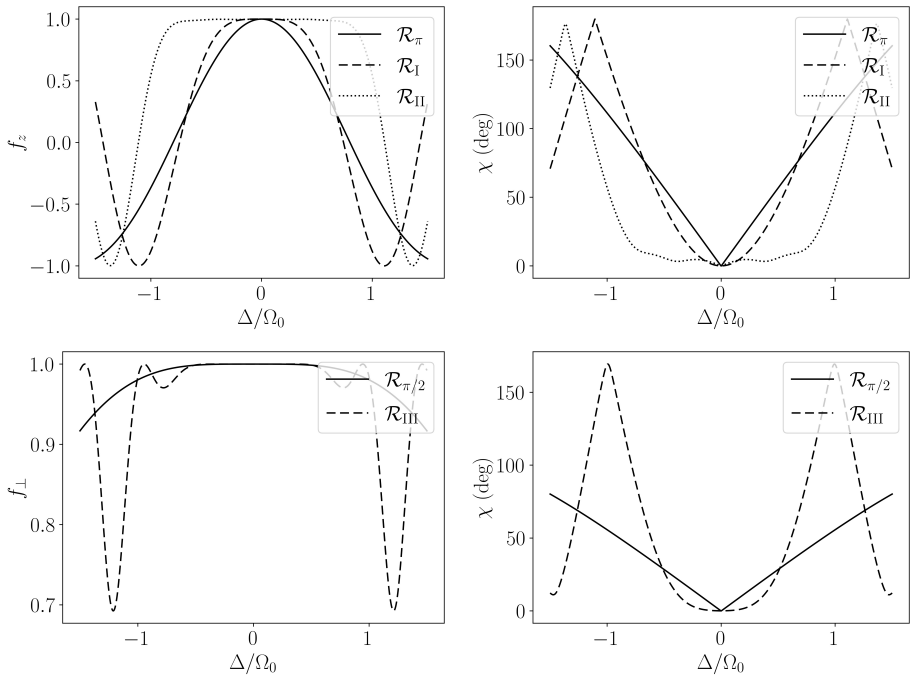

Figure 4.3.: Dependence of f_z and χ on detuning for the pulse sequences described in Table 4.2. The upper charts show single and composite π pulses, the lower charts are devoted to single and composite $\pi/2$ pulses. Note that the composite pulses sequences relocate the instabilities in the detuning from $|\Delta/\Omega_0| \ll 1$ to $|\Delta/\Omega_0| \gtrsim 1$.

variance in the spin projections and angular deviations. On the other hand, when $|\Delta/\Omega_0| \gtrsim 1$, the situation is reversed. More generally, the stabilization resulting from composite pulses can be understood as a rearrangement in the sensitivity of the system, where instabilities are transferred to minor spectral regions or minor spin observables.

A second example of multi-pulse resonant rf and mw sequences is the manipulation of the azimuthal spin pointing angle $\theta = \arctan2(f_x, f_y)$. A change in the azimuthal spin pointing angle is equivalent to a rotation around the quantization axis ($\mathbf{z}$). This is generally not possible through a single resonant driving pulse but can be achieved via two resonant π pulses. We write these pulses as $R_{\alpha_A}[180]$ and $R_{\alpha_B}[180]$. The composite pulse sequence[2] $R_{\alpha_B}[\pi]R_{\alpha_A}[\pi]$ results

[2]Composite pulse sequences are read in inverse order, from right to left (←).

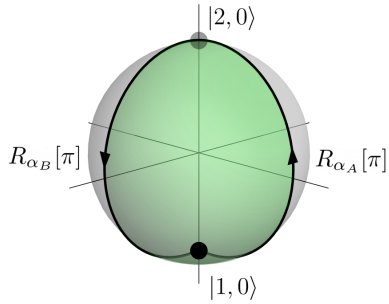

Figure 4.4.: Bloch Sphere representation of the spin trajectory resulting from two consecutive π pulses between states $|1,0\rangle$ and $|2,0\rangle$ (pseudo-spin $\frac{1}{2}$ system). The initial spin state is $|1,0\rangle$ (opaque dot) and the first rotation $R_{\alpha_A}[\pi]$ is an ascending spin trajectory towards the intermediate state $|2,0\rangle$ (translucent dot). The second spin rotation $R_{\alpha_B}[\pi]$ moves the state back to $|1,0\rangle$. The rotation axes have been adjusted to $\alpha_B - \alpha_A = \pi/2$ and the enclosed solid angle (green area) is $\mathcal{S} = \pi$. The resulting transformation for the $\xi_0^{(f)}$ component reads $\xi_0^{(1)} \to \xi_0^{(1)} \times \exp[-i\mathcal{S}/2] = -i\xi_0^{(1)}$.

in a rotation around $\mathbf{z}$ by an angle $\theta = 2(\alpha_B - \alpha_A)$, where $\alpha_B - \alpha_A$ is adjusted through the phase difference between the two applied AC fields.

The same pulse sequence can be used to perform phase manipulations on individual spin components of $f = 1$ and $f = 2$. We will illustrate the process for a SBEC in $f = 1$ and a phase manipulation of the $\xi_0^{(1)}$ component. To this end, the $R_{\alpha_B}[\pi]R_{\alpha_A}[\pi]$ pulse sequence is applied on the mw clock transition between $|1,0\rangle$ and $|2,0\rangle$. The transformation of the $\xi_0^{(1)}$ component reads[3] $\xi_0^{(1)} \to \xi_0^{(1)} \times \exp[i\pi + i(\alpha_B - \alpha_A)]$. An application of the phase manipulation of the $\xi_0^{(1)}$ component is the coherent driving between oriented ($F^{(1)} = N_A^{(1)}$) and aligned states ($F^{(1)} = 0$), e.g. between $\xi^{(1)}/\sqrt{N_A^{(1)}} = (1/2, \pm 1/\sqrt{2}, 1/2)^T$ and $\xi^{(1)}/\sqrt{N_A^{(1)}} = (1/2, \pm i/\sqrt{2}, 1/2)^T$.

In Fig. 4.4 we show the spin trajectory for the phase manipulation of the $\xi_0^{(1)}$ component. We note that it forms a closed path and that the transformation of $\xi_0^{(1)}$ can be equally written in terms of a geometric phase given by the enclosed

[3]Note that we operate within a spin-$\frac{1}{2}$ system, which yields a factor 1/2 between the evolution of the azimuthal spin pointing angle $\theta = 2(\alpha_B - \alpha_A)$ and the evolution of the ground state phase $\arg(\xi_0^{(1)}) = \pi + \alpha_B - \alpha_A$, i.e. $\partial_\theta \arg(\xi_0^{(1)}) = 1/2$.

solid angle $\mathcal{S}$ [84, 85, 86]. Using the geometric phase we have $\xi_0^{(1)} \rightarrow \xi_0^{(1)} \times \exp[-i\mathcal{S}/2]$, which applies to any arbitrary closed spin trajectory on a spin-$\frac{1}{2}$ Bloch Sphere.

4.4.2. Adiabatic spin manipulations

In contrast to resonant spin manipulations, off-resonant spin manipulations engineer variable detunings to achieve a robust spin population transfers through adiabatic passages. The technique was first introduced in the pioneering NMR experiments of Felix Bloch *et al.* [87] and is based on an adiabatic sweep in the detuning which inverts the spin populations of the system [88].

In the limit of large detunings, the atomic spins and the oscillating field are uncoupled and the Hamiltonian in Eqs. (4.7) becomes $[\hat{H}]_{\rm rot} \approx -\hbar\Delta\hat{f}_z$. We write the eigensates as $|f,m\rangle$ and their associated eigenenergies as $E_m^{(f)} = -\hbar\Delta m$. The list of sorted eigenenergies reads $[E_{-f}^{(f)}, E_{-f+1}^{(f)}, ..., E_f^{(f)}]$ for $\Delta < 0$ and $[E_f^{(f)}, E_{f-1}^{(f)}, ..., E_{-f}^{(f)}]$ for $\Delta > 0$. More generally, the sorted eigenstates reverse their order when going from negative to positive detunigs and vice-versa.

This feature is used in adiabatic passages [89, 90, 91] to achieve spin population inversion. In an adiabatic passage from $\Delta/\Omega_0 \ll 0$ to $\Delta/\Omega_0 \gg 0$ (or vice-versa) the system remains in the instantaneous eigenestates of $[\hat{H}]_{\rm rot}$. The result is a population inversion of type $N_m^{(f)} \leftrightarrow N_{-m}^{(f)}$, where $N_m^{(f)}$ is the spin population of the state $|f,m\rangle$.

In Fig. 4.5 we show the eigenenergies of the coupling Hamiltonian as a function of detuning. The eigenenergies highlight the connection between $|f,m\rangle$ to the $|f,-m\rangle$ states when an adiabatic change in the detuning is performed. We also observe that the spacing between energy levels decrease as we approach resonance. This is of particular importance in the design of adiabatic sweeps and for setting an upper bound to the sweep rate. We make use of the work introduced by Landau and Zener [92, 93], which evaluates the probability of an adiabatic transition in a two-level system ($f = \frac{1}{2}$) under a linear sweep in detuning. This reads [88]:

$$P_{\rm adb} = 1 - \exp\left(\frac{-2\pi(\hbar\Omega_0/2)^2}{\hbar|\partial_t(E_e - E_g)|}\right) , \tag{4.10}$$

where $P_{\rm adb}$ is the probability of an adiabatic transition between states $|g\rangle$ and $|e\rangle$, $E_e - E_g$ the energy difference between them and $\hbar\Omega_0/2$ is the off-diagonal element of the two-level system's Hamiltonian. We can use Eqs. (4.7) to rewrite the energy difference in the limit of large detunigs $|E_e - E_g| \approx \hbar|\Delta|$. Under this

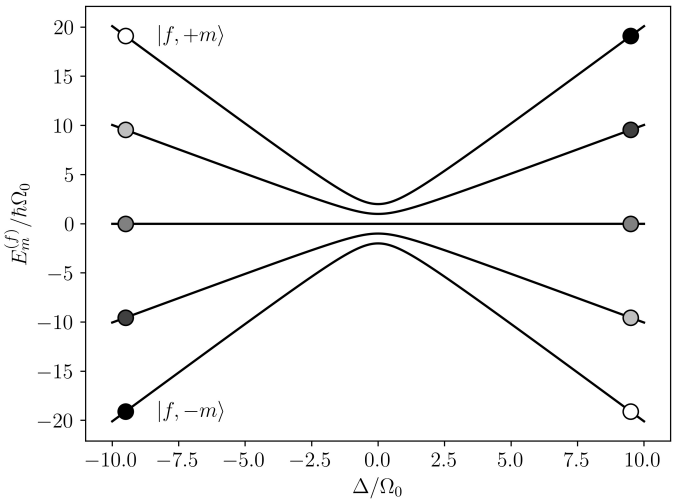

Figure 4.5.: Eigenenergies $E_m^{(f)}$ of the magnetic coupling Hamiltonian in the rotating frame (Eq. (4.3a)) as a function of detuning Δ. In the limit of large detunings $|\Delta/\Omega_0| \gg 1$ the eigenstates of the system correspond to the bare states $|f, m\rangle$. We use gray scale coding to pictorially represent the distinct bare states at the left and right side of the figure. Note that their orders are reversed and the populations inverted $N_m^{(f)} \leftrightarrow N_{-m}^{(f)}$ when adiabatically driving the system from negative to positive detunings and vice-versa.

approximation, an adiabatic transfer with $P_{\mathrm{adb}} \gtrsim 1 - \epsilon$ is guaranteed for

$$\frac{2\pi \left(\hbar\Omega_0/2\right)^2}{\hbar^2 |\partial_t \Delta|} \gtrsim -\ln(\epsilon) \quad \rightarrow \quad |\partial_t \Delta| \lesssim -\frac{\pi \left(\Omega_0\right)^2}{2\ln(\epsilon)} \,, \tag{4.11}$$

where $|\partial_t \Delta|$ is the detuning sweep rate. While the adiabatic transition probability in Eq. (4.10) was originally computed for $f = \frac{1}{2}$, we can use Eq. (4.11) also in higher spin system for choosing appropriate sweep rates and avoiding couplings between neighbouring Zeeman substates. Furthermore, we can use this expression to compare the adiabatic sweep time t_{adb} and the duration of a resonant π pulse t_π. For a linear sweep in detuning in the range $\Delta/\Omega_0 \in [-\eta, +\eta]$ we obtain:

$$t_{\mathrm{adb}}/t_\pi > -\frac{4\eta \ln(\epsilon)}{\pi^2} \,. \tag{4.12}$$

For a typical sweep range $\eta \sim 10$ (as given in Fig. 4.5) and $\epsilon \sim 0.01$ we get

$t_{\mathrm{adb}}/t_{\pi} \gtrsim 20$. Hence, adiabatic transfers are significantly slower than the corresponding resonant manipulations, which is a fundamental drawback of this technique. Additionally, spin superpositions undergoing an adiabatic sweep do not mantain their original phase relation. The new phase relation depends on the difference in the dynamical phase as well as on the Berry phase acquired by each spin component [91, 94].

5
Experimental setup

The experimental apparatus this work is based on was started in 2012. During the subsequent 3 years, the former PhD students Silvana Palacios and Simon Coop did an exceptional work and by the time I joined ICFO (late 2015) the experiment was very close to achieve condensation. In fact, we observed the first BEC signatures a few months later. From that point on, I had the priviledge to work in the ultracold regime and develop hardware, firmware and software for the control and manipulation of our spinor BEC.

This chapter starts with a general overview of the experimental setup but is manly devoted to the improvements and new developments in the context of this thesis. They are classified as improvements in the magnetic control of the atomic ensemble and improvements in the optical manipulation and probing. The first ones include an active magnetic field stabilization and the synthesis of radiofrequency (rf) and microwave (mw) fields. The second type of improvements include a pulsed loading scheme for the optical dipole trap, a purification scheme for the optical evaporation, the digitization of the laser locking scheme and the development of a hyperfine-selective Faraday probing scheme. Detailed discussions on the pre-existing setup and capabilities can be found in [95, 96].

5.1. General overview

In this section we review the basic capabilities of the experimental apparatus. The core of every ultracold quantum gas experiment is its vacuum system, which for this experimental work is shown in Fig. 5.1. The atomic ensembles are trapped and cooled inside a $\varnothing = 115.8\,\mathrm{mm}$ wide octagonal glass cell, offering an exceptional optical access. The pressure of the system is lowered to $\sim 1 \times 10^{-11}\,\mathrm{mbar}$ by means of an ion pump. The strong magnetic field of the ion pump is contained by a custom μ-metal shielding. The atoms are sourced from enriched ^{87}Rb dispensers powered via electrical feedthroughs.

Magnetic pairs of coils along each spatial direction encapsulate the octagonal glass cell and produce up to $\sim 1\,\mathrm{G}$ for compensating the Earth's magnetic field

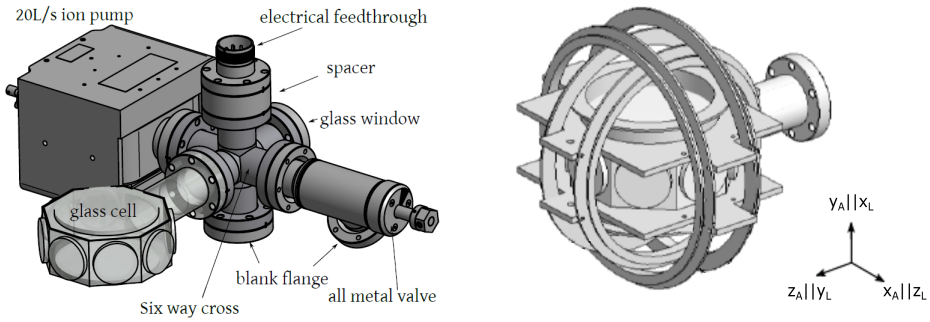

Figure 5.1.: Full vacuum system (left) and detailed view of the octagonal glass cell (right) including magnetic field coils. We label as $\{\mathbf{x}_A, \mathbf{y}_A, \mathbf{z}_A\}$ and $\{\mathbf{x}_L, \mathbf{y}_L, \mathbf{z}_L\}$ the atomic and Faraday probing reference frames, respectively. Images adapted from [95].

and defining the quantization axis of the experiment. Not shown here is an additional pair of Helmholtz coils which are used to actively cancel magnetic field fluctuations along the $\mathbf{z}_A$ direction (Section 5.2.1). Superposed to the bias coils along $\mathbf{y}_A$, a pair of coils connected in anti-Helmholtz configuration are used to generate the quadrupole magnetic field (linear gradient) for the magneto-optical trap (MOT) and Stern-Gerlach imaging. Additional rf (Section 5.2.2) and mw (Section 5.2.3) driving allow to manipulate the atomic spin state.

The laser beams used for cooling, trapping and probing the atomic ensemble are shown in Fig. 5.2. Based on their geometry, we distinguish between collimated ($w_0 \gtrsim 5\,\text{mm}$) and focused ($w_0 \lesssim 50\,\mu\text{m}$) beams. The first corresponds to the three counter-propagating pairs of beams for the MOT and the absorption imaging beam, which propagates along $(1,1,0)_A^T$, i.e. $(1,0,1)_L^T$. On the other hand, the focused light beams are coplanar within $\mathbf{x}_A$-$\mathbf{z}_A$, i.e. $\mathbf{z}_L$-$\mathbf{y}_L$. They are formed by the three optical dipole traps (ODT 1,2,3), the optical pumping (OP) beam and the dispersive Faraday probing beam. Relevant to this work are the beam waists w_0 of ODT 1,2,3 and the Faraday probing beam. They are respectively 46 µm, 63 µm, 65 µm (calibrated in [95]) and 38 µm (estimated from effective area and comparison between theoretical and measured $G_1^{(1)}$ in Section 5.3.4).

The above beams not only differ by their geometries, they also operate at distinct wavelengths. We use a 1560 nm Erbium doped fiber amplifier (EDFA) for the dipole trapping beams, where ODT 2 and ODT 3 recycle the power of ODT 1[1]. The maximum optical power in ODT1 is 10 W. The remaining beams

[1] In [95] two additional EDFA are described, operating at 1560 nm and 1529 nm These sources are not used in this work and all dipole trapping beams are sourced from the same EDFA.

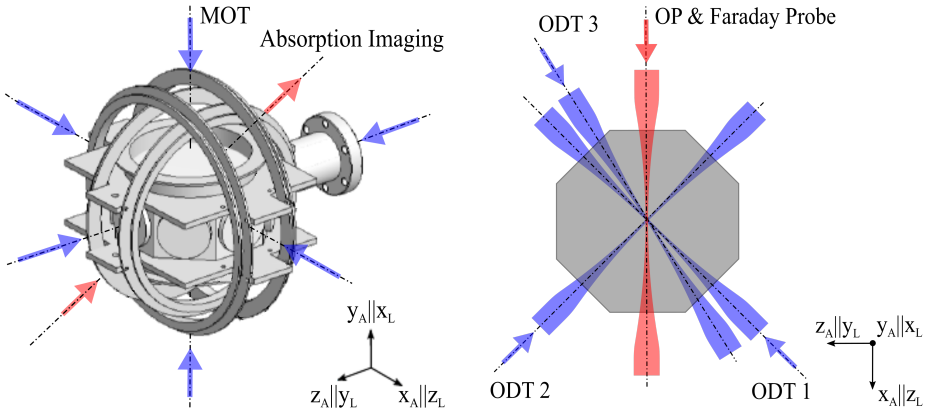

Figure 5.2.: Laser beam configurations of the experimental setup. Left and right subfigures show the collimated ($w_0 \gtrsim 5\,\mathrm{mm}$) and the focused ($w_0 \lesssim 100\,\mu\mathrm{m}$) beams, respectively. We use blue colors for cooling and trapping beams and red colors for imaging and probing beams.

operate in the NIR regime at 780 nm. As described in Section 3.1, we use two laser sources to drive the $\mathcal{D}_2$ line of ^{87}Rb, namely the cooler ($f = 2 \leftrightarrow f' = \{1, 2, 3\}$) and repumper ($f = 1 \leftrightarrow f' = \{0, 1, 2\}$) lasers. The MOT beams contain both frequencies, the absorption imaging and optical pumping use the cooler light only, and the Faraday probing alternates the cooler and repumper light to probe the spin orientation in $f = 2$ or $f = 1$, respectively. In this thesis, the cooler and repumper locking schemes have been updated to a fully digital control. This is further described in Section 5.3.3.

The experimental control of the system is based on an adapted version of the open source *Cicero Word Generator* developed at the group of W. Ketterle, MIT [97, 98]. The Cicero Word Generator is a graphical user interface (GUI) for programming hardware-clocked experimental sequences on PXI family products of National Instruments. It makes composing, testing and debugging experimental sequences easy and allows for external *hold and retrigger* for synchronizing the experiment with external trigger signals. We use this feature during experimental sequences that are sensitive to the magnetic field to synchronize their execution with the 50 Hz power lines. The fundamental limitation of the control system used in this work is its temporal resolution $\geqslant$20 µs, which is slower than the typical Larmor precession periods $\sim$ 10 µs. Spin manipulation via rf and mw pulse require much higher temporal resolution. For this purpose, a custom real time rf source was developed (see Section 5.2.4), with a temporal resolution in the range of 100 ns and capable of buffering and executing up to 1000 configuration

instructions for a dual port Direct Digital Synthesizer (DDS).

We now describe a typical experimental sequence:

(i) **3D MOT loading**. The magneto-optical trap (MOT) [99] is loaded from the ^{87}Rb background pressure in $\sim 20\,\mathrm{s}$. The cooling and repump light are provided through the optical paths indicated in Fig. 5.2 and are $-15\,\mathrm{MHz}$ red detuned to the $f = 2 \leftrightarrow f' = 3$ transition and on resonance to the $f = 1 \leftrightarrow f' = 2$ transition, respectively. The magnetic gradient field is generated by the anti-Helmholtz coils with symmetry axis along $\mathbf{y}_A$. The MOT traps about 2×10^8 atoms cooled to a temperature of $T \sim 400\,\mu\mathrm{K}$.

(ii) **Optical molasses**. The magnetic gradient of the MOT is turned off and the cooler detuning increased to $-190\,\mathrm{MHz}$ for polarization gradient cooling, a.k.a. Sisyphus cooling [100, 101]. After 20 ms this reduces the temperature bellow $T \lesssim 20\,\mu\mathrm{K}$.

(iii) **CMOT**. The gradient fields are rapidly turned on forming a compressed magneto-optical trap (CMOT) [102], which recovers the atomic density prior to the loading of the ODT.

(iv) **ODT loading**. The loading of the optical dipole trap (ODT) [103] is typically accomplished by a slow ramp up of the dipole trapping power and a successive lowering in the cooling and repump powers during the molasses and CMOT stages. In the current experimental setup, the ODT operates at 1560 nm close to the excited states transitions at 1529 nm between energy levels $5P_{3/2} \leftrightarrow \{4D_{3/2}, 4D_{5/2}\}$. As a result, the dipole trap exerts an intense light shift on the excited $f' \in \{0, 1, 2, 3\}$ [104]. This introduces a spatial dependency in the detuning of the molasses and CMOT, which strongly reduces their cooling efficiency. We palliate this effect by introducing an alternating trapping-cooling scheme (see Section 5.3.1) where the atoms experience the average trapping and cooling powers separately, i.e. without any light shift. We typically load 6×10^6 atoms into ODT 1. During loading, ODT 2 is switched off and ODT 3 is used to compress the atomic cloud, which otherwise would spread along the axial direction of ODT 1.

(v) **Optical evaporation**. The evaporation starts by lowering ODT 1 and ODT 3, while ODT 2 is ramped up. After 1s, ODT 3 is fully turned off and the atoms are pinned at the intersection of ODT 1 and ODT 2. The power of these beams is further reduced for a total evaporation time of 4.5 s, yielding a BEC of $\sim 10^5$ atoms with no visible thermal fraction.

During the evaporation phase, the spin state of the system is purified via two mechanisms. The first one is optical pumping, which transfers the atoms into the $|1, -1\rangle$ state. Optical pumping can only be applied at early

stages of the evaporation, when the recoil photon energy is negligible in comparison to the temperature of the cloud $\hbar^2k^2/2m \ll k_BT$. After optical pumping, the populations in $|1,-1\rangle$ and $|1,0\rangle$ are swapped by applying a mw pulse sequence[2]. This results in an atomic ensemble in state $|1,0\rangle$. The second purification mechanism is a combination of resonant mw pulses and magnetic field gradients that are applied during the last 2.4 s of evaporation. It removes any residual atomic populations outside $|1,0\rangle$ and is further explained in Section 5.3.2.

(vi) **Spin manipulation**. The spin state of the system is manipulated via resonant rf and mw transitions. By tuning the frequency of the driving fields we address the magnetic inter- and intrahyperfine transitions shown in Fig. 4.1. In this work, the used spin manipulations range from simple π and $\pi/2$ pulses to composite pulse sequences.

(vii) **Variable hold time**. During the hold time the SBEC undergoes coherent evolution within the ODT. Spin decoherence is strongly suppressed in single-mode SBECs and the current apparatus has reported coherence times $\tau_{\mathrm{coh}} \sim 7\,\mathrm{s}$ [33]. This is of fundamental advantage in precision measurements of external fields and other type of energy shifts with sensitivities scaling as $\propto 1/\tau_{\mathrm{coh}}$.

(viii) **Spin readout**. We use two types of spin readout. The first technique is **Stern-Gerlach imaging** [105, 106, 54] which uses absorption imaging after releasing the atomic cloud from the ODT and in the presence of a magnetic field gradient. The gradient separates the center of mass of each hyperfine manifold and maps the spin populations into separated spatial distributions. Because of the reversed gyromagnetic ratios in $f = 1$ and $f = 2$, the Zeeman sublevels of the two manifolds separate in opposite direction. Hence, Stern-Gerlach images typically show the *reversed* sum of the spin populations $N^{(1)}_{-m} + N^{(2)}_{+m}$ for $m \in \{-1, 0, +1\}$. If both $f = 1$ and $f = 2$ are populated, additional spin manipulations might be required to distinguish between each contribution[3].

[2]The pulse sequence is as follows.:

Item	Rotation	Type	Coupled levels	$\rho^{(1)}$	$\rho^{(2)}$
0				(a, b, c)	$(0, 0, 0, 0, 0)$
1	$\mathcal{R}_\pi$	mw	$\|1,0\rangle \leftrightarrow \|2,0\rangle$	$(a, 0, c)$	$(0, 0, b, 0, 0)$
2	$\mathcal{R}_\pi$	mw	$\|1,-1\rangle \leftrightarrow \|2,0\rangle$	$(a, 0, b)$	$(0, 0, c, 0, 0)$
3	$\mathcal{R}_\pi$	mw	$\|1,0\rangle \leftrightarrow \|2,0\rangle$	(a, c, b)	$(0, 0, 0, 0, 0)$

Rotations are defined in Table 4.2 and the relative populations read $\rho^{(f)}_m = |\xi^{(f)}_m|^2/N_A$.

[3]For example, in the case only $|1,0\rangle$ and $|2,0\rangle$ are populated, the atomic cloud does not

A second technique is **dispersive Faraday probing** [73, 68] which uses the vector light shift introduced in Section 3.3.3 to reveal the spin projection $F_{x_A}^{(f)}$ ($F_{z_L}^{(f)}$ in the light reference frame). Faraday probing is a non-destructive imaging technique which allows for continuous or stroboscopic probing over several Larmor precession periods. By recording the $F_{x_A}^{(f)}$ ($F_{z_L}^{(f)}$) projections at distinct points over a Larmor precession cycle, the full information of the spin projections in the transverse plane is recovered. In this work, we extended the experimental setup to support hyperfine-selective Faraday probing, which is further detailed in Section 5.3.4.

5.2. Magnetic control and manipulation

5.2.1. Magnetic control

The magnetic field control of the experiment is performed via two mechanisms. First, a rough compensation ($\sim$ 1 mG) of the Earth magnetic field and other external magnetic field sources is achieved by a pair of magnetic coils along each experimental axes. These coils are powered by stabilized current drivers and their set-points are defined by the experimental control system. Second, we use an actively controlled pair of coils along the bias field direction $\mathbf{z}_A$ ($\mathbf{y}_L$) to compensate for time-evolving magnetic fields caused by the 50 Hz cycles in the power grid and the operation of electric equipments. The remaining directions remain uncompensated, since magnetic fluctuations along these directions do not contribute to the first order correction of the magnetic field modulus:

$$\mathbf{B} = B_z\hat{\mathbf{z}} + \delta\mathbf{B} \longrightarrow B = B_z + \hat{\mathbf{z}} \cdot \delta\mathbf{B} + \mathcal{O}(\delta\mathbf{B}^2) \tag{5.1}$$

The development and testing of this scheme has been reported in [107]. The resulting magnetic noise suppression is analyzed in terms of the peak-to-peak fluctuations and averaged standard deviations over a 50 Hz power cycle. This yields $[B_{pp}]_{\text{raw}}/[B_{pp}]_{\text{feedback}} = 4.5$ and $\langle\delta B\rangle_{\text{raw}}/\langle\delta B\rangle_{\text{feedback}} = 8.6$. In the latter expression, the average is computed via $\langle\delta B\rangle \equiv \tau^{-1}\int_0^\tau \delta B(t)\,dt$, where $\tau = 20$ ms.

separate under a magnetic field gradient. In this case, we typically apply a mw π pulse that swaps the populations between the initially empty $|1,-1\rangle$ state and the $|2,0\rangle$ state. As shown in Fig. 4.1, the mw driving between $|1,-1\rangle$ and $|2,0\rangle$ has the same resonance frequency as between $|1,0\rangle$ and $|2,1\rangle$. Hence, the π pulse will fully transfer the state $|2,0\rangle \rightarrow |1,-1\rangle$ but also partially transfer the state $|1,0\rangle \rightarrow |2,-1\rangle$. After applying the π pulse, Stern-Gerlach imaging fully separates the relevant spin populations and we can assign $N_{-1}^{(1)}$ to the original population in $|2,0\rangle$ and $N_0^{(1)} + N_{-1}^{(2)}$ to the original population in $|1,0\rangle$.

5.2.2. Rf manipulation

Rf manipulations couple spin states belonging to the same hyperfine manifold with an energy splitting governed by the LZS (see Fig. 4.1). They require magnetic driving fields that are transverse to the external bias field (along $\mathbf{z}_A$). To this end, we make use of the already existing transverse offset coils along $\mathbf{x}_A$ and incorporate a double bias-T configuration to combine the DC and AC driving for the bias control and spin manipulations, respectively. We incorporate a 25 dB amplifier (*Minicircuits*, ZHL-6A+) for the rf driving signal. The schematic of the driving circuit is given in Fig. 5.3, where the DC driving is further described in [95] and the rf driver is detailed later in this chapter.

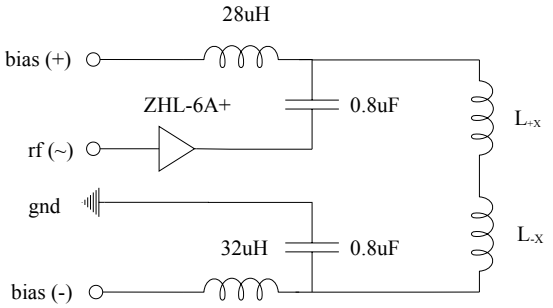

Figure 5.3.: Double bias-T configuration for combining the bias and rf driving. The pair of magnetic coils along $\mathbf{x}_A$ are labeled as $\mathrm{L}_{\pm x}$.

The resulting rf driving field is linearly polarized and the total magnetic field reads

$$\mathbf{B} = \left(\tilde{B}_x \cos(\omega t + \phi_x), 0, B_z\right)^T \ , \tag{5.2}$$

where B_z is the magnetic bias field, $\tilde{B}_x$ the rf field amplitude, ω its angular frequency and ϕ_x the initial phase. The linear polarized rf field has projections onto σ^+ and σ^- components (see Eq. (4.2b)) and is therefore suited to simultaneously manipulate the Zeeman sublevels in $f = 1$ and $f = 2$. Expressing the driving field in Eq. (5.2) in terms of the coherent spin manipulation parameters described in Chapter 4 yields

$$\omega_0^{(1)} = \gamma^{(1)} B_z \qquad \omega_0^{(2)} = \gamma^{(2)} B_z \tag{5.3a}$$

$$\Delta_-^{(1)} = -\omega - \omega_0^{(1)} \qquad \Delta_+^{(2)} = \omega - \omega_0^{(2)} \tag{5.3b}$$

$$\Omega_{0,-}^{(1)} = -\gamma^{(1)} \tilde{B}_x/2 \qquad \Omega_{0,+}^{(2)} = \gamma^{(2)} \tilde{B}_x/2 \tag{5.3c}$$

$$\phi_- = \phi_x + \pi \qquad \phi_+ = \phi_x \tag{5.3d}$$

The gyromagnetic ratio $\gamma^{(f)}$ is defined in Eq. (2.12) and is negative (positive) for $f = 1$ ($f = 2$). We have chosen to use positive defined $\Omega^{(f)}_{0,\pm}$ for both manifolds and account for the negative gyromagnetic ration in $f = 1$ with a π phase shift in $\phi^{(1)}$.

The rf amplitude, frequency and phase are fundamental experimental parameters to be characterized or adjusted for coherent spin manipulations. Similarly, the duration of the rf field has to be tuned depending on the required rotation angle. In the following, we illustrate this process for $f = 1$:

- **Amplitude.** In general, strong driving amplitudes and short pulse durations are preferable because of the resulting *power broadening* and enhanced robustness against magnetic field fluctuations. However, we limit the value of $\tilde{B}_x$ based on the following considerations. First, it has to be small enough such that we operate in the perturbative regime $|\tilde{B}_x/B_z| \ll 1$ (i.e. $|\Omega^{(1)}_-/\omega^{(1)}_0| \ll 1$). Second, we shall not overcome the saturation power of the rf amplifier, which is key for a linear amplification. While the first condition is magnetic field dependent, the second is guaranteed even at the maximum amplitude of the rf source, where we have proven a linear amplification scaling[4].

- **Frequency.** Resonant spin-1 manipulations require $\Delta^{(1)}_- = -\omega + \omega^{(1)}_0 = 0$, where $\omega^{(1)}_0 = \gamma^{(1)} B_z$ is stabilized by the earlier described active magnetic field control. Although $\omega^{(1)}_0$ is stabilized, its actual value has to be measured using the atomic ensemble. To this end, we typically prepare the spin along $|1,-1\rangle$ and apply a 65 µs long rf-pulse and measure $F^{(1)}_z/N_A$ for different driving frequencies ω. Results are shown in Fig. 5.4 (i), where we use Eq. (4.9) for fitting the experimental data. The free parameters are the resonance frequency $\omega^{(1)}_0$ and the resonant Rabi frequency $\Omega^{(1)}_{0,-}$.

- **Phase offset**. The phase offset of the rf driving field is given by the initial phase of the rf driver as well as additional constant phase shifts introduced by the propagation delay of the rf lines, amplifiers and the inductance of the rf coils. Since for most application only the relative phase between consecutive rf pulses is relevant, these constant phase shifts are not explicitly calibrated.

[4] To prove the linearity at a given nominal driving amplitude $\tilde{B}_x$, we reduce the driving to one half $\tilde{B}_x \to \tilde{B}_x/2$ and verify that $\Omega^{(1)}_- \to \Omega^{(1)}_-/2$

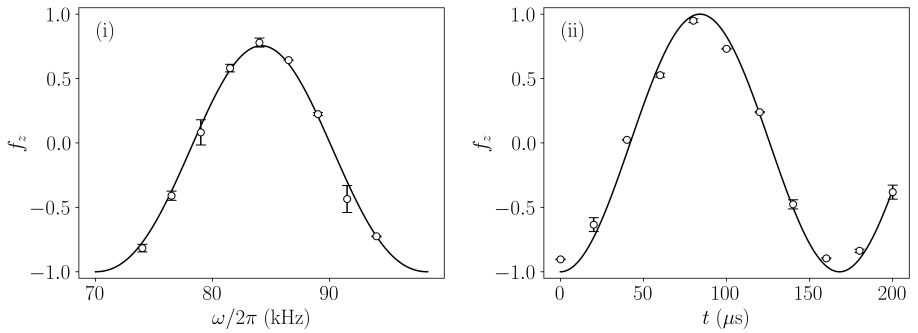

Subfigure	Fit parameter	Best estimate
(i)	$\omega_0^{(1)}/2\pi$	$-84.18(12)$ kHz
(i)	$\Omega_{0,-}^{(1)}/2\pi$	$5.93(11)$ kHz
(ii)	$\Omega_{0,-}^{(1)}/2\pi$	$5.952(31)$ kHz

Figure 5.4.: Rf driving field calibration for $f = 1$. Subfigure (i) evaluates the population inversion vs. driving field frequency for a 65 µs long rf pulse. The measured resonance frequency corresponds to an offset field $B = \omega_0^{(1)}/\gamma^{(1)} = 119.97(17)$ mG. Subfigure (ii) shows Rabi oscillations for a resonant driving field $\omega = -\omega_0^{(1)}$. Open circles and error bars represent the experimental data and standard deviation, respectively. Curves show the fitted results based on Eq. (4.9), where the free fit parameters and their best estimates are summarized in the table above. Used spin imaging technique: *Stern-Gerlach*.

- **Duration**. The rf field amplitude $\tilde{B}_x$, or equivalently $\Omega_{0,-}^{(1)}$ in Eq. (5.3c), and its duration t determine the net rotation angle $\Omega_{0,-}^{(1)}t$. Thus, by performing an accurate measurement of $\Omega_{0,-}^{(1)}$, the required t can be inferred for any arbitrary rotation angle. In Fig. 5.4 (ii) we show a Rabi oscillation sequence, where starting from $|1-1\rangle$, we apply a resonant rf rotation for various durations t. We fit the resulting dynamics to Eq. (4.9), with $\Delta_-^{(f)} = 0$ and $\Omega_{0,-}^{(1)}$ as a free fit parameter. Note, that this sequence is particularly suited for evaluating the resonant Rabi frequency, and that the best estimate for $\Omega_{0,-}^{(1)}$ is about 3 times more accurate in Fig. 5.4 (ii) than in Fig. 5.4 (i).

An analogous calibration can be performed to find $\omega_0^{(2)}$ and $\Omega_+^{(2)}$, but in practice is rarely necessary because $\gamma^{(2)} \approx -\gamma^{(1)}$. For example, with $\Delta_-^{(1)} = 0$, i.e. on res-

onance with the $f = 1$ resonance, the residual $f = 2$ detuning is $\Delta_+^{(2)}/\Omega_+^{(2)} \approx 0.1$. This is negligible for most rf manipulations of this work[5], which simultaneously rotate $f = 1$ and $f = 2$ in reversed directions.

In order to individually address the $f = 1$ or $f = 2$ manifold, and additional driving field along $\mathbf{y}_A$ should be included. Amplitude and frequency have to match the already existing driving along $\mathbf{x}_A$ and the phase difference between them $\Delta\phi = \phi_y - \phi_x$ can be used to commute between a coupling to $f = 1$ or $f = 2$. For a phase difference $\Delta\phi = -\pi/2$, the resulting magnetic field is σ^- polarized and only drives $f = 1$. In contrast, for $\Delta\phi = +\pi/2$ we obtain a σ^+ polarized magnetic field, which exclusively drives $f = 2$.

5.2.3. Mw manipulation

The microwave manipulation is used to couple spin states belonging to different hyperfine manifolds. In Fig. 4.1 and discussion below we saw that the distinct pseudo $f = \frac{1}{2}$ transitions have generally different resonance frequency but also different resonant polarization components. While the driving field frequency is easy to adjust by means of configuring a waveform synthesizer, its polarization is more involved as it depends on the particular positioning of the mw antenna with respect to the magnetic offset fields.

In this work, rather than producing a mw field for a particular polarization component, we configure the mw antenna to result in a driving field that simultaneously has σ^+, σ^- and π polarization components. In particular, we use a horn antenna along the $(1, -1, -1)_A^T$ direction and feed it with a custom built microwave chain, shown in Fig. 5.5. The latter is based on a two stage mixing scheme, which combines a custom rf input ($\sim 24\,\mathrm{MHz}$) and two stable frequency sources at 210 MHz and 6.6 GHz, respectively. The rf source is equivalent to the rf driver used in Section 5.2.3, which will be described later. The fixed frequency references are a digital synthesizer (*National Instruments*, PXIe-5650) and a voltage controlled oscillator (VCO) stabilized by a phase-locked loop (PLL). The reference for the PLL is an externally provided 25 MHz clock. This design offers an additional on/off trigger port that controls the state of an rf switch (*Minicircuits*, ZX80-DR30-S+) prior to the input of the last mixing stage. The trigger port is used to gate the mixed $\sim 24\,\mathrm{MHz}$ and 210 MHz signals, such that for generating a mw pulse, the amplitude of the rf driver is held constant and the trigger port is enabled for the required pulse duration. At the end of the microwave chain, the spectrum is cleaned by means of a cavity filter. This reduces the power in unwanted sidebands resulting from the two mixing stages and ensures

[5] The only exception is the hyperfine-dependent state preparation Appendix E, which is a composite pulse sequence that explicitly uses the relative detuning between $f = 1$ and $f = 2$ rf manipulations.

that subsequent amplifications are fully devoted to the resonant sideband. The filtered signal is further amplified to a power of $\sim 30\,\mathrm{dBm}$ and sent to the horn antenna. Note that a circulator is inserted to protect the high power amplifier (*Minicircuits*, ZVE-3W-83+) from back reflections and impedance mismatches at the antenna.

Similar to rf manipulations, we can adjust the following parameters of the mw driving:

- **Amplitude**. The amplitude is adjusted by means of the rf-driver, which is running at 1/4 of its full scale amplitude to ensure a linear amplification across all amplifiers of the microwave chain.
- **Frequency**. The driving field has to match the particular resonance fre-

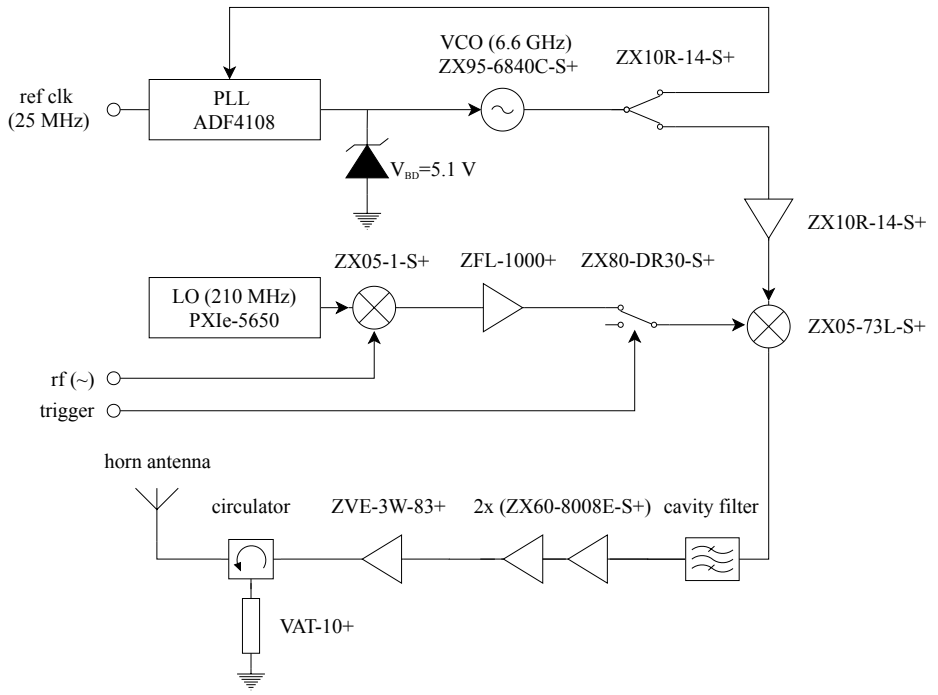

Figure 5.5.: Microwave chain used to generate the resonant 6834 MHz interhyperfine driving field. We show the *Analog Devices* and *National Instruments* part numbers for the phase-locked loop (PLL) and local oscillator (LO), respectively. The remaining part numbers belong to the *Minicircuits* catalogue.

quency $\omega^{(12)}_{0,mm'}$ between levels $|1,m\rangle \leftrightarrow |2,m'\rangle$. An example of this calibration is given in Fig. 5.6 (i), where we we scan the population inversion between $|1,-1\rangle \leftrightarrow |2,-2\rangle$ as a function of the driving frequency. The pulse duration is set to 90 µs.

- **Phase**. The 210 MHz and 6.6 GHz run continuously and their phase is not reset at start of the experimental sequence. Therefore, we only have control on the relative phase between successive mw pulse within the same experimental sequence.

- **Duration**. We control the duration of the mw pulses through the pulse length of the gating (trigger) pulse. In Fig. 5.6 (ii) we scan the duration of a resonant $|1,-1\rangle \leftrightarrow |2,-2\rangle$ driving and observe the expected Rabi oscillations. The system is initially prepared in $|1,-1\rangle$ and the resonance

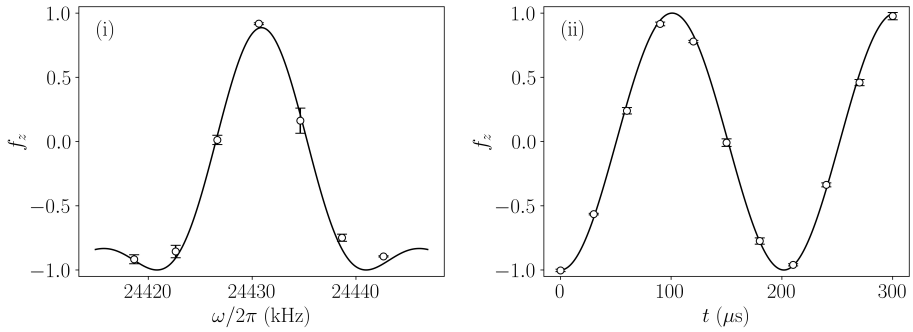

Subfigure	Fit parameter	Best estimate
(i)	$\omega^{(12)}_{0,-1-2}/2\pi$	24 430.90(10) kHz + 210 MHz + 6.6 GHz
(i)	$\Omega^{(12)}_{0,-1-2}/2\pi$	4.70(16) kHz
(ii)	$\Omega^{(12)}_{0,-1-2}/2\pi$	4.955(12) kHz

Figure 5.6.: Mw driving field calibration for the pseudo-spin $f = \frac{1}{2}$ transition between sates $|1,-1\rangle \leftrightarrow |2,-2\rangle$. Subfigure (i) evaluates the population inversion vs. driving field frequency for a 90 µs long rf pulse and a magnetic field of $B = 120$ mG. Subfigure (ii) shows Rabi oscillations for a resonant driving field $\omega = \omega^{(12)}_{0,-1-2}$. Open circles and error bars represent the experimental data and standard deviation, respectively. Curves show the fitted results based on Eq. (4.9). The free fit parameters and their best estimates are summarized in the table above. Used spin imaging technique: *Stern-Gerlach*.

Attribute	Value | Comment	Unit
Operational modes[1]	Single tone, Modulation, Sweep	
Number of channels[1]	2	
Amplitude resolution[1]	10	bit
Frequency resolution[1]	32	bit
Phase resolution[1]	14	bit
DAC sampling rate[1]	500	MS/s
Max. instructions	1000	
Trigger input resolution[2]	100	ns
Configurable delay[2]	62.5 | Step size	ns
	125 | Min. delay	ns
Reconfiguration time[2]	100 | Update profile pins	ns
	4 | Update SPI register	us

[1] Reference values taken from the AD9958 data sheet [108].
[2] Typical values observed during development and testing.

Table 5.1.: General features and timing specification of the real-time rf source.

frequency is taken from the fit results of Fig. 5.6 (i). As we saw in Section 5.2.2, this sequence is particularly suited for estimating the resonant Rabi frequency $\Omega^{(12)}_{0,-1-2}$ and its best estimate is above an order of magnitude more precise in Fig. 5.6 (ii) than in Fig. 5.6 (i).

5.2.4. Real-time rf source

The real-time rf source became a key development for this thesis. It is used to generate the rf and gaiting (trigger) signals for rf and mw spin manipulations. This extends the main experimental control system, which with a minimum temporal resolution of 20 µs is not suited for rf synthesis. We summarize the main capabilities of the device in Table 5.1.

The operation of the real-time rf source can be understood in terms of 3 effective layers:

(i) **AD9958**. This is a dual channel Direct Digital Synthesizer (DDS) from *Analog Devices* [108]. This is the lowermost layer, devoted to the generation of rf signals. At the core of the DDS sit two phase accumulators and two phase-to-amplitude converters, which generate the corresponding sine/cosine digital waveforms for each channel. The digital waveforms are fed into fast digital-to-analog converters (DACs) that synthesize the actual rf signals.

There are three fundamental reason why this DDS has been chosen. First, because its high clocking speed and sample rate (500 MS/s) is far above the frequencies required for rf and mw manipulations, which respectively are 84 kHz and 24 MHz (rf input of the mw chain). Having a high ratio between sampling rate and target rf frequencies minimizes the distortion due to the discrete synthesis of the sine/cosine waveforms. Second, the internal phase accumulator is continuously running and is independent of the amplitude settings. This ensures phase coherence in a multi-pulse rf sequence. Third, because of its fast programming interfaces: SPI for register setting and 4 profile pins for the up to 16-level direct modulation.

(ii) **ChipKit Max 32**. The intermediate layer is a PIC32 microcontroller from *Digilent* [109], which operates as a sequencer, responsible for the hardware-timed configuration of the AD9958 through SPI and the 4 profile pins. It features an input trigger, used to synchronize its operation with the experimental control system, as well as an output trigger, which we use for monitoring purposes or for gating the mw chain. The C++ source code is available on [110].

During operation, the microcontroller parses incoming serial commands and populates the built-in *function stack* and *variable stack*. They are a 1000 item-long array of function pointers and a 1000×5 parameter array, respectively. The functions include SPI register transfers, profile pin settings, configurable delays and input/output trigger management. The parameters are the particular arguments for each of these function calls. Once the function and variable stack have been configured, the system is ready for execution. During execution, the microcontroller mutes all interrupts and sequentially steps through the function and variable stacks. At completion, interrupts are enabled and the system is ready again to parse incoming commands and to build new function and variable stacks.

(iii) **Python API**. This is the uppermost layer, which exposes to the user the tools for sequentially configuring the rf source. It implements user friendly methods such as *setAmplitude()*, *waitForTimer()*, *waitForTriggerIn()*, *setTriggerOut()*... where the corresponding hardware settings are handled in the back end. This is, for each API method the required SPI transfers, profile pin settings or trigger managements are automatically inferred. These are then transferred as serial commands to the microcontroller, which constructs the function and variable stacks. After the rf sequence has been programmed, the user calls the API method *runStack()*, which notifies the microcontroller that the configuration has been finished and commands it to initiate the execution of the function and variable stacks. Please refer to [110] for the API source code, its documentation and working examples.

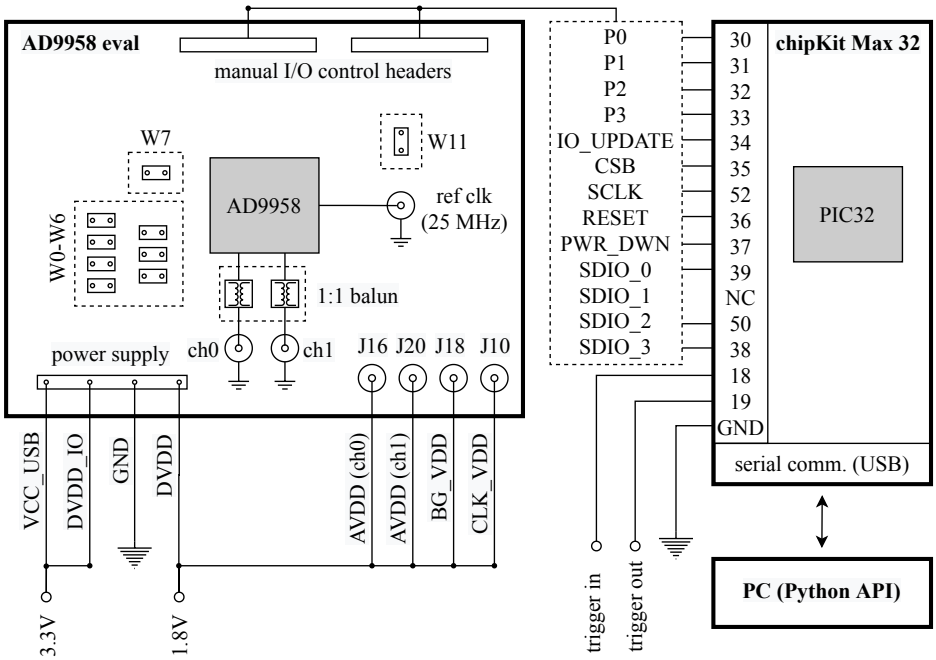

Figure 5.7.: Connection between the DDS (AD9958 eval), the controller (chipKit Max 32) and the Python API (running on the host PC). Please refer to [111] for setting jumpers W0-W7 and W11, which configure the AD9958 control mode and reference clock, respectively. The suitable decoupling baluns are described in the text below. We label the chipKit Max 32 ports via the corresponding board pins (30, 31, 32...). For the complete pinout please see [109]. Note that the microcontroller operates at 3.3 V and that typical 5 V TTL triggering signals have to be adapted.

In Appendix B we show a subset of these examples and the corresponding waveform captures to illustrate the operational modes of the AD9958.

The schematic and wiring between the 3 parts of the real-time rf source is shown in Fig. 5.7. We use the AD9958 Evaluation Board [111], which can be operated in two ways. On one hand, using the on-board USB controller (not shown in Fig. 5.7) and a ready-to-use GUI running on the host PC. This operational mode is intended for evaluating the main capabilities of the DDS but is not adequate for real-time control. On the other hand, the DDS can be controlled through the I/O

pin headers, which expose the SPI interface and profile pins of the device. This is suited for real-time control applications but requires a custom controller and a suitable user interface. We use this second operational mode, where the controller and user interface are the chipKit Max 32 and the Python API, respectively. To this end, jumpers W0-W7 have to be configured as described in [111] and jumper W11 is set to accept the external 25 MHz reference clock. A pair of 1:1 baluns is used to decouple the AD9958 outputs and reference the rf signals to the provided ground level. The board is shipped with two surface mounted baluns (ADTT1-1, *Minicircuits*), with a typical frequency range of 0.3 MHz to 300 MHz. They are only adequate for decoupling the rf signals of the mw chain ($\sim$ 24 MHz). For rf manipulations ($\sim$ 84 kHz) we use instead two ADT1-6T+ baluns from *Minicircuits*, with a frequency range of 0.03 MHz to 125 MHz.

5.3. Optical manipulation and probing

In the context of this thesis the optical manipulation and probing have been upgraded in several forms. We describe these with different levels of detail in function of their importance to the thesis. That is, for the pulsed ODT loading scheme and the new spin state purification method, we will focus on presenting their key concepts, such that future PhD generations can operate and further improve the techniques. On the other hand, the digital laser locking scheme and the hyperfine selective Faraday probing are key contributions of this work, for which detailed descriptions will be provided.

5.3.1. Pulsed ODT loading scheme

The intense 1560 nm ODT beams provide the confinement potential for the $f \in \{1, 2\}$ ground state manifolds ($5^2S_{1/2}$). Earlier in this chapter, we introduced the ODT geometry and their maximum power. Based on these parameters and Eq. (3.17a) we can estimate the typical trap depth for the ground state manifold $V_0^{(f)} \approx k_B \times 70\,\mu\text{K} = h \times 1.5\,\text{MHz}$. The situation is different for the excited state manifolds $f' \in \{0, 1, 2, 3\}$ ($5^2P_{3/2}$), which additionally experience a strong light shift arising from the excited state transition between $5^2P_{3/2} \leftrightarrow 4D_{3/2}$. The excited state transition has a resonant wavelength of 1529 nm and is much closer to the ODT wavelength than is the $\mathcal{D}_2$ line. The corresponding excited states energy shift is above $\gtrsim h \times 100\,\text{MHz}$. This effect has been used for trap tomography [96] and has triggered the development of a Floquet theory that accurately describes excited states light shifts [104].

The strong excited state light shifts have a significant impact in resonant and near-resonant optical manipulations. Most notably, it influences the loading of the ODT, where the cooling and intense trapping light beams coexist. At this

point, the ODT provides a conservative trapping potential and cooling is required to accommodate the atoms at the center of the ODT. However, the detuning of the cooling light is spatially dependent due to the strong excited state light shift and this results in heating and inefficient atom loading [95]. We palliate this effect by introducing a pulsed ODT loading scheme, where cooling and trapping lights are rapidly alternated. In this case, the atoms alternately experience cooling (without light shifts) and trapping. The atomic motion averages over these two effects to produce a damped motion in the average dipole potential. In the following we describe the development of a pulse-width modulation (PWM) scheme for the controls, i.e. binary gating switches, of the cooling and trapping beams.

Two PWM implementations have been tested on a low cost Arduino Nano (*Arduino Srl*) development board (source codes available in [112]). The first one uses native (hardware) PWM counters for separate control of the cooling and trapping light. It features a 8 bit resolution for the duty cycle and counter offset but the frequency is only roughly adjustable to $16\,\mathrm{MHz}/(256 \times N)$, where $N \in$

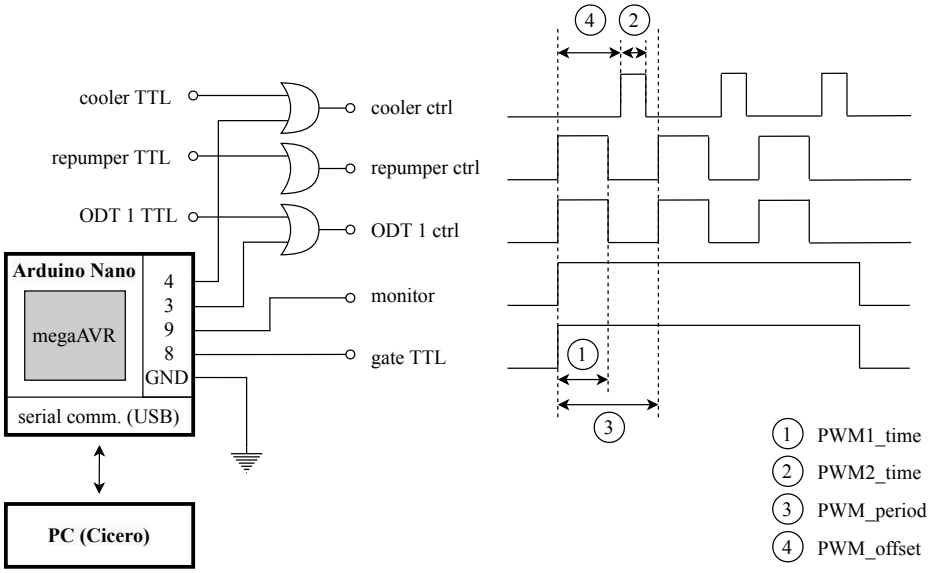

Figure 5.8.: Left: hardware connections between the Arduino Nano and the TTL control signals for cooling (cooler TTL and repumper TTL) and trapping (ODT 1 TTL). The microcontroller operates at 5 V and is fully compatible with standard TTL logic. Right: typical PWM waveforms. The parameters ①, ②, ③ and ④ are configured through the serial interface.

$\{1, 8, 64, 256, 1024\}$. The second implementation is based on a software PWM, which typically operates with a lower phase and offset resolution but has a more adjustable frequency. We have chosen this second method and show in Fig. 5.8 (left) the corresponding hardware connections. We use the gate TTL input to enable the synthesis of the PWM signals and verify the operation of the device through the monitor output. The synthesized PWM signals are combined via OR gates with the TTL signals for regular control of the cooling and trapping beams. These are the cooler TTL, repumper TTL and ODT 1 TTL signals. Note that PWM of ODT 2 and ODT 3 are produced simultaneously with ODT1, since these beams recycle the power of ODT 1. In Fig. 5.8 (right) we show the configurable parameters of the PWM scheme. They define the duty cycle, relative offset and overall frequency of the two PWM outputs. These parameters are configured within the Cicero Word Generator and are forwarded to the microcontroller via serial communication (USB).

The current configuration enables the cooling beams when the trapping and repumping beams are disabled (and vice-versa) such that only repumping events are affected by the strong excited state light shift. As a result, repumping is strongly suppressed at the central region of the ODT, where cold atoms are eventually collected in the $f = 1$ state (dark state for the cooling process).

5.3.2. Spin state purification

The efficiency of cooling a spin ensemble down to a SBEC strongly depends on the particular spin state. Condensation is most easily achieved when only a single spin state is populated. This is because of the following three reasons. First, the phase space density and condensation temperature T_c drop when atoms are distributed among different spin states. In the most extreme case, where the atoms are in an incoherent mixture that equally populates all spin-f Zeeman sublevels, T_c drops by a factor $(2f + 1)^{2/3}$ [25]. Second, spin changing collision during evaporation depletes the atomic populations from partially condensed spin states to others where the thermal gas is not yet saturated [113]. Third, the thermalization time diverges near the phase transition and the condensation occurs within local spin domains. The latter effect is most relevant to atomic ensembles populating multiple Zeeman sublevels and which can accommodate distinct spin domains [114, 115].

In this work, we have implemented a new spin purification scheme that combines, optical trapping, magnetic field gradient pulses and gravity. The spin state we target is the polar $f = 1$ state $|1, 0\rangle$ (or equivalently $\xi = (0, 1, 0)^T \oplus \mathbf{0}_5^T$). As described in Section 5.1, right after the start of the optical evaporation, optical pumping and mw manipulations are used to transfer close to 90% of the atomic population into $|1, 0\rangle$. The total evaporation time is 4.5 s and during the last 2.4 s

we additionally apply a spin purification scheme to remove the residual atoms in $|1,1\rangle$ and $|1,-1\rangle$. It is formed by 12 repetitions of the following 200 ms long sequence:

(i) 0.0 ms to 4.9 ms. The magnetic field offset is set to point along $\mathbf{z}_A$ and allowed to stabilize around $B = 120\,\mathrm{mG}$. Magnetic field gradients are switched off during this stage.

(ii) 4.9 ms to 5.0 ms. We apply a resonant mw π pulse, that transfers the population in $|1,-1\rangle$ into $|2,-1\rangle$. This leaves the $|1,0\rangle$ population unaffected and locates any residual population in high field seeking states.

(iii) 5.0 ms to 200.0 ms. The magnetic field offset is set to point along $-\mathbf{y}_A$ (along gravity) and ramped up in magnitude to $B \approx 500\,\mathrm{mG}$. The high magnetic field drives the atomic system far into the polar region of its phase diagram [24], where the energy offset introduced by the QZS is much higher than the ferromagnetic interaction. In this regime $|1,0\rangle$ is the groundstate and spin changing collisions are highly suppressed. During this time step we operate the MOT coils driver at full current ($\sim 20\,\mathrm{A}$) to provide a gradient field above $25\,\mathrm{Gcm}^{-1}$ along gravity. As a result, high field seeking states ($|1,+1\rangle$, $|2,-1\rangle$, $|2,-2\rangle$) experience an enhanced gravitational drag and are forced to leave the optical trap.

The combination of the optical evaporation with the above described spin purification results in a pure SBEC in $|1,0\rangle$ with neither visible thermal fraction nor residual spin populations in the $|1,\pm1\rangle$ states.

5.3.3. Digital PLL laser lock

The current experimental setup builds upon a single spectroscopic element. That is, all light sources are referenced to a master 1560 nm EDFA laser. The light source is frequency doubled to 780 nm and features a linewidth as narrow as 4.75(6) kHz [95]. The 780 nm light is sent through a modulation transfer spectroscopy (MTS) setup [116] operating on the $f = 2 \leftrightarrow f' = 3$ cycling transition of the ^{87}Rb $\mathcal{D}_2$ line. The MTS outputs a dispersive error signal that is fed back to the EDFA current controller for frequency stabilization. We note that the MTS stabilization technique is particularly robust against power fluctuations [117] and that the system can be operated for several days without losing lock. The accuracy and robustness of the master laser is leveraged by the remaining light sources of the experiment. These are the ODT (1560 nm), which is seeded by the master laser; and the cooler and repumper lasers (780 nm), which are stabilized to the frequency doubled master light through a phase-locked loop (PLL). In this

section we will discuss the latter two locking schemes, focusing on the developed digital control of the PLL units.

The cooler and repumper are *Toptica* TApro and DLpro external cavity diode lasers (ECDL). They feature external controls for the diode current and for the voltage of the piezoelectric element attached to the internal diffraction grating. We provide feedback on both controls as their bandwidth and tuning range are inherently different. The current control has a typical bandwidth of 20 MHz and is primarily used to stabilise the laser frequency against rapid perturbations. The piezo control is significantly slower and has a bandwidth of $\lesssim 1\,\mathrm{kHz}$. Although slow, the piezo has a large range, covering the whole mode-hop-free tuning range $\sim 2\,\mathrm{GHz}$. Once the laser is locked, the feedback is predominantly provided by the current controller and the piezo control is an idle state unless the required feedback signal is outside the tuning range of the current controller. This happens at several points of our experimental sequence that require a sudden change in the absolute laser frequency set point above $|\Delta f| \gtrsim 200\,\mathrm{MHz}$. In these situations, the piezo driver *slowly* moves the laser frequency until the set point is again within the tuning range of the current controller and the laser lock is recovered.

The PLL offset locks are shown in Fig. 5.9. The cooler and repumper lasers are combined with light from the stabilized and frequency doubled master laser. Their beat note is captured by a commercial telecommunications PIN preamp receivers (PT10GC 10Gb/s, *Bookham*). The beat note frequency is, depending on the experimental sequence, within $f_{\mathrm{BN}}^{\mathrm{cooler}} \in [-200\,\mathrm{MHz}, 600\,\mathrm{MHz}]$ for the cooler laser and between $f_{\mathrm{BN}}^{\mathrm{repumper}} \in [6.0\,\mathrm{GHz}, 7.0\,\mathrm{GHz}]$ for the repumper laser.[6] The beat notes are fed into two digital PLLs (ADF4110 and ADF41020 from *Analog Devices*) that use internal counter and scaling logic to compare the signals against the provided reference clock (10 MHz and 100 MHz). The set-point for the beat note frequency is controlled by configuring the counter and scaling logic within the PLLs. If the beat note frequency exceeds the set-point, the charge pump (*cp*) outputs a positive current and vice-versa if the beat note is below the set point.[7] The charge pump is connected to a resistor ladder that converts the output current to a voltage level. Note that the the resistor ladder is referenced to the charge pump source voltage (*vp*) and ground (*gnd*), and that the generated voltage levels will be centred around *vp*/2. We compensate this through a separate offset control for the cooler and repumper laser locks. At their output we obtain the error signal for each lock, which for small deviations is proportional to the difference between set-point and actual laser frequency. The error signal is sent through two cascaded integration stages. The output of the first integration

[6] We define the beat note frequencies such that for most of the experimental sequence they are positively defined. This is $f_{\mathrm{BN}}^{\mathrm{cooler}} \equiv f^{\mathrm{master}} - f^{\mathrm{cooler}}$ and $f_{\mathrm{BN}}^{\mathrm{repumper}} \equiv f^{\mathrm{repumper}} - f^{\mathrm{master}}$

[7] The ADF4110 and ADF41020 chipsets have configurable charge pump polarities. Hence, the described frequency response can be inverted.

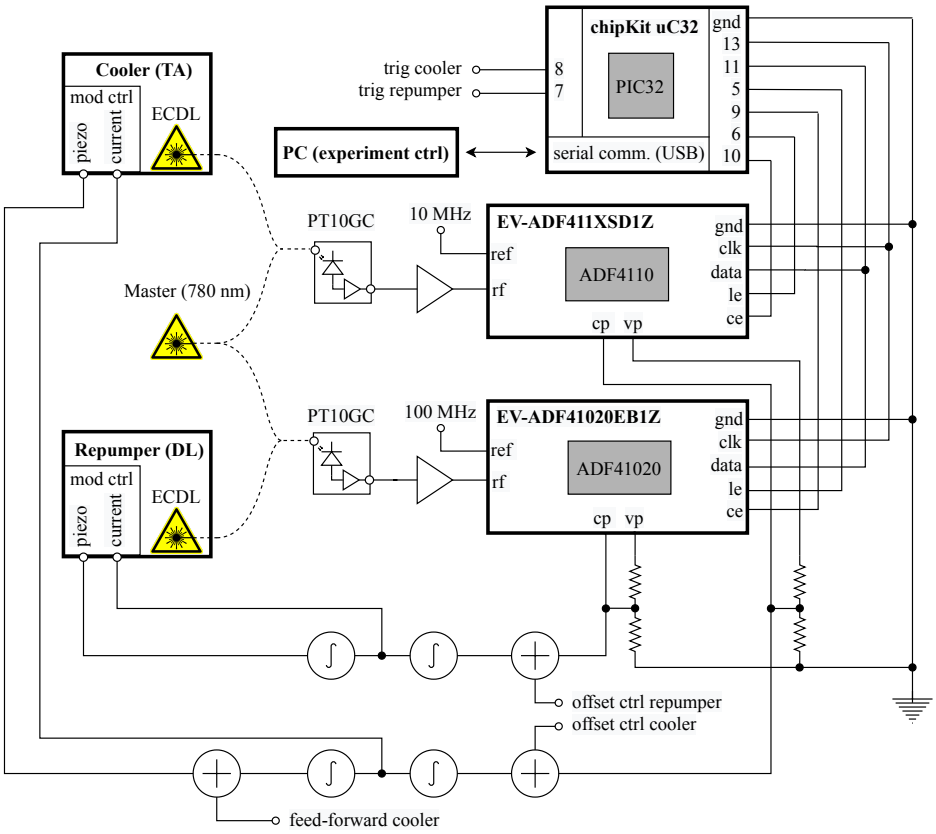

Figure 5.9.: Schematic of the digital PLL laser lock for the cooler and repumper lasers. Both laser are interferred with the frequency doubled master laser and the corresponding beat notes are forwarded to the digital PLLs (*ADF4110* and *ADF41020*). The PLLs are configured in real-time by the *chipKit uC32* microcontroller and return a current on the charge pump (*cp*) which for small deviations is linear in the difference between frequency set-point and the beat note frequency. The *cp* output is connected to a resistor ladder and an offset correction. The feedback electronics is based on a single (double) integrator connected connected to the current (piezo) drivers of the ECDL lasers. We use straight and dashed lines for electrical wires and optical fibres, respectively.

stage is the feedback signal for the laser current, while the second one has a much slower response and is suited for providing feedback to the piezo driver. In order to reduce the response time of the cooler lock, we introduce a feed-forward signal that is added to the output of the second integrator.

A special feature of this locking scheme is that no analogue set-point is provided. Instead, the set-point is tuned by configuring the PLL registers in real-time. To this end, the PPLs are connected to a chipKit uC32 microcontroller (*Digilent*) which includes two first-in-first-out (FIFO) buffer that at the beginning of each experimental sequence are programmed to hold the required cooler and repumper frequency set-points. During the execution of the experimental sequence, the FIFOs are sequentially emptied and the PLLs are reconfigured. The reconfigurations are externally triggered and use the SPI interfaces of the ADF4110 and ADF41020. Both devices share the same clock and data lines but use separate latch-enable (le) and chip-enable (ce) lines.

In the following we list the advantages of the described digital laser locking scheme with respect to the pre-existing setup, which was based on a static PLL configuration and used voltage-controlled oscillators (VCOs) as reference inputs [95].

- **Stability**. The stability of the frequency set-point is inherited from the PLL reference (ref). In the current design we ensure a stable reference by using constant frequency oscillators at 10 MHz and 100 MHz, for the cooler and repumper PLLs, respectively. This was not the case in the previous design, which used free-running VCOs as reference clocks. VCOs typically feature temperature dependent and ageing drifts, and require a frequent recalibration of their voltage-to-frequency response.

- **Configurable lock polarity**. This is a unique property of this locking scheme that enables to operate the lock on positive as well as negative beat note frequencies. The gain of the feedback reverses its sign when moving form positive to negative beat note frequencies. As a result, the previous lock design was adjusted to stabilize (i.e. have negative feedback) at either positive or negative beat note frequencies. This is different in the current design, where the frequency set point and PLL polarity can be adjusted real-time. This is used in the dispersive Faraday probing of $f = 2$, which operates the AD4110 PLL at a set-point of $f_{\mathrm{BN}}^{\mathrm{cooler}} = -200\,\mathrm{MHz}$, while the rest of the experimental sequence operates it above $f_{\mathrm{BN}}^{\mathrm{cooler}} \gtrsim 160\,\mathrm{MHz}$.

The source code for the digital PLL laser lock can be found in [118], which includes custom libraries for the ADF4110 and ADF41020, as well as a lightweight SPI library. Please refer to Appendix C for a Pyhton code example that illustrates the configuration and execution of the digital PLL locks.

5.3.4. Hyperfine-selective Faraday probing

The extension of the already existing Faraday probe [95] to $f = 1$ and $f = 2$ made it possible to simultaneously track the transverse magnetisation in both hyperfine manifolds. It is the cornerstone of the comagnetometery and interhyperfine interaction studies in Chapter 6 and Chapter 7.

This section is arranged as follows. It first adapts the dynamical evolution presented in Section 3.5 to input and output relations of the light polarization Stokes parameters. Thereafter, the experimental arrangement is presented and the Stokes parameters are put into context with the obtained readout signals. The translation from readout signals (i.e. voltage levels) to Stokes parameters require adequate signal post-processing and a calibration of the gain of the photodetection electronics, which are both discussed.[8] The last part is devoted to the calibration of the vector light-atom coupling constant $G_1^{(f)}$.

Discrete Stokes parameters and transfer relations

In Section 3.3.3 we discussed the vector light-atom interaction, which introduces a circular birefringence dependent to the atomic spin projection along the light propagation axis. This interaction results in a rotation ϕ of the light polarization which can be detected via a calibrated polarimeter. In this work, the Faraday rotation is a weak perturbation $|\phi| \lesssim 30\,\mathrm{mrad}$ and the light-atom interaction is described by a set of input (before the light-atom interaction) and a set of output (after the light-atom interaction) mean-field Stokes parameters. We write them as S_i^{in} and S_i^{out}, with $i \in \{x, y, z, 0\}$. For the input Stokes parameters we assume a light field that is linearly polarized along the horizontal direction $(\mathbf{y}_L || \mathbf{z}_A)$, such that:

$$S_x^{\mathrm{in}} = N_L/2\,, \tag{5.4a}$$
$$S_y^{\mathrm{in}} = 0\,, \tag{5.4b}$$
$$S_z^{\mathrm{in}} = 0\,, \tag{5.4c}$$
$$S_0^{\mathrm{in}} = N_L/2\,, \tag{5.4d}$$

where N_L is the number of photons than are within an optical pulse of duration τ. For the output meanfield Stokes parameter we use Eq. (3.34) with $\delta_t S_i \approx \tau^{-1}(S_i^{\mathrm{out}} - S_i^{\mathrm{int}})$. Neglecting the tensorial light-atom interaction we get:

$$S_x^{\mathrm{out}} = S_x^{\mathrm{in}}\,, \tag{5.5a}$$

[8] Additional calibrations such as the detection noise scaling and the verification of a *shot-noise-limited* sensitivity are not discussed in this work. These investigations have been addressed in [95].

$$S_y^{\text{out}} = G_1^{(f)} S_x^{\text{in}} F_x^{(f)} \ , \tag{5.5b}$$

$$S_z^{\text{out}} = S_z^{\text{in}} \ , \tag{5.5c}$$

$$S_0^{\text{out}} = S_0^{\text{in}} \ . \tag{5.5d}$$

We note that in Eq. (5.5b) the atomic spin projection $F_x^{(f)}$ is assumed to be constant over the entire pulse duration τ. This conditions is generally not met, however it is possible to subdivide the optical pulse into smaller sub-pulses for which the atomic spin evolution is negligible and Eq. (5.5b) still applies. We index these *virtual* sub-pulses by $n \in [0, 1, 2...]$ and write their duration as $\tau_n \ll \tau$. For each of the sub-pulses we have:

$$S_y^{\text{out}}[t_n] = G_1^{(f)} \, S_x^{\text{in}}[t_n] \, F_x^{(f)}[t_n] \ , \tag{5.6}$$

where $t_n = \sum_{n' \leqslant n} \tau_{n'}$.

The rotation experienced by the light polarization ϕ can be directly inferred from the output Stokes parameters. Moreover, in the weak interaction limit $|\phi| \ll 1$ we obtain a linear relation between the polarization rotation angle and the atomic spin projection. This connection is the working principle behind our Faraday rotation probing and we write it as

$$2\phi[t_n] \approx S_y^{\text{out}}[t_n] / S_x^{\text{out}}[t_n] = G_1^{(f)} F_x^{(f)}[t_n] \ . \tag{5.7}$$

Hyperfine selective light-atom interaction

The hyperfine dependent Faraday interaction is achieved by using separate probing lights for $f = 1$ and $f = 2$. Their frequencies are adjusted such that $|G_1^{(1)} / G_1^{(2)}| \gg 1$ for the $f = 1$ probing light and $|G_1^{(1)} / G_1^{(2)}| \ll 1$ for the $f = 2$ probing light. As a result, the polarization of the $f = 1$ ($f = 2$) probe beam primarily couples to the spin projection of $f = 1$ ($f = 2$). In Table 5.2 we compare the coupling coefficients for distinct operational points of the $f = 1$ and $f = 2$ Faraday probe. The residual cross-coupling between the Faraday readouts of $f = 1$ ($f = 2$) and the spin projections in $f = 2$ ($f = 1$) are suppressed by more than an order of magnitude.

Faraday probing setup and data post-processing

The experimental arrangement for the hyperfine selective Faraday probing setup is shown in Fig. 5.10. The probing light is typically composed of two 40 µs long optical pulses and separated by a 20 µs downtime. The first pulse corresponds to the $f = 1$ Faraday probe and uses the repumper (r) laser source. The second pulse probes the $f = 2$ manifold and uses the cooler (c) laser source. For a discussion

Probe	$\Delta^{(10')}/2\pi$	$\Delta^{(23')}/2\pi$	$G_1^{(1)}/(\lambda_0^3/\pi\lambda A)$	$G_1^{(2)}/(\lambda_0^3/\pi\lambda A)$
$f=1$	$-270\,\mathrm{MHz}$	$6069\,\mathrm{MHz}$	$\mathbf{3.67\times10^{-3}}$	1.27×10^{-4}
$f=1$	$-570\,\mathrm{MHz}$	$5769\,\mathrm{MHz}$	$\mathbf{1.62\times10^{-3}}$	1.34×10^{-4}
$f=2$	$-5979\,\mathrm{MHz}$	$360\,\mathrm{MHz}$	1.31×10^{-4}	$\mathbf{2.50\times10^{-3}}$

Table 5.2.: Coupling coefficients $G_1^{(f)}$ of the vector light-atom interaction for $f=1$ and $f=2$ evaluated at the operational points of the Faraday probe. In this work the $f=1$ Faraday probe is detuned below the closed $1\to0'$ transition $\Delta^{(10')}/2\pi\in\{-570\,\mathrm{MHz},-270\,\mathrm{MHz}\}$ and the $f=2$ Faraday probe frequency is located above the closed $2\to3'$ transition $\Delta^{(23')}/2\pi=360\,\mathrm{MHz}$. We highlight the couplings between probe f and hyperfine manifold f, the remaining couplings quantify the residual crosstalks between Faraday readouts.

on the probe frequencies, i.e. detunings, please refer to the subsection above. The optical pulses are combined through a fibre splitter and undergo a polarization cleaning stage, formed by polarizing beam-splitters (PBS) as well as $\lambda/2$ and $\lambda/4$ waveplates, that ensure a linear polarization. At this point, the optical field is split by a non-polarizing beam splitter (BS). One half of the light field is sent to an auxiliary photodiode (PD) which measures the instantaneous optical power. The other half interacts with the SBEC and its polarization gets rotated by an angle $\phi=G_1^{(f)}F_x^{(f)}/2$. In order to measure ϕ, the light is sent through a polarimeter, formed by a $\lambda/2$ waveplate, a PBS and a differential photo-detector (diff PD), which is adjusted to measure the photon number difference between the $\pm45°$ polarization modes. The polarimeter operates in a balanced configuration, such that both outputs of the PBS carry the same optical power when $\phi=0$. When $\phi\neq0$, a power imbalance arises, which is measured by the differential photodetector. The differential photodetector [119] is based on two photodiodes in a differential arrangement and connected to a charge sensitive preamplifier that integrates and amplifies the difference in the photodiode currents. The diff PD ① and PD ② signals are recorded on a STEMLab 125-14 (*Red Pitaya*) board, which is triggered by the experiment control system and features an acquisition rate of 125MS/s (8 ns sampling period). After completion of the experimental sequence, the recorded traces are transferred to the host PC. There, the data post-processing converts traces ① and ② into the Stokes parameters S_y and S_x, from which the Faraday rotation angle ϕ is inferred. The post-processing of this work is based on a *virtual* stroboscopic probing (sub-µs probing pulses). We outline the process below:

(i) Each data sample of trace ① is considered a virtual sub-pulse of duration $\tau_n = 8\,\text{ns}$. We compute the contribution of each sub-pulse to the measured differential signal by computing the increments: $\Delta V_1[t_n] \equiv V_1[t_n] - V_1[t_{n-1}]$. The increments are multiplied by the calibrated gain of the differential detector to obtain the Stokes parameter $S_y^{\text{out}}[t_n]$. Thereafter, we apply a first order order low-pass filter, with a cut-off frequency $f_c = 1\,\text{MHz}$ that is far above the Larmor frequency atomic spins $|\omega_0^{(f)}|/2\pi \sim 84\,\text{kHz}$.

(ii) The data samples of trace ② are scaled by the calibrated gain of the auxiliary photodetector and undergo a similar low-pass filtering stage ($f_c = 1\,\text{MHz}$). The result is the Stokes parameter $S_x^{\text{out}}[t_n]$.

(iii) The resulting $S_y^{\text{out}}[t_n]$ and $S_x^{\text{out}}[t_n]$ arrays are divided to obtain $\phi[t_n]$, as described in Eq. (5.7).

(iv) The Stokes parameter S_x^{out} is integrated to obtain the total number of photons $\mathcal{N}_L[t_n]$ that have interacted with the atomic ensemble since the start

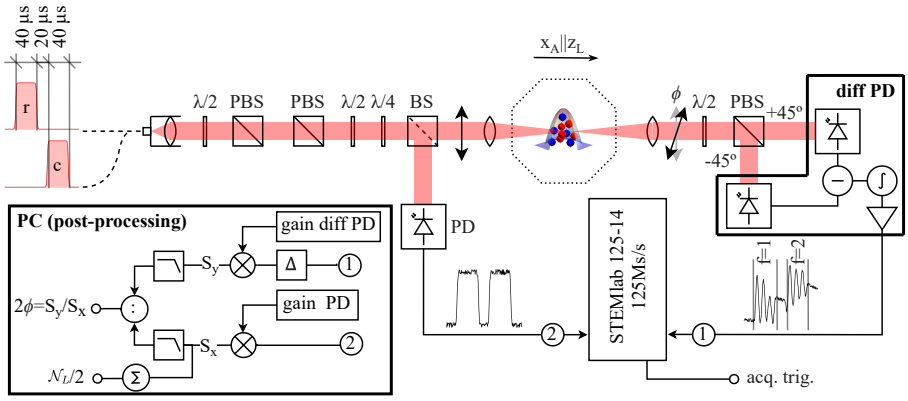

Figure 5.10.: Schematic of the Faraday rotation probing setup. Signal ① illustrates typical Faraday rotation signals for $f = 1$ and $f = 2$, interrogated with light sourced from the repumper (r) and cooler (c) lasers, respectively. Oscillations are caused by the Larmor precession of the atomic spins. Signal ② shows the typical probing pulse shapes captured by the auxiliary photodiode. The data post-processing is detailed in the text below.

of the Faraday probing pulse:

$$\mathcal{N}_L[t_n] = \sum_{n' \leqslant n} N_L[t_{n'}] = 2 \sum_{n' \leqslant n} S_x^{\text{out}}[t_{n'}] \,. \tag{5.8}$$

Calibration of the auxiliary photodetector

The readout of the auxiliary photo detector is used to estimate the Stokes parameter S_x^{out}. Note that this Stokes parameter needs to be evaluated at the same position where S_y^{out} is estimated, i.e. at the output of the optical chamber. As a result, we require a calibration that relates photodetector voltage to the optical power at the output of the optical chamber. At this position, a powermeter was placed and we recorded its readout and the auxiliary photo detector voltage for different optical probing powers. The results are shown in Fig. 5.11, where the obtained slope is the power calibration for the auxiliary PD. Using equation Eqs. (5.4) and (5.5) for a pulse of duration τ and an auxiliary photodetector

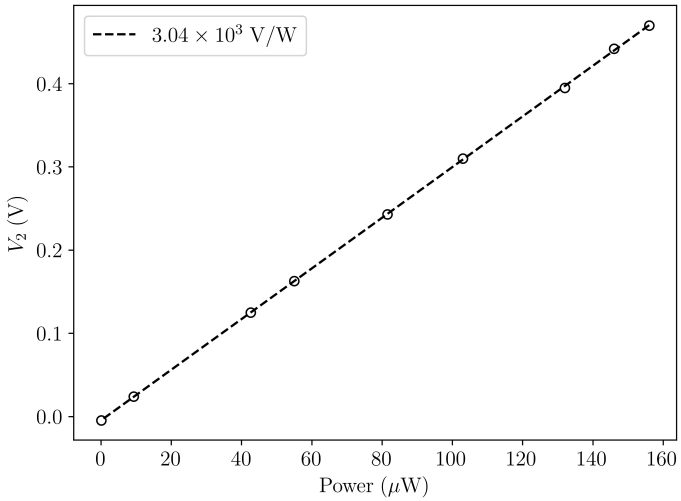

Figure 5.11.: Power calibration of the auxiliary photodetector. V_2 is the auxiliary photodetector voltage as measured on input channel 2 of the STEM-Lab 125-14 board. Optical power measurements are performed by a powermeter placed at the output of the optical chamber. Calibration performed in absence of ^{87}Rb atoms.

voltage V_2 we have:

$$S_x^{\text{out}} = \frac{N_L}{2} = \frac{\tau V_2}{2\hbar\omega} \times \frac{1}{3.04 \times 10^3\,\text{V/W}}\,, \tag{5.9}$$

where N_L is the total photon number and $\omega = 2\pi c/\lambda$ is the probe photon frequency. We can rewrite Eq. (5.9) in terms of virtual sub-pulses with a duration equal to our acquisition sampling period $\tau = 8\,\text{ns}$ and a discrete time variable defined as $t_n = n \times \tau$. Doing so for the Faraday probing of the ^{87}Rb $\mathcal{D}_2$ line ($\lambda = 780.2\,\text{nm}$) we obtain $S_x^{\text{out}}[t_n] = V_1[t_n] \times (5.17 \times 10^6\,\text{V}^{-1})$.

Calibration of the differential photodetector

The calibration of the differential photodetector voltage V_1 requires separate evaluation of the response of the two internal photodiodes that measure the light intensity at the $+45°$ and $-45°$ arms of the PBS. To this end, we fully unbalance the detector by rotating the $\lambda/2$ waveplate such that the incoming Faraday probing light is exclusively propagating through the $+45°$ ($-45°$) arm. Under this configuration, optical pulses are sent to the differential photodetector, which results in positive (negative) differential photodiode currents that are integrated within the differential detector. For this calibration we use $20\,\mu\text{s}$ long optical pulses and perform a scan over the optical pulse power. The corresponding differential photodector signal are $20\,\mu\text{s}$ long positive (negative) voltage ramp, where the slope is proportional to the optical pulse power. In Fig. 5.12 we show the measured voltage slopes for the $+45°$ ($-45°$) configuration as a function of the optical power recorded on the auxiliary photodetector.

We can applying the result to a balanced configuration and a general pulse duration τ, the photon number along the $+45°$ ($-45°$) arm of the PBS are $N_{L,+45°}$ ($N_{L,-45°}$) and the Stokes parameter S_y^{out} reads.

$$\begin{aligned} S_y^{\text{out}} =& \frac{1}{2}\left(N_{L,+45°}^{\text{out}} - N_{L,-45°}^{\text{out}}\right) \\ =& \frac{\tau\partial_t V_1}{4\hbar\omega} \times \left(\frac{1}{3.10 \times 10^{12}\,\text{V/Ws}} - \frac{1}{-3.08 \times 10^{12}\,\text{V/Ws}}\right)\,, \end{aligned} \tag{5.10}$$

Earlier in this section we have introduced the increment in the differential photodetector signal $\Delta V_1[t_n] \equiv V_1[t_n] - V_1[t_{n-1}]$. The increment connects to the time derivative $\nabla V_1[t_n] \approx \tau\partial_t V_1$, where $\tau = t_n - t_{n-1} = 8\,\text{ns}$ is the acquisition sampling period. In terms of virtual sub-pulses and for the Faraday probing of the ^{87}Rb $\mathcal{D}_2$ line we rewrite Eq. (5.10) as $S_y^{\text{out}}[t_n] = \nabla V_1[t_n] \times (6.35 \times 10^5\,\text{V}^{-1})$.

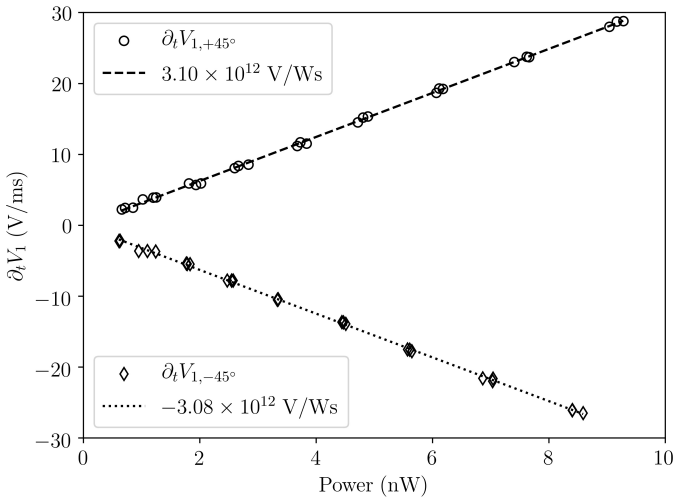

Figure 5.12.: Power calibration of the differential photodetector. V_1 is the differential photodector voltage as measured on input channel 1 of the *Red Pitaya STEMLab 125-14* board. The auxiliary photodetector is simultaneously sampled on channel 2 and is used to estimate the optical power. We label as $V_{1,+45^\circ}$ ($V_{1,-45^\circ}$) the differential photodetector voltage in an unbalanced configuration, where the incoming Faraday probing light is exclusively propagating through the $+45^\circ$ (-45°) arm of the PBS. Calibration performed in absence of ^{87}Rb atoms.

Faraday rotation measurements and estimation of $G_1^{(f)}$

As previously explained, a typical Faraday rotation measurement consists of a 40 µs long $f = 1$ Faraday probing pulse, followed by 20 µs delay and a 40 µs long $f = 2$ Faraday probing pulse. The resulting auxiliary and differential photodetector signals are combined in the data post-processing yielding the Stokes parameters S_x^{out}, S_y^{out}, the polarization rotation ϕ and the integrated number of photons $\mathcal{N}_L$ (see Fig. 5.10 and discussion below it). We analyse the Faraday rotation signals with a fit model that merges the atomic spin evolution and the light-atom interaction. The first one is described in Eq. (2.18), where the LZS introduces oscillations in the transverse spin projections $F_x^{(f)}$ and $F_y^{(f)}$. The second one connects the atomic atomic spin projection to the observed rotation signal (Eq. (5.7)) and describes the depolarization due to off-resonant photon

absorption events (Eq. (3.30)). Combining them we get:

$$\phi[t_n] = \frac{1}{2} G_1^{(f)} F_x^{(f)}[t_n] \,, \tag{5.11a}$$

$$F_x[t_N] = \underline{\underline{F_\perp^{(f)}}} \times \exp\left(-\mathcal{N}_L[t_n]/\underline{\underline{N_{L,\mathrm{dep}}^{(f)}}}\right) \times \cos\left(\omega^{(f)} t_n + \underline{\underline{\theta^{(f)}}}\right) \,. \tag{5.11b}$$

The highlighted free fit parameters are the spin orientation angle $\theta^{(f)}$, the transverse magnetisation $F_\perp^{(f)}$ and the characteristic depolarization photon number $N_{L,\mathrm{dep}}^{(f)}$. The Larmor precession frequency $\omega^{(f)}$ is a constant contribution since the Faraday probe is typically operated under the same constant magnetic field. It can be estimated by including it as a free fit parameter in Eq. (5.11) or from a scan of the rf driving frequency as shown in Fig. 5.4. Also the light-atom interaction constant $G_1^{(f)}$ must be calibrated. We detail the processes in the following.

The $G_1^{(f)}$ calibration compares the obtained rotation signal for a known atomic state. In particular, it uses a transversally oriented state $F_{\perp,0}^{(f)} = fN_A$ in $f = 1$ ($f = 2$), which is prepared through the combination of mw and rf pulses shown in Table 5.3. After state preparation, the Faraday probing pulses are applied and the obtained traces are fit to Eq. (5.11). In this case, we include $G_1^{(f)}$ as a free fit parameter while constraining the initial transverse magnetisation to $F_\perp^{(f)} = fN_A$, where the atom number N_A has been estimated through absorption imaging prior to this calibration. Measurements for the calibration of $G_1^{(1)}$ ($G_1^{(2)}$) are shown at the end of this section in Fig. 5.13 (Fig. 5.14). The upper charts show the readout from the differential V_1 and auxiliary photodetector V_2, the lower charts show the inferred rotation angle $\phi \propto \partial_t V_1$ and integrated photon number $\mathcal{N}_L \propto \int V_2 dt$. The fits to the $f = 1$ ($f = 2$) rotation signals are shown in blue (red). Comparing the amplitude of the fitted signals, we see that the $f = 1$ ($f = 2$) Faraday probe primarily couples to $F_\perp^{(1)}$ ($F_\perp^{(2)}$) and that the residual crosstalk amplitudes are suppressed by more than one order of magnitude. We collect the experimentally inferred $G_1^{(f)}$ in Table 5.4.

Item	Rotation	Type	Coupled levels	$\rho^{(1)}$	$\rho^{(2)}$
0				$(0,1,0)$	$(0,0,0,0,0)$
1	$\mathcal{R}_\pi$	mw	$\|1,0\rangle \leftrightarrow \|2,0\rangle$	$(0,0,0)$	$(0,0,1,0,0)$
2	$\mathcal{R}_\pi$	mw	$\|1,-1\rangle \leftrightarrow \|2,0\rangle$	$(0,0,1)$	$(0,0,0,0,0)$
3a	$\mathcal{R}_{\pi/2}$	rf	$\|f,m\rangle \leftrightarrow \|f,m\pm 1\rangle$	$(\frac{1}{4},\frac{1}{2},\frac{1}{4})$	$(0,0,0,0,0)$
3b	$\mathcal{R}_\pi$	mw	$\|1,-1\rangle \leftrightarrow \|2,-1\rangle$	$(0,0,0)$	$(0,0,0,0,1)$
4b	$\mathcal{R}_{\pi/2}$	rf	$\|f,m\rangle \leftrightarrow \|f,m\pm 1\rangle$	$(0,0,0)$	$(\frac{1}{16},\frac{1}{4},\frac{3}{8},\frac{1}{4},\frac{1}{16})$

Table 5.3.: Mw and rf pulse sequence for the generation of a transversally stretched state in either $f = 1$ or $f = 2$. The sequence branches into (a) for $f = 1$ or (b) for $f = 2$. Rotations are defined in Table 4.2 and the relative populations read $\rho_m^{(f)} = |\xi_m^{(f)}|^2/N_A$.

Probe	$\Delta^{(10')}/2\pi$	$\Delta^{(23')}/2\pi$	$G_1^{(1)}$[rad/spin]	$G_1^{(2)}$[rad/spin]
$f = 1$	-270 MHz	6069 MHz	$\mathbf{3.15(25)\times 10^{-7}}$	$1.61(32)\times 10^{-8}$
$f = 1$	-570 MHz	5769 MHz	$\mathbf{1.67(12)\times 10^{-7}}$	-
$f = 2$	-5979 MHz	360 MHz	$9.46(45)\times 10^{-9}$	$\mathbf{1.78(14)\times 10^{-7}}$

Table 5.4.: Measured coupling coefficients $G_1^{(f)}$ for the distinct $f = 1$ and $f = 2$ probe detunigs of this work. We highlight the couplings between probe f and hyperfine manifold f, the remaining couplings quantify the residual crosstalk between Faraday readouts. The first and last row are obtained from the data set shown in Fig. 5.13 and Fig. 5.14. The row in between corresponds to a separate data set, where the cross-coupling was not estimated.

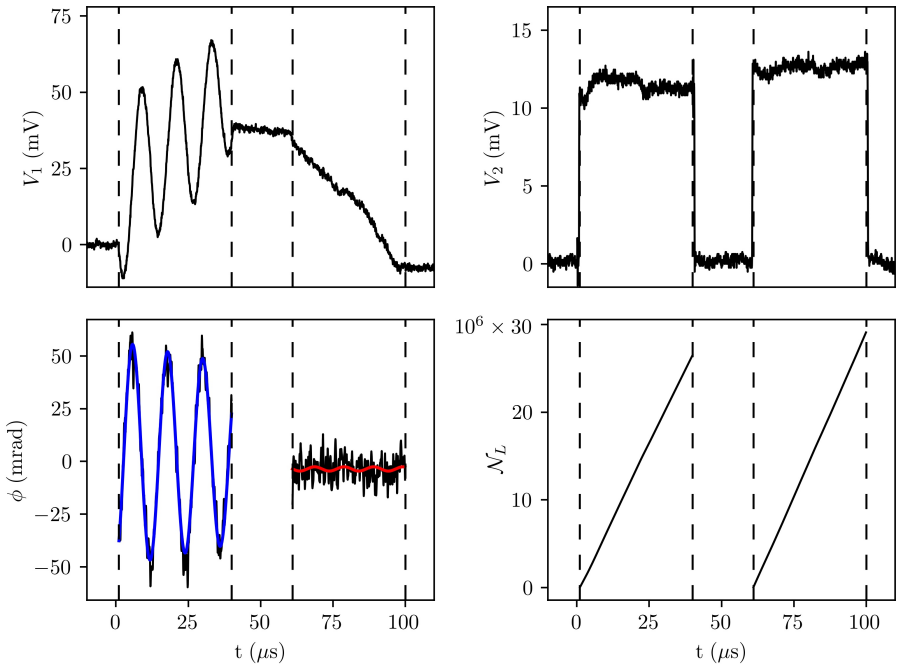

Figure 5.13.: Faraday rotation measurement of a transversely oriented SBEC in $f = 1$ ($F_\perp^{(1)} = N_A$, $F_\perp^{(2)} = 0$). The upper subfigures show the raw differential photodetector voltage V_1 and the auxiliary photodetector voltage V_2. Below them are the corresponding polarization rotation $\phi \propto \partial_t V_1$ and the integrated photon number $\mathcal{N}_L \propto \int V_2 dt$. Blue and red curves show the best fit estimates of the rotation signal based on Eq. (5.11). The total atom number is $N_A = 8.64(14) \times 10^4$ and the detunings of the $f = 1$ and $f = 2$ Faraday probes are $\Delta^{(10')}/2\pi = -270\,\mathrm{MHz}$ and $\Delta^{(23')}/2\pi = 360\,\mathrm{MHz}$, respectively.

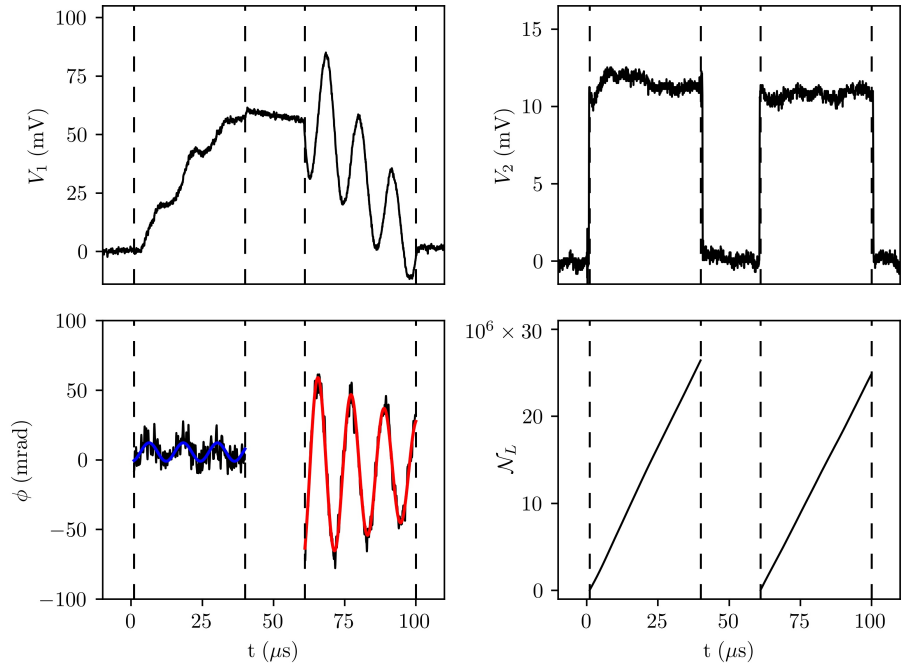

Figure 5.14.: Faraday rotation measurement of a transversely oriented SBEC in $f = 2$ ($F_\perp^{(1)} = 0$, $F_\perp^{(2)} = 2N_A$). The upper subfigures show the raw differential photodetector voltage V_1 and the auxiliary photodetector voltage V_2. Below them are the corresponding polarization rotation $\phi \propto \partial_t V_1$ and the integrated photon number $\mathcal{N}_L \propto \int V_2 dt$. Blue and red curves show the best fit estimates of the rotation signal based on Eq. (5.11). The visible depolarization, i.e. exponential damping in the polarization rotation, is caused by off-resonant photon absorption and is particularly visible for the $f = 2$ trace. Total atom number and Faraday probe detunings are equal to Fig. 5.13.

6

Bose-Einstein condensate comagnetometer

The value of paired magnetic sensors was first demonstrated in the early days of modern magnetism, when C. F. Gauss [120, 121] used paired compasses to perform the first absolute geomagnetic field measurements. In contemporary physics, paired magnetic sensors enable comagnetometer-based searches for new physics [122, 123]. In a *comagnetometer*, colocated magnetometers respond in the same way to a magnetic field, but have different sensitivities to other, weaker influences. Differential readout then allows high-sensitivity detection of the weak influences with greatly reduced sensitivity to magnetic noise. Comagnetometers have been used to investigate anomalous spin interactions [124, 125, 126, 127, 128] and spin-gravity couplings [129, 130, 131] and for stringent tests of Lorentz invariance and CPT violation [132, 133, 134, 135, 136, 137]. Further applications are found in inertial navigation and gyroscopes built upon atomic spin comagnetometers [138, 139, 140, 141]. Implementations with miscible mixtures include atomic vapors [142, 143] and liquid-state NMR with different nuclear spins [144, 145].

In this chapter we discuss the development of a comagnetometer implemented on a SBEC in a superposition of $f = 1$ and $f = 2$, which has been reported in [52]. A challenge for this strategy is the relatively short lifetime of the $f = 2$ manifold produced by exothermic $2 \rightarrow 1$ hyperfine-relaxing collisions [66, 146]. We strongly suppress these collisions by using the spin-dependent interaction at low magnetic fields to lock the spins in a stretched state. In this way we achieve $\sim$1 s lifetimes in $f = 1, 2$ mixtures and demonstrate a field noise rejection of 44.0(8) dB in the comagnetometer readout.

6.1. State preparation and probing

The comagnetometer is implemented on a coherent superposition of the $f = 1$ and $f = 2$ hyperfine manifolds. After the all-optical evaporation the SBEC is transferred from the polar state $\xi/\sqrt{N_A} = (0, 1, 0)^T \oplus \mathbf{0}_5^T$ into transversally

stretched states in $f = 1$ and $f = 2$. The applied mw and rf pulse sequence is shown in Table 6.1. First, a rf $\pi/2$ pulse rotates the polar state into $\xi/\sqrt{N} = (1/\sqrt{2}, 0, 1/\sqrt{2})^T \oplus \mathbf{0}_5^T$. A mw π pulse on the $|f = -1, m = -1\rangle \leftrightarrow |f = 2, m = -2\rangle$ transition then produces the state $\xi/\sqrt{N_A} = (1/\sqrt{2}, 0, 0)^T \oplus (0, 0, 0, 0, 1/\sqrt{2})^T$, which describes a stretched state oriented along (against) the magnetic field for the $f = 1$ ($f = 2$) manifold. Finally, both spins are simultaneously rotated into the **x**-**y** plane by means of a second rf $\pi/2$ pulse.

Item	Rotation	Type	Coupled levels	$\rho^{(1)}$	$\rho^{(2)}$
0				$(0, 1, 0)$	$(0, 0, 0, 0, 0)$
1	$\mathcal{R}_{\pi/2}$	rf	$\|f, m\rangle \leftrightarrow \|f, m \pm 1\rangle$	$(\frac{1}{2}, 0, \frac{1}{2})$	$(0, 0, 0, 0, 0)$
2	$\mathcal{R}_{\pi}$	mw	$\|1, -1\rangle \leftrightarrow \|2, -2\rangle$	$(\frac{1}{2}, 0, 0)$	$(0, 0, 0, 0, \frac{1}{2})$
3	$\mathcal{R}_{\pi/2}$	rf	$\|f, m\rangle \leftrightarrow \|f, m \pm 1\rangle$	$(\frac{1}{8}, \frac{1}{4}, \frac{1}{8})$	$(\frac{1}{32}, \frac{1}{8}, \frac{3}{16}, \frac{1}{8}, \frac{1}{32})$

Table 6.1.: Mw and rf pulse sequence for the generation of a transversally stretched state in $f = 1$ and $f = 2$. Rotations are defined in Table 4.2 and the relative populations read $\rho_m^{(f)} = |\xi_m^{(f)}|^2/N_A$.

To independently probe the spin ensembles in $f = 1$ and $f = 2$, we use the hyperfine-selective Faraday probe introduced in Section 5.3.4. The Faraday readout yields the transverse spin amplitude $F_\perp^{(f)}$ and its azimuthal angle $\theta^{(f)}$.

6.2. Magnetic evolution

As discussed in Section 2.2 the magnetic field contribution to the spin dynamics splits into LZS and QZS. In the following we describe how they influence the dynamics of the $f = 1, 2$ spinor BEC comagnetometer.

6.2.1. Linear Zeeman splitting

In the transverse plane, the spin manifolds precess around the magnetic field in opposite directions. Under the SMA, $f = 1$ and $f = 2$ experience exactly the same external magnetic field and their angular evolutions read:

$$\theta^{(f)}(t) = \theta_0^{(f)} + \gamma^{(f)} \int_0^t dt'\, B(t') \,, \tag{6.1}$$

where the azimuth spin orientation $\theta^{(f)}$ is defined in Eq. (2.16c) and $\theta_0^{(f)}$ is its initial value right after the second rf rotation. The gyromagnetic ratio $\gamma^{(f)}$ for $f = 1$ and $f = 2$ is given in Eq. (2.12).

The spin orientation angle $\theta^{(f)}$ directly relates to applied magnetic field. In particular, we can use Eq. (6.1) to estimate the precision in the estimated DC magnetic field δB as a function of the precision in the azimuth angle $\delta\theta^{(f)}$ and the free evolution time t:

$$\delta B = \frac{1}{|\gamma^{(f)}|t}\delta\theta^{(f)} \ , \tag{6.2}$$

We write the precision in the azimuth angle as $\delta\theta^{(f)} = \delta F_x^{(f)}/F_\perp^{(f)}$, where $\delta F_x^{(f)}$ is the precision in the measured spin projection along $\mathbf{x}$. Assuming an atomic projection-noise limited measurement we get $[\delta F_x^{(f)}]_A = \sqrt{fN_A/2}$. Similarly, if the measurement is limited by the photon shot-noise of the Faraday probe we have $[\delta F_x^{(f)}]_L = 1/(G_1^{(f)}\sqrt{N_L})$. More generally, the atomic spin projection-noise and photon shot-noise are independent contributions and they can be combined into Eq. (6.2) as:

$$\delta B = \sqrt{[\delta B]_A^2 + [\delta B]_L^2} \ , \tag{6.3a}$$

$$[\delta B]_A = \frac{1}{|\gamma^{(f)}|t}\frac{\sqrt{fN_A/2}}{F_\perp^{(f)}} \geqslant \frac{1}{|\gamma^{(f)}|t}\frac{1}{\sqrt{2fN_A}}, \tag{6.3b}$$

$$[\delta B]_L = \frac{1}{|\gamma^{(f)}|t}\frac{1}{F_\perp^{(f)}G_1^{(f)}\sqrt{N_L}} \geqslant \frac{1}{|\gamma^{(f)}|t}\frac{1}{fN_AG_1^{(f)}\sqrt{N_L}} \ . \tag{6.3c}$$

The inequalities in Eq. (6.3b) and Eq. (6.3c) saturate for fully oriented states $F_\perp^{(f)} = fN_A$. The limited lifetime and coherence time can be included through a single parameter τ, which scales the magnetic precisions as $[\delta B]_A \propto \exp(t/2\tau)/t$ and $[\delta B]_L \propto \exp(t/\tau)/t$. As a result, the optimal evolution time is $t = 2\tau$ for atomic projection-noise limited measurements and $t = \tau$ for photon shot-noise limited measurements.

6.2.2. Quadratic Zeeman splitting

The QZS modulates $F_\perp^{(f)}$ and drives coherent orientation-to-alignment oscillations (see Fig. 2.1), e.g. from $F_\perp^{(f)} = fN_A^{(f)}$ to $F_\perp^{(f)} = 0$ and back. For $f = 1$, these oscillations are only a minor inconvenience; they allow full-signal measurements but only at certain times.[1] The situation is distinct for $f = 2$, where non-oriented states $F_\perp^{(2)} < 2N_A^{(2)}$ undergo $f = 2 \to f = 1$ hyperfine relaxing collisions. In this case, the QZS directly impacts the lifetime of the ensemble since it drives the system from stable (oriented) to lossy (aligned) spin states. This process is described in the following section, together with a mitigation technique based on the competition between QZS and the spin contact interaction.

[1] Alternatively, the orientation-to-alignment dynamics can be reversed by a mw manipulation prior to the Faraday probe pulse. See Fig. 4.4 and discussion above it.

6.3. Hyperfine relaxing collisions

In a hyperfine relaxing collision, the liberated energy is transferred to the motional degree of freedom, which expels the colliding atoms from the trap [66]. This process makes it difficult not only to achieve condensation in $f = 2$, but also to observe coherent spinor dynamics in the $f = 2$ state and in $f = 1, 2$ mixtures.

We divide these collisions based on the hyperfine manifolds the colliding atoms belong to. This is, when they belong to $f = 1$ and $f = 2$ we write the collision as $1 \asymp 2$. Similarly, when both atoms are in $f = 2$ we write the collisions as $2 \asymp 2$. For the state preparation described in Section 6.1, where $f = 1$ and $f = 2$ precess in opposite directions, hyperfine relaxing collisions of type $1 \asymp 2$ are unavoidable and set an upper limit on the lifetime of the ensemble. In contrast, the stronger $2 \asymp 2$ collisions can be suppressed by preserving $f = 2$ in an oriented state.[2]

The stability of oriented spin states is determined by the QZS and the spin interaction. While the QZS drives orientation-to-alignment conversion, the ferromagnetic (antiferromagnetic) spin interaction in $f = 1$ ($f = 2$) [24, 43] opposes to it and can reestablish long $f = 2$ lifetimes. The competition of QZS and spin interaction effects is parametrized by the ratio $\eta^{(f)} \equiv |E_q^{(f)}/E_{\text{spin}}^{(f)}|$, where the QZS and spin interaction energies of a transverse stretched state in hyperfine manifold f are

$$E_q^{(f)} = (-1)^{f-1} \frac{\left(\hbar\gamma^{(f)} B\right)^2}{\hbar\omega_{\text{hfs}}} \frac{fN^{(f)}}{2} , \tag{6.4a}$$

$$E_{\text{spin}}^{(f)} = \frac{g_1^{(f)}}{2V_{\text{eff}}} \left(fN^{(f)}\right)^2 . \tag{6.4b}$$

Here $\omega_{\text{hfs}} = 2\pi \times 6.8\,\text{GHz}$ is the $f = 1, 2$ hyperfine splitting frequency and the spin interaction coefficients $g_1^{(f)}$ and effective volume V_{eff} are defined in Chapter 2.

[2] The suppression of hyperfine relaxing collisions is easily understood in terms of angular momentum conservation. We follow the notation for the scattering lengths $a_{\mathcal{C}}^{\mathcal{F}}$ and label by $\mathcal{C}$ the total spin of the collision channel. In the case of pairs of $f = 1, 1$ atoms, the total spin of the collision channel is within $\mathcal{C} \in \{0, 1, 2\}$. Similarly, for pairs of $f = 1, 2$ and $f = 2, 2$ atoms we have $\mathcal{C} \in \{1, 2, 3\}$ and $\mathcal{C} \in \{0, 1, 2, 3, 4\}$, respectively. Collision channels with $\mathcal{C} > 2$ cannot relax into $f = 1$ and are preserved from hyperfine relaxation. Applying it to the spin state prepared in Section 6.1 we see that:

- The $f = 1$ and $f = 2$ manifolds precess in opposite directions and they continuously oscillate between parallel ($\mathcal{C} = 3$) and anti-parallel spin configurations ($\mathcal{C} = 1$). As a result, we cannot avoid hyperfine relaxing collisions of type $1 \asymp 2$.
- The $f = 2$ manifold is initially prepared in an oriented states and $\mathcal{C} = 4$. Hyperfine relaxing collisions of type $2 \asymp 2$ can be suppressed if $f = 2$ is preserved in an oriented state.

When $\eta^{(f)} \gtrsim 1$, the system is driven by the QZS and transversely oriented states undergo orientation-to-alignment oscillations and $2 \asymp 2$ hyperfine-relaxation occur. On the other hand, when $\eta^{(f)} \ll 1$, initially stretched $f = 2$ states become stable and $2 \asymp 2$ hyperfine-relaxing collisions are suppressed. Experimental results for the two distinct regimes are given in Fig. 6.1, where we evaluate the orientation-to-alignment oscillations and hyperfine-relaxing relaxation for different applied magnetic fields. We show the transverse degree of polarization $F_{\perp}^{(f)}/(fN_A)$ versus evolution time t, where the atom number $N_A = 2F_{\perp}^{(1)}(t = 0)$ is estimated from the first $f = 1$ Faraday rotation signal. The state preparation (see Section 6.1) is performed at $B = 282\,\mathrm{mG}$, results in a superposition of transversely oriented states $\xi/\sqrt{N_A} = \hat{R}_{\pi}^{(1)}[\pi/2](1/\sqrt{2}, 0, 0)^T \oplus \hat{R}_0^{(2)}[\pi/2](0, 0, 0, 0, 1/\sqrt{2})^T$, where $\hat{R}_{\alpha}^{(f)}[\beta]$ is the rotation operator[3] for hyperfine manifold f. Thereafter, the magnetic field is ramped in 4 ms to a value of $\mathrm{B} = \{381\,\mathrm{mG}, 277\,\mathrm{mG}, 120\,\mathrm{mG}\}$ for free evolution. For these magnetic fields, the measured atom number are $N_A = \{1.47(11), 1.05(13), 1.15(14)\} \times 10^5$ and the estimated ratios between QZS and spin interaction energies read $\eta^{(1)} = \{5.62, 3.40, 0.62\}$ and $\eta^{(2)} = \{1.01, 0.61, 0.11\}$, respectively. We note that in order to have a consistent readout process, the field is ramped back to 282 mG in the 4 ms prior to Faraday readout.

We observe clear orientation-to-alignment conversion cycles in $f = 1$ at 381 mG and 277 mG. The oscillatory process is less visible in $f = 2$ due to its stronger spin interaction and rapid atom losses via $2 \asymp 2$ hyperfine relaxing collisions. At 120 mG, $(\eta^{(1)}, \eta^{(2)}) = (0.62, 0.11) \ll 1$ and the spin interaction dominates in both hyperfine manifolds. As a result, $2 \asymp 2$ losses are suppressed and the $\tau \sim 1\,\mathrm{s}$ lifetime is limited by $1 \asymp 2$ hyperfine relaxing collisions.

The experimental results are supported by SMA mean field simulations including intra- and interhyperfine interactions (solid lines in Fig. 6.1). We follow the prescription of Section 2.5 and model hyperfine relaxation by introducing imaginary scattering amplitudes for $1 \asymp 2$ and $2 \asymp 2$ collisions, i.e. $a_{\mathcal{C}}^{(12)} \to a_{\mathcal{C}}^{(12)} - i\tilde{a}_{\mathcal{C}}^{(12)}$ and $a_{\mathcal{C}}^{(2)} \to a_{\mathcal{C}}^{(2)} - i\tilde{a}_{\mathcal{C}}^{(2)}$, where $\mathcal{C}$ is the total spin of a given collision channel. A full set of scattering rates is not known, so for simplicity we take two imaginary scattering amplitudes that describe hyperfine relaxation on all relevant $1 \asymp 2$ and $2 \asymp 2$ collisions channels. This is, $\tilde{a}_{\mathcal{C}}^{(12)} = \tilde{a}^{(12)}$ and $\tilde{a}_{\mathcal{C}}^{(2)} = \tilde{a}^{(2)}$ for $\mathcal{C} \leqslant 2$, and $\tilde{a}_{\mathcal{C}}^{(12)} = \tilde{a}_{\mathcal{C}}^{(2)} = 0$ for $\mathcal{C} > 2$.

The values for $\tilde{a}^{(12)}$ and $\tilde{a}^{(2)}$ are left as free fit parameters. We use the the data for $f = 2$ at $B = 381\,\mathrm{mG}$, where $2 \asymp 2$ collisions are dominant, to obtain $\tilde{a}^{(2)} = 0.692(34)a_B$ while enforcing $\tilde{a}^{(12)} = 0$. Thereafter, we use the estimated $\tilde{a}^{(2)}$ to

[3] We leverage the notation of the spin rotations in Section 4.4.1 and use β for the rotation angle and α for the azimuth angle of the rotation axis. The corresponding spin-f rotation operator reads $\hat{R}_{\alpha}^{(f)}[\beta] \equiv \exp[-i\beta(\cos(\alpha)\hat{f}_x^{(f)} + \sin(\alpha)\hat{f}_y^{(f)})]$.

fit the experimental data for $f = 1$ at $B = 120\,\mathrm{mG}$, yielding $\tilde{a}^{(12)} = 0.018(18)$.

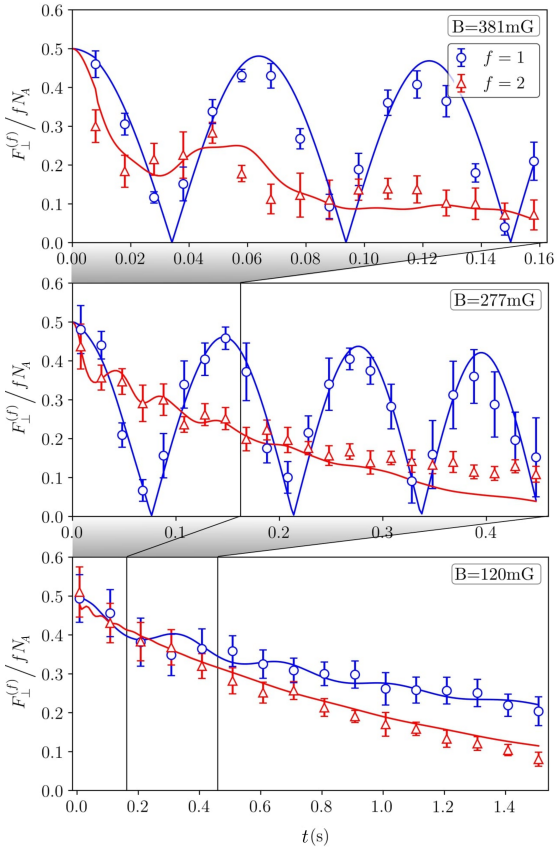

Figure 6.1.: Evolution of the transverse spin magnitude for $f = 1$ (blue circles) and $f = 2$ (red triangles) for decreasing magnetic field strengths B. The reduction in $F_\perp^{(2)}$ results from hyperfine relaxing collisions throughout the evolution time, which is constrained to $t \geqslant 4\,\mathrm{ms}{+}4\,\mathrm{ms}$ by the magnetic ramps at the beginning and end of the experimental sequence. Solid lines are SMA mean-field simulations as described in the text. Error bars show the measured standard deviation in the transverse spin magnitude over 12 experimental repetitions and black vertical lines indicate the temporal extent of the graphs above. The Faraday probe detunings are $\Delta^{(10')}/2\pi = -270\,\mathrm{MHz}$ and $\Delta^{(23')}/2\pi = 360\,\mathrm{MHz}$ (see Table 5.4).

6.4. Magnetic background suppression

A largely B-independent signal is obtained by adding the azimuth estimates defined in Eq. (6.1) to obtain our comagnetometer readout $\theta^{(12)} \equiv \theta^{(1)} + \theta^{(2)}$:

$$\theta^{(12)}(t) = \theta_0^{(12)} - 2\gamma_s \int_0^t dt'\, B(t')\,, \tag{6.5}$$

where $\theta_0^{(12)} = \theta_0^{(1)} + \theta_0^{(2)}$. The magnetic field dependency of the comagnetometer readout is suppressed by the ratio $|\partial_B \theta^{(f)} / \partial_B \theta^{(12)}| \approx \gamma_0/2\gamma_s = 251$ (in amplitude) or 48.0 dB (in power). In contrast, any effect that influences $\theta^{(1)}$ and $\theta^{(2)}$ in the same direction would doubly influence $\theta^{(12)}$.

We proceed by evaluating the comagnetometer common-mode suppression at low magnetic fields, where both hyperfine manifolds are long lived. To this end, a constant bias magnetic field of 120 mG is applied for state preparation, hold time and Faraday readout. This removes the temporal overhead of the previously required magnetic ramps such that hold times down to 20 µs are accessible, limited only by the hardware timing of the experiment.

We measure the spread in estimated azimuth angles $\theta^{(f)}$ and comagnetometer signal $\theta^{(12)}$ as a function of hold time t, with results shown in Fig. 6.2. We employ as a cyclic statistic the *sharpness* $S \equiv |\langle \exp[i\theta] \rangle|$ [147], where $\langle \cdot \rangle$ here indicates the sample mean and θ is an angle variable, e.g. $\theta^{(f)}$ or $\theta^{(12)}$. $S^2 = 1$ indicates no spread of θ while S^2 near zero indicates a large spread.

We can relate the loss of sharpness with increasing t seen in Fig. 6.2 to the magnetic noise as follows. First we note that the hold time t is always small relative to the time between measurements and that by Eq. (6.1), $\theta^{(f)}$ is most sensitive to the DC component of $B(t)$. This motivates a quasistatic model, where the field B is constant during free evolution and normally distributed from shot to shot, with variance σ_B^2. Consequently $\theta^{(f)}$ and $\theta^{(12)}$ are normally distributed, with rms deviations $\sigma_{\theta^{(f)}} = |\gamma^{(f)}| \sigma_B t \approx \gamma_0 \sigma_B t$ and $\sigma_{\theta^{(12)}} = 2\gamma_s \sigma_B t$.

For normally distributed θ and sample size K, the expectation of S^2 is

$$\langle S^2 \rangle = \frac{1}{K} + \frac{K-1}{K} e^{-\sigma_\theta^2}. \tag{6.6}$$

This form is fitted to the data of Fig. 6.2 to find $\sigma_{\theta^{(1)}} = 230(20)\,\mathrm{rad\,s^{-1}}\,t$ and $\sigma_{\theta^{(12)}} = 1.45(5)\,\mathrm{rad\,s^{-1}}\,t$.

The ratio between these indicates a common-mode rejection of B fluctuations $|\partial_B \theta^{(1)} / \partial_B \theta^{(12)}| = 159(15)$ in amplitude or 44.0(8) dB in power, in reasonable agreement with the predicted 48 dB rejection. The discrepancy is plausibly due to field drifts during the free evolution, which principally affect larger t and thus $\sigma_{\theta^{(12)}}$.

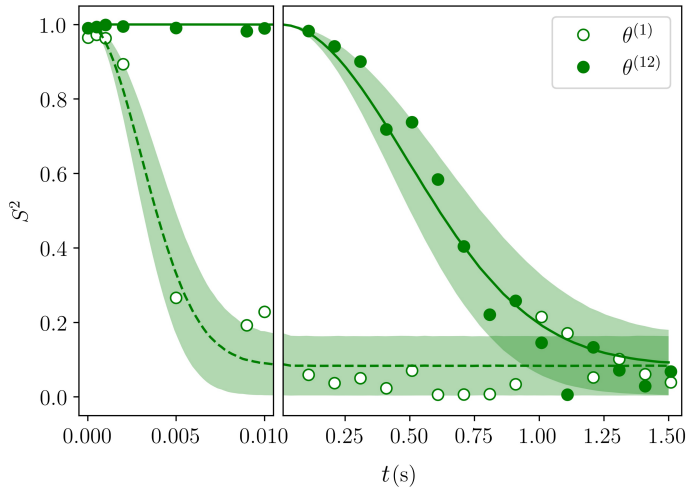

Figure 6.2.: Magnetic noise rejection of the SBEC comagnetometer. Graph shows evolution of S^2, where $S \equiv |\langle \exp[i\theta] \rangle|$ is the sharpness, as a function of hold time t, for $\theta = \theta^{(1)}$ and $\theta = \theta^{(12)}$. Averages are taken over $K = 12$ samples. Sharpness of $\theta^{(2)}$ closely tracks that of $\theta^{(1)}$ and is not shown. Dashed and solid lines show fits assuming a quasistatic field noise model (see Eq. (6.6) and surrounding paragraph), yielding rms deviations in the azimuth angles and comagnetometer readout of $\sigma_{\theta^{(1)}} = 230(20)\,\mathrm{rad\,s^{-1}}t$ and $\sigma_{\theta^{(12)}} = 1.45(5)\,\mathrm{rad\,s^{-1}}t$, respectively. Shaded areas represent the numerically estimated plus and minus one standard deviation in S^2 for the above obtained fit results. The Faraday probe detunings are $\Delta^{(10')}/2\pi = -270\,\mathrm{MHz}$ and $\Delta^{(23')}/2\pi = 360\,\mathrm{MHz}$ (see Table 5.4).

6.5. Sensitivity, extensions and applications

To estimate the sensitivity of the comagnetometer, we use the typical probe photon numbers $N_L \approx 2.5 \times 10^7$, the reported atom numbers $N_A \approx 10^5$ and the vector light-atom couplings in Table 5.4. The described state evolution yields $F_\perp^{(f)} = f N_A^{(f)} e^{-t/t_{\mathrm{coh}}}$, where $N_A^{(f)} = N_A/2$ and $\tau \approx 1\,\mathrm{s}$. The typical experimental cycling time including atom loading, cooling, state initialisation, hold time and probing is $t_{\mathrm{cyc}} \approx 20\,\mathrm{s}$.

We can inserted these quantities into Eqs. 6.3 with $t = \tau$ to obtain Table 6.2. It compares the *single-shot* precision δB and sensitivity $\delta B \sqrt{t_{\mathrm{cyc}}}$ for $f = 1$, $f = 2$ and the comagnetometer readout. We see that the current experimental setup is

	Units	$f = 1$ readout	$f = 2$ readout	Comag. readout
$[\delta B]_A$	T	1.2×10^{-13}	8.4×10^{-14}	1.5×10^{-13}
$[\delta B]_L$	T	7.8×10^{-13}	6.9×10^{-13}	1.0×10^{-12}
δB	T	7.9×10^{-13}	7.0×10^{-13}	1.1×10^{-12}
$\delta B\sqrt{t_{\mathrm{cyc}}}$	$\mathrm{T}/\sqrt{\mathrm{Hz}}$	$\mathbf{3.5 \times 10^{-12}}$	$\mathbf{3.1 \times 10^{-12}}$	$\mathbf{4.7 \times 10^{-12}}$

Table 6.2.: Precision ($[\delta B]_A$, $[\delta B]_L$, δB) and sensitivity ($\delta B\sqrt{t_{\mathrm{cyc}}}$, bold) in the magnetic field estimation for the $f = 1$, $f = 2$ and comagnetometer readout. The estimations for $f = 1$ and $f = 2$ are computed via Eqs. 6.3, while for the comagnetometer we use $\delta B^{(12)} = \sqrt{\delta B^{(1)} + \delta B^{(2)}}$.

limited by probe photon shot-noise, and that it is close to an order of magnitude above the atomic spin projection-noise.

In the following we highlight a few natural extensions of the presented comagnetometer technique:[4]

(i) The remaining QZS can be cancelled using microwave dressing [149], to allow free choice of Larmor frequency and zero hyperfine relaxing collisions between $f = 2$ atoms.

(ii) A state-specific optical Zeeman shift can be applied to null γ_s and thus fully cancel background field noise.

(iii) A softer confining potential could reduce the rate of $1 \asymp 2$ collisions. If the mean trap frequency $\bar{\omega}$ gets reduced to 1/3 of its current value to give, the lifetime due to background gas collisions and $1 \asymp 2$ collisions become comparable $\tau^{\mathrm{bkg}} \sim \tau^{(12)} \sim 8\,\mathrm{s}$. The combined lifetime would be $\tau = (\tau^{\mathrm{bkg}} \cdot \tau^{(12)})/(\tau^{\mathrm{bkg}} + \tau^{(12)}) \sim 4\,\mathrm{s}$.

(iv) Cavity-assisted readout [150, 151, 152] could be used to reach the projection-noise level $\delta B \approx [\delta B]_A$, where the best precision is achieved for a hold time $t = 2\tau$.

(v) Faster loading could reduce the overhead between experimental cycles such that $t_{\mathrm{cyc}} \approx t$.

[4] Beyond mean-field dynamics that influence the precision of the comagnetometer δB are not captured in this list. Further investigations are required to quantify the interaction-based squeezing (anti-squeezing) [148] of the $f = 1$ and $f = 2$ spin components.

Combining these would give a sensitivity $\delta B^{(12)}\sqrt{t_{\mathrm{cyc}}} \approx 30\,\mathrm{fT}/\sqrt{\mathrm{Hz}}$ or $\delta E\sqrt{t_{\mathrm{cyc}}}/h \approx 210\,\mu\mathrm{Hz}/\sqrt{\mathrm{Hz}}$, where $\delta E\sqrt{t_{\mathrm{cyc}}}$ is the sensitivity on a hyperfine dependent energy splitting. In one week of running time, the statistical uncertainty of such a system would reach $\approx 40\,\mathrm{aT}$, comparable to state-of-the-art vapor- and gas-phase comagnetometers used in searches for physics beyond the standard model. For example, Lee *et al.* report 70 aT residual uncertainty after 1.5 week of acquisition in a recent search for axion-like particles with a ^{3}He-K comagnetometer [128]. These pseudo particles are postualted to mediate the spin-mass interaction between spin-polarized and unpolarized fermions. The interaction is described through a Yukawa-type potential of the form [153]:

$$V(\mathbf{r}) = \frac{\hbar^2 g_s g_p}{8\pi m_p}\hat{r}\cdot\hat{\sigma}_p\left(\frac{1}{r\lambda_\phi}+\frac{1}{r^2}\right)e^{-r/\lambda_\phi}\,, \tag{6.7}$$

where g_s and g_p are the scalar and pseudoscalar coupling constants, m_p the fermionic mass, $\hat{\sigma}_p$ the normalized spin expectation value and $\hat{r}$ the unit vector between both fermions. The interaction depends on the separation r between particles and on the characteristic axion interaction range $\lambda_\phi = \hbar/m_\phi c$, where m_ϕ is the associated axion mass. A SBEC comagnetometer would be able to probe length scales down to $\lambda_\phi \sim 10\,\mu\mathrm{m}$, about four orders of magnitude shorter than other comagnetometers and which corresponds to an axion mass of $m_\phi c^2 \sim 2\times10^{-3}\,\mathrm{eV}$. In searches for axion-like particles, these length scales are only weakly constrained by astrophysical arguments [154] and prior laboratory tests [155, 156].

Another potential application is phase-resolved spin amplification. Spin amplifiers use coherent collision processes in a BEC to achieve high-gain, quantum-noise limited amplification of small spin perturbations [45]. They are of particular interest in studies of quantum dynamics and non-classical state generation [46], but to date have not been able to resolve the magnetically sensitive azimuthal spin degree of freedom. This issue can be circumvented in a SBEC comagnetometer in which one hyperfine manifold tracks the magnetic field evolution while the other experiences parametric spin amplification. Preliminary experimental results on this topic are sown in Appendix D.

We close this chapter by mentioning the application to precision measurements of interhyperfine interactions in ultracold gases. The presented comagnetometer is highly sensitive to energy shifts between the $f = 1$ and $f = 2$ hyperfine manifolds, while suppressing any dependency on the external magnetic field. By leveraging this *effective* low magnetic noise environment, precision measurements on the scattering lengths rations $(a_1^{(12)} - a_2^{(12)})/(a_2^{(1)} - a_0^{(1)})$ and $(a_3^{(12)} - a_2^{(12)})/(a_2^{(1)} - a_0^{(1)})$ have been performed [53]. The measurement technique and obtained results are further discussed in Chapter 7.

7

Measurement of interhyperfine scattering lengths in ^{87}Rb

Studies on SBECs encompass a broad range of dynamics, from spin-mixing [146, 157, 36, 158] to spontaneous magnetic symmetry breaking [114, 159, 160], domain formation [22, 114, 161] and exotic topological spin excitations [162, 163]. These dynamics arise from the interplay between superfluidity and magnetism, which for a single, spin-f species and s-wave binary contact interactions are described by $2f+1$ parameters, the *intrahyperfine* scattering lengths. In the case of ^{87}Rb, these have been separately determined for the $f = 1$ and $f = 2$ ground-state manifolds [63, 35, 36]. *Interhyperfine* interactions are less well studied, but nonetheless play an important role in determining the miscibility of multiple BEC species [164, 165, 166], and have been used to produce spin-squeezing with its attendant entanglement, and Bell-type correlations [167, 168, 169, 170, 171]. For ^{87}Rb, the full set of inter-hyperfine spin interaction parameters has recently been measured [42].

In this chapter we report precision measurements on the ^{87}Rb interhyperfine $f = 1 \leftrightarrow f = 2$ scattering lengths, which have been published in [53]. We first give a brief overview of the prior work by Eto *et al.* [42] and proceed with our strategy and error estimation. Thereafter, we perform a calibration of the relevant classical parameters: the atom number N_A, the QZS $q^{(f)}$ and the mean trapping frequency $\bar{\omega}$. The measurement of the interhyperfine parameters estimates the interaction parameter ratios $g_2^{(12)}/g_1^{(1)}$ and $g_1^{(12)}/g_1^{(1)}$, from which the scattering lengths rations $(a_1^{(12)} - a_2^{(12)})/(a_2^{(1)} - a_0^{(1)})$ and $(a_3^{(12)} - a_2^{(12)})/(a_2^{(1)} - a_0^{(1)})$ are estimated. We close this chapter by comparing the obtained results to [42] and comment on possible extensions.

The following discussion references back to multiple sections of this thesis. We use the theoretical framework of Chapter 2 to describe the intra- and inter-hyperfine interaction in ^{87}Rb and to compute the resulting dynamics. As the experimental setup concerns, we leverage the hyperfine-selective Faraday probe and the comagnetometer technique described respectively in Section 5.3.4 and Chapter 6.

7.1. Prior work

The recent work by Eto *et al.* [42] constitutes the first measurement of the inter- hyperfine scattering lengths in ^{87}Rb. The authors present an original state preparation[1], which employs the differential Zeeman splitting between hyperfine manifolds to independently control the spin orientation in $f = 1$ and $f = 2$. It results in a SBEC in a superposition of $f = 1$ in a transversally oriented state $F_{\perp}^{(1)} = N_A^{(1)}$ and $f = 2$ in a longitudinally oriented state $F_z^{(2)} = -2N_A^{(2)}$.

For such a spin state, the interhyperfine interaction reduces to an effective linear Zeeman shift plus an effective quadratic Zeeman shift on the f=1 state, as described by Eq. (2.28) and Eq. (2.29). The corresponding phase shift of the $f = 1$ spin components is measured via a combination of Ramsey and spin-echo type sequence, from which the interhyperfine scattering lengths are obtained.

The SBEC ground state is significantly affected by the interhyperfine interaction. In fact, the results of Eto *et al.* indicate that in an equal $f = 1$, $f = 2$ ground-state mixture, the $f = 1$ component manifests a polar ground state at zero magnetic field [43] even though the $f = 1$ component alone is ferromagnetic [157].

7.2. Strategy and error estimates

The dynamics of a SBEC in a coherent superposition of $f = 1$ and $f = 2$ are driven by the distinct energy contributions in Eq. (2.30). For the purpose of this chapter, we include the QZS, the $f = 1$ and $f = 2$ intrahyperfine interaction energy and the $f = 1, 2$ interhyperfine interaction (neglecting hyperfine relaxation):

$$\begin{aligned} i\hbar\frac{\partial\xi_m^{(f)}}{\partial t} = \frac{\partial}{\partial\xi_m^{(f)*}}\Bigg[& \sum_f q^{(f)} F_z^{2(f)} \\ & + \frac{1}{2V_{\text{eff}}}\left(g_1^{(1)}\mathbf{F}^{(1)}\cdot\mathbf{F}^{(1)}\right) \\ & + \frac{1}{2V_{\text{eff}}}\left(g_1^{(2)}\mathbf{F}^{(2)}\cdot\mathbf{F}^{(2)} + g_2^{(2)}\left|A_0^{(2)}\right|^2\right) \\ & + \frac{1}{V_{\text{eff}}}\left(g_1^{(12)}F_z^{(1)}F_z^{(2)} + g_2^{(12)}\overline{P_1^{(12)}}\right)\Bigg]. \end{aligned} \tag{7.1}$$

The classical parameters to calibrate in Eq. (7.1) are the QZS $q^{(f)}$, the total atom number N_A and the mean trap frequency $\bar{\omega}$. The latter two are part of

[1] We closely follow the presented state preparation in Section 7.4.1.

the effective volume V_{eff} (see Appendix A) and scale the intra- and interhyperfine interaction dynamics. To derive this scaling we apply the $\partial/\partial\xi_m^{(f)*}$ derivative on the right-hand side of Eq. (7.1) and inspect the order the atom numbers $N_A^{(f)}$ appears:

$$i\hbar\frac{\partial\xi_m^{(f)}}{\partial t} = \Bigg\{ q^{(f)}\mathcal{O}(1) + \frac{1}{V_{\text{eff}}}\Bigg[\sum_{\mathcal{X}} g_{\mathcal{X}}^{(f)}\mathcal{O}(N_A^{(f)}) + \sum_{\mathcal{X}} g_{\mathcal{X}}^{(12)}(\mathcal{O}(N_A^{(2)})\delta_{f,1} + \mathcal{O}(N_A^{(1)})\delta_{f,2})\Bigg]\Bigg\}\xi_m^{(f)} \ . \quad (7.2)$$

Here, $g_{\mathcal{X}}^{(f)}$ and $g_{\mathcal{X}}^{(12)}$ are generic parameter for the intra- and interhyperfine interaction. We use $N_A^{(3-f)}$ for the *crossed* dependency in atom numbers introduced by the interhyperfine interaction, i.e $N_A^{(2)}$ for $f = 1$ and $N_A^{(1)}$ for $f = 2$. If we take $\mathcal{O}(N_A^{(f)}) = \mathcal{O}(N_A)$, we obtain that the mean density N_A/V_{eff} is a common pre-factor for the interaction dynamics. Expanding it in terms of the atom number and mean trap frequency we derive the scaling $N_A/V_{\text{eff}} \propto N_A^{2/5}\bar{\omega}^{6/5}$, which we will use in Section 7.3.

In the following we outline the strategy to perform the required classical calibrations and to estimate the interhyperfine interaction parameters :

(i) We calibrate $q^{(f)}$, N_A and $\bar{\omega}$ by comparing the dynamics of a $f = 1$ SBEC to simulations based on the tabulated intrahyperfine interaction parameters (see Table 2.3).

(ii) We estimate $g_2^{(12)}$ by preparing the SBEC in a superposition of $f = 1$ and $f = 2$ in which the transverse spin magnetisation of $f = 1$ is entirely driven by the $g_2^{(12)}$ term in Eq. (7.1). The dynamics are compared to simulations results by using the tabulated intrahyperfine interaction parameters, the previously calibrated classical parameters and $g_1^{(12)} = 0$. The only free fit parameter is $g_2^{(12)}$.

(iii) We estimate $g_1^{(12)}$ by preparing the SBEC in two different superpositions of $f = 1$ and $f = 2$. The two superpositions differ by their spin projection along the external magnetic field $F_z^{(f)}$, which leads to a slight shift in the Larmor precession frequencies of $f = 1$ and $f = 2$. Our comagnetometer technique resolves this tiny change in frequency and disentangles it from the external magnetic field noise. The data analysis uses the tabulated values for the intrahyperfine interaction, the estimated classical calibration parameters and measured $g_2^{(12)}$, while $g_1^{(12)}$ is left as a free fit parameter.

(iv) Based on the obtained interhyperfine interaction parameters, the scattering length differences $a_3^{(12)} - a_2^{(12)}$ and $a_1^{(12)} - a_2^{(12)}$ are obtained.

We use numerical error propagation to capture the different contributions to the uncertainties in our results. To this end, we numerically compute the derivatives of the form $\partial E_i/\partial x_j$, where E_i are the best estimates of our least-square fits (classical calibration values and interhyperfine couplings) and x_j are the input parameters of steps (i) to (iii) (atom numbers and intrahyperfine couplings). We assume uncorrelated error sources, such that for a given best estimate E_i its uncertainty reduces to $\delta E_i = \sqrt{(\delta f_i)^2 + \sum_j (\partial E_i/\partial x_j)^2 (\delta x_j)^2}$, which depends on δf_i, the statistical uncertainty of the underlying least-squares fit, and δx_j, the uncertainties in the input parameters .

The relative magnitudes of the contributions $(\partial E_i/\partial x_j)^2(\delta x_j)^2$ reveal that the uncertainty in the estimated interhyperfine couplings is predominantly inherited from the intrahyperfine interaction term $a_2^{(1)} - a_0^{(1)}$, a quantity for which theory and experiment are at present discrepant [63, 35, 36]. At the scale of our experimental precision, the estimated interhyperfine couplings depend linearly on $a_2^{(1)} - a_0^{(1)}$. For this reason, we report the ratios $g_1^{(12)}/g_1^{(1)}$, $g_2^{(12)}/g_1^{(1)}$, $(a_3^{(12)} - a_2^{(12)})/(a_2^{(1)} - a_0^{(1)})$ and $(a_1^{(12)} - a_2^{(12)})/(a_2^{(1)} - a_0^{(1)})$, where the numerator is the fit result and the denominator is a fixed parameter. These ratios, unlike the fit result itself, are insensitive to the value of $a_2^{(1)} - a_0^{(1)}$, again at the level of precision of the experimental results. For the estimated trap frequency, we report its bare value $\bar{\omega}$ as well as $\bar{\omega}|a_2^{(1)} - a_0^{(1)}|^{5/6}$, which does not depend on the intrahyperfine interaction.

While systematic errors in the atom number readout are calibrated, a remaining uncertainty arises from experimental atom numbers fluctuations and drifts. Atom numbers and their fluctuations were estimated by repeated trap loading, state preparation, and destructive absorption imaging prior to acquiring data runs such as the one reported in Fig. 7.1. Despite this, a significant uncertainty accrues due to drifts in the ^{87}Rb background pressure. We account for this with a systematic uncertainty of $\pm 10\%$ rms deviation around the measured atom numbers. The value $\pm 10\%$ describes the observed drifts from run to run, as well as the observed fluctuations of $f = 2$ population shown in Fig. 7.2.

7.3. Calibration of trap conditions

For a precise determination of the inter-hyperfine scattering parameters, we require best-estimate values and uncertainties for the QZS $q^{(f)}$, the mean trapping frequency $\bar{\omega}$ and the atom number N_A. Precise knowledge of the LZS is not required, because the signals are either insensitive to the Larmor precession angles

$\theta^{(1)}$ and $\theta^{(2)}$, or are sensitive only to their sum, to which the net LZS contribution is small. The LZS must, however, be large enough that the RWA is valid.

There are multiple sources for systematic uncertainties in the above mentioned parameters. The QZS is potentially affected by tensorial light shifts caused by the intense trapping beams [104]. The trapping frequency depends on power levels and precise alignment of the crossed dipole traps, and is typically calibrated *in situ*. The inferred atom number is sensitive to the magnification and polarization of the absorption imaging light, as well as to the absorption cross section. For an absolute calibration of the measured atom numbers, schemes based on projection noise scaling in SBECs have been reported [68, 172].

We note that $q^{(f)}$, $\bar{\omega}$ and N_A enter into $f = 1$ spin dynamics and $f = 1, 2$ interhyperfine spin dynamics in the same way, which provides an opportunity to calibrate the net effect of these variables with the intrahyperfine spin dynamics as reference. In particular, the trapping frequency $\bar{\omega}$ and atom number N_A only contribute through the mean density $N/V_{\text{eff}} \propto N^{2/5}\bar{\omega}^{6/5}$ (see Eq. (7.2) and below). In this way, the above-described experimental sources of uncertainty in $\bar{\omega}$ and in N_A can be combined in a single parameter, which we choose to be the effective trapping frequency $\bar{\omega}_{\text{eff}}$. In the following calibration, we take N_A to be the atom number as measured by absorption imaging or Faraday rotation, and obtain $q^{(f)}$ and the effective trap frequency $\bar{\omega}_{\text{eff}}$ from a fit to measured $f = 1$ intra-hyperfine spin dynamics. This results in a calibration of the QZS and the mean density N/V_{eff}, now written in terms of measured N_A and estimated $\bar{\omega}_{\text{eff}}$.

To this end, we first create a $f = 1$ SBEC in the non-magnetic $\xi/\sqrt{N_A} = (0, 1, 0)^T \oplus \mathbf{0}_5^T$ state, in the presence of a constant field B =119.6 mG, giving $N_A = 79(4) \times 10^3$ atoms as measured by destructive absorption imaging. A rf $\pi/4$ pulse rotates the spin state to $\xi^{(1)}/\sqrt{N_A} = (1/2, i/\sqrt{2}, 1/2)^T$. After a variable hold time, Faraday rotation signals are acquired and fitted with Eqs. (5.11) to find the transverse magnetization $F_\perp^{(f)}$. Results are shown in Fig. 7.1 and exhibit the expected oscillation of $F_\perp^{(f)}$ produced by competition between the QZS and the ferromagnetic interaction. These $F_\perp^{(f)}$ values are compared to SMA mean-field simulations as per Section 2.4, with the $q^{(1)}$ and $\bar{\omega}_{\text{eff}}$ as free fit parameters. We find $\bar{\omega}_{\text{eff}} = 2\pi \times 90(9)$ Hz and $q^{(1)}/h = 0.89(10)$ Hz.

The $\bar{\omega}_{\text{eff}}$ value is consistent with independent measurements of trap sloshing frequencies. The obtained value for $q^{(1)}/h$ is in agreement with the theoretically expected $(p^{(1)}/h)^2/\nu_{\text{hfs}} = 1.03$ Hz, where $\nu_{\text{hfs}} = 6.8$ GHz is the $f = 1, 2$ hyperfine splitting. We note that, to the precision of this work, the hyperfine manifolds feature opposite QZS, so that $q^{(2)}/h = -0.89(10)$ Hz.

The estimated value of $\bar{\omega}_{\text{eff}}$ depends on the ferromagnetic interaction coefficient $g_1^{(1)}$ and thus on $a_2^{(1)} - a_0^{(1)}$. As mentioned in Section 7.2, this dependence is undesirable and our preferred quantity to report is the rescaled mean trapping

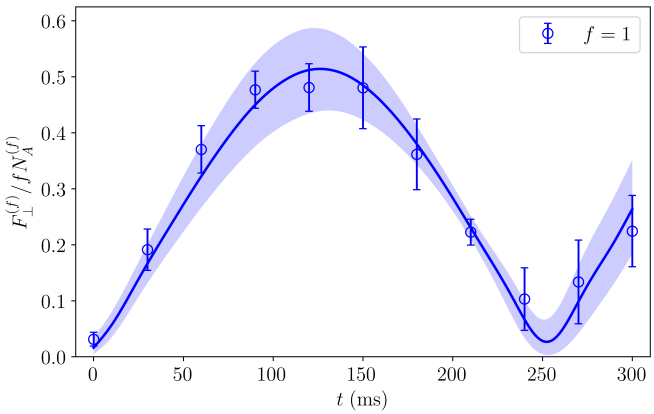

Figure 7.1.: Time evolution of the transverse magnetization in $f = 1$, starting from a fully aligned ($F_\perp^{(1)} = 0$) state $\xi^{(1)}/\sqrt{N_A} = (1/2, i/\sqrt{2}, 1/2)^T$. The dynamics are governed by the competition between the QZS and the ferromagnetic interaction. Blue circles show the mean observed transverse magnetization $F_\perp^{(1)}$ after a variable hold time t. Error bars are the standard deviation over 4 experimental repetitions. The solid line and coloured area represent the median and 90% confidence interval of the theoretical model. The Faraday probe detuning is $\Delta^{(10')}/2\pi = -570\,\mathrm{MHz}$ (see Table 5.4).

frequency $\bar{\omega}_{\mathrm{eff}}|a_2^{(1)} - a_0^{(1)}|^{5/6} = 1.63(12) \times 10^{-6}\,\mathrm{s}^{-1}\mathrm{m}^{5/6}$, which does not depend on the intrahyperfine interaction.

7.4. Measurement of interhyperfine interaction parameters

In this section we use the incremental strategy described in Section 7.2 to estimate the interhyperfine interaction parameters $g_2^{(12)}$ and $g_1^{(12)}$. For an intuitive picture on the interhyperfine dynamics and the spin states used in the following discussions, please refer to Section 2.3.

7.4.1. Interaction parameter $g_2^{(12)}$

To measure $g_2^{(12)}$, we first prepare the state

$$\frac{\xi}{\sqrt{N_A}} = \begin{pmatrix} \frac{1}{2\sqrt{2}} \\ \frac{i}{2} \\ \frac{1}{2\sqrt{2}} \end{pmatrix} \oplus \begin{pmatrix} 0 \\ 0 \\ 0 \\ 0 \\ \frac{1}{\sqrt{2}} \end{pmatrix}, \tag{7.3}$$

which describes and equal superposition of $f = 1$ in an aligned ($F_\perp^{(1)} = 0$) state and $f = 2$ in a $-\mathbf{z}$ oriented state. After a variable wait time the $f = 1$ transverse magnetization $F_\perp^{(1)}$ is measured by Faraday rotation. Note that the $f = 2$ state is unchanged by the evolution and readout of $f = 1$. After measuring the $f = 1$ manifold, a rf $\pi/2$ pulse rotates the stretched $f = 2$ state into the transverse plane and $F_\perp^{(2)}$ is measured by Faraday rotation. This provides a measure of the atom number $N = 2N^{(2)} = 101(9) \times 10^3$ atoms. The procedure is described in detail in Appendix E.

In Fig. 7.2 the measured transverse magnetization in $f = 1$ and $f = 2$ are shown as a function of the hold time in the trap. Note that the frequency and amplitude of the modulation nearly double those in Fig. 7.1, where only the $f = 1$ manifold is populated. This enhancement is caused by the effective QZS induced by the $g_2^{(12)}$ term of the interhyperfine interaction (see Eq. (2.29) and surrounding discussion). By fitting the expected SMA mean-field evolution we obtain $g_2^{(12)}/g_1^{(1)} = -6.4(6)$. For this fit, we used the calibrated values for $q^{(f)}$ and $\bar{\omega}_{\text{eff}}$ and neglect the $g_1^{(12)}$ term in Eq. (7.1), which does not contribute to the modulation in $F_\perp^{(1)}$.

7.4.2. Interaction parameter $g_1^{(12)}$

We measure $g_1^{(12)}$ by estimating the change in the effective LZS (see Eq. (2.28) and surrounding discussion) for the following two states:

$$\frac{\xi_A}{\sqrt{N_A}} = \hat{R}_\pi^{(1)}[\pi/6] \begin{pmatrix} \frac{1}{\sqrt{2}} \\ 0 \\ 0 \end{pmatrix} \oplus \hat{R}_0^{(2)}[\pi/6] \begin{pmatrix} \frac{1}{\sqrt{2}} \\ 0 \\ 0 \\ 0 \\ 0 \end{pmatrix}, \tag{7.4a}$$

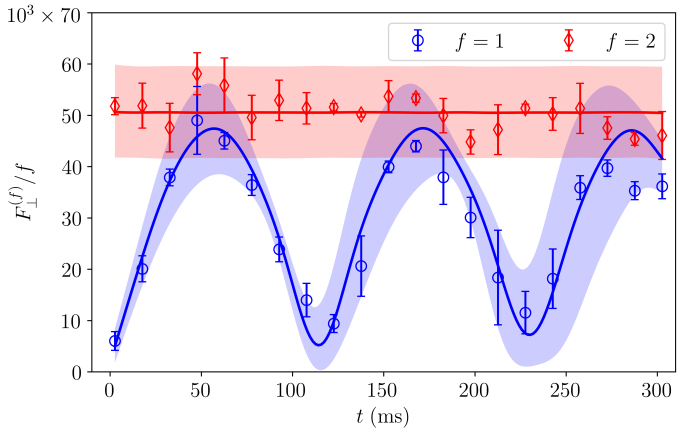

Figure 7.2.: Dynamical evolution for the initial state in Eq. (7.3) and under a magnetic field of 119.6 mG. Blue circles and red diamonds, are the mean experimental transverse magnetization in $f = 1$ and $f = 2$, respectively. Error bars are the standard deviation over 4 experimental repetitions. The solid lines are the median of the theoretical mean-field evolution for $g_2^{(12)}/g_1^{(1)} = -6.4$, while shaded areas represent the 90% confidence intervals. The Faraday probe detunings are $\Delta^{(10')}/2\pi = -270\,\mathrm{MHz}$ and $\Delta^{(23')}/2\pi = 360\,\mathrm{MHz}$ (see Table 5.4).

$$\frac{\xi_B}{\sqrt{N_A}} = \hat{R}_\pi^{(1)}[\pi/6] \begin{pmatrix} 0 \\ 0 \\ \frac{1}{\sqrt{2}} \end{pmatrix} \oplus \hat{R}_0^{(2)}[\pi/6] \begin{pmatrix} 0 \\ 0 \\ 0 \\ 0 \\ \frac{1}{\sqrt{2}} \end{pmatrix}, \tag{7.4b}$$

where $\hat{R}_\pi^{(1)}[\pi/6]$ and $\hat{R}_0^{(2)}[\pi/6]$ rotate the $f = 1$ and $f = 2$ states by $\pi/6$ rad around $-\mathbf{x}$ and $+\mathbf{x}$, respectively. The rotation angle is a compromise between a strong spin component parallel to the external magnetic field (required for a $g_1^{(12)} F_z^{(1)} F_z^{(2)}$ contribution in Eq. (7.1)) and a significant transverse magnetization (required for Faraday readout). After a variable wait time, the $f = 1$ and $f = 2$ precession angles are measured by Faraday rotation. A detailed description is given in Appendix E.

For an initial state $X \in \{A, B\}$ the comagnetometer signal $\theta_X^{(12)} \equiv \theta_X^{(1)} + \theta_X^{(2)}$ contains contributions from the $-2\gamma_s = 2\pi \times -334\,\mathrm{Hz}$ differential LZS between $f = 1$ and $f = 2$, the QZS and the spin-dependent inter-hyperfine interaction,

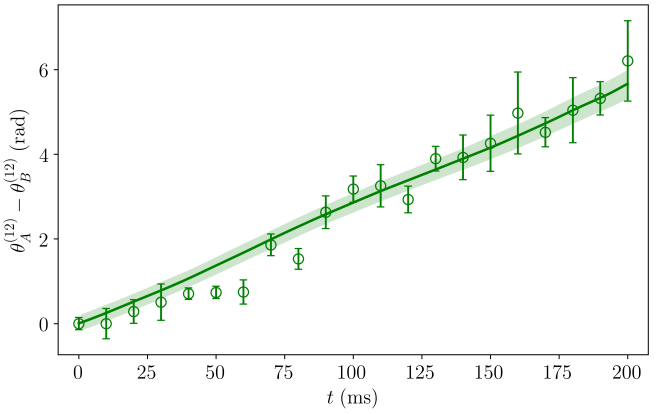

Figure 7.3.: Phase evolution of the difference in the comagnetometer readouts between state preparations A and B. Circles show the experimental mean values and the error bars represent one standard deviation. The solid line and shaded area are the mean and standard deviation of the theoretical phase evolution for $g_2^{(12)}/g_1^{(1)} = -6.4$ and $g_1^{(12)}/g_1^{(1)} = -1.27$. Atom numbers are estimated by destructive absorption imaging before the first run of experimental sequence A and B, yielding $N_A = 88(3) \times 10^3$ and $N_A = 96(3) \times 10^3$, respectively. The Faraday probe detunings are $\Delta^{(10')}/2\pi = -270\,\mathrm{MHz}$ and $\Delta^{(23')}/2\pi = 360\,\mathrm{MHz}$ (see Table 5.4).

i.e., the $g_1^{(12)}$ and $g_2^{(12)}$ contributions. We analyze the difference in comagnetometer readouts $\theta_A^{(12)} - \theta_B^{(12)}$, in which also the differential LZS contribution cancels. The QZS is known from the calibration of Section 7.3. The results are shown in Fig. 7.3, where the experimental data are fitted to SMA mean-field simulations in which $g_1^{(12)}$ is a free fit parameter whereas $g_2^{(12)}$ is fixed at the value found in Section 7.4.1. We obtain $g_1^{(12)}/g_1^{(1)} = -1.27(15)$.

7.5. Comparison with prior work and extensions

Using Eq. (2.20g) and Eq. (2.20h) for the above values of $g_1^{(12)}$ and $g_2^{(12)}$, we find $(a_3^{(12)} - a_2^{(12)})/(a_2^{(1)} - a_0^{(1)}) = -1.27(15)$ and $(a_1^{(12)} - a_2^{(12)})/(a_2^{(1)} - a_0^{(1)}) = -1.31(13)$, with relative uncertainties of 12% and 10%, respectively. As noted

above, these ratios are insensitive to the exact value of $a_2^{(1)} - a_0^{(1)}$, which serves as an input parameter in the modelling and fits. Applying the same scaling to the values reported by Eto *et al.* [42] yields $(a_3^{(12)} - a_2^{(12)})/(a_2^{(1)} - a_0^{(1)}) = -1.8(5)$ and $(a_1^{(12)} - a_2^{(12)})/(a_2^{(1)} - a_0^{(1)}) = -2.2(4)$. These differ by 1σ and 2σ combined uncertainty from the result presented here.

Our results are complementary to Ramsey spectroscopy measurements used to characterise mean-field shifts in the ^{87}Rb clock transition [173, 174]. The SBEC dynamics of this chapter resolve the spin-dependent interhyperfine couplings $g_1^{(12)}$ and $g_2^{(12)}$ but are insensitive to the spin-independent coupling $g_0^{(12)}$ (see Table 2.1 and discussion above it). The situation is reversed in a ^{87}Rb SBEC clock, which is typically described through an effective two level system and three interaction coefficients that describe the $|1,0\rangle \asymp |1,0\rangle$ and $|2,0\rangle \asymp |2,0\rangle$ intrahyperfine interaction strengths, and the $|1,0\rangle \asymp |2,0\rangle$ interhyperfine interaction strength. These coefficients are linear combinations of the $g_{\mathcal{C}}^{(\mathcal{F})}$ that appear in Eqs. (2.20). The strongest contributions are from the spin-independent couplings $g_0^{(1)}$, $g_0^{(2)}$ and $g_0^{(12)}$.

Our accuracy is presently limited by uncertainty in the SBEC atom numbers, which reflect loading fluctuations and atom loss during the experiment. Active control schemes can stabilize the atom numbers of cold atomic ensembles below shot noise by using dispersive probing [175]. Applied to the current experiment, such stabilization is foreseen to reduce the relative uncertainties in the results below $\sim$0.3 %.

8

Conclusions and outlook

This thesis demonstrates the first realization of a comagnetometer in the ultracold regime. By engineering the spin state of a ^{87}Rb spinor Bose-Einstein condensate (SBEC) we achieve paired magnetometers implemented on separate hyperfine manifolds but sharing the same spatial wavefunction. At low magnetic fields, the spin-dependent contact interaction energy overcomes the quadratic Zeeman shift, which suppresses exothermic hyperfine relaxing collisions and yields $\sim 1\,\mathrm{s}$ long coherence times. Under this configuration we demonstrate a $44.0(8)\,\mathrm{dB}$ attenuation in the common-mode magnetic field noise. Our comagnetometer operates on $\sim 10\,\mu\mathrm{m}$ length scales, about four order of magnitudes below competing techniques, and is a promising platform for studying axion-mediated interactions at those length scales.

We have applied our SBEC comagnetometer to estimate the interhyperfine interaction in ^{87}Rb, which is a weak influence in comparison to typical energy fluctuations in the linear Zeeman splitting and magnetic field noise. Prior to these measurements, a thorough calibration of the trap conditions and mean density was performed, based on the comparison between observed SBEC dynamics and meanfield simulations. The uncertainty in the here-estimated interhyperfine scattering lengths is reduced by more than a factor three with respect to prior experimental works.

The enabling experimental developments can be separated into advances in the magnetic control of the atomic ensembles and advances in the optical manipulation and readout. In the first case, we highlight the implementation of radiofrequency and microwave driving techniques, as well as the development of a real-time radiofrequency source. In the second case, we include the digitization of the laser locks and the new hyperfine-selective Faraday probing.

The outlook of this thesis is twofold. On the physical side, we discuss a further applications of the SBEC comagnetometer and next steps on the phase resolving parametric spin amplifier. As regards possible technical improvements, we comment on a state preparation that cancels the differential Zeeman splitting between $f = 1$ and $f = 2$ manifolds and introduce a crosstalk mitigation technique for their readout.

Further applications on SBEC comagnetometry[1]

A potential application is atomic rf magnetometry. Recently reported rf magnetometers in cold atoms [176] are only sensitive to a single rf polarization. This limitation is resolved within our dual-magnetometer configuration, where the opposite gyromagnetic ratios of $f = 1$ and $f = 2$ result in a sensitivity to both σ^- and σ^+ polarization components. Hence, the full information on the transverse driving field can be retrieved.

Another application is an atomic gyroscope. Our SBEC comagnetometer cancels the common mode magnetic evolution, while rotations of the laboratory reference frame doubly influence its readout $\theta^{(12)} = \theta^{(1)} + \theta^{(12)}$. In fact, the comagnetometer readout can be used to measure rotations of the laboratory reference frame and disentangle them from spin rotations caused by the external magnetic fields.

Regarding phase-resolved parametric amplification, the preliminary results in Appendix D did not explore the parameter space of the parametric amplifier. Klempt *et al.* demonstrated that the instability, or equivalently gain of the amplifier, can be tuned via the QZS and the spin population in the pump field $\rho_0^{(2)} N_A$. For instance, by increasing the relative population in the pump field to $\rho_0^{(2)} = 0.75$ and moving the magnetic field to $B_z = 420\,\mathrm{mG}$ we expect an enhancement in the amplifier gain of a factor 2.5. A thorough calibration of these parameters and the estimation of the linear amplification regime remain open.

Technical improvements

The SBEC comagnetometer is constrained to work at low magnetic fields and in a fully oriented configuration ($F_\perp^{(f)} = f N_A$) to avoid hyperfine relaxing collisions. These limitation are not present for less dense and non-condensed ensembles. In this case, more *exotic* spin configuration can be used, which significantly enhance the performance of the comagnetometer. For example, the comagnetomer can be prepared in state $\xi = (0, \frac{1}{2}, \frac{1}{2})^T \oplus (\frac{1}{2}, \frac{1}{2}, 0, 0, 0)^T$, which has two fundamental advantages. First, it does not suffer from orientation-to-alignment conversion and has a constant transverse magnetisation. Second, the readout signal evolves like $\theta^{(12)} = \theta_0^{(12)} + (-2\gamma_s B + 4\beta_0 B^2)t$ (see definitions in Section 2.2) and features a magnetically insensitive point at $B \approx 4.84\,\mathrm{G}$.

On behalf of the hyperfine-selective readout, a fundamental drawback is the residual crosstalks between the $f = 1$ and $f = 2$ probes. The situation is analogous to the crosstalks in multi-axis magnetic field and inertial sensors, which are

[1] The extensions to our SBEC comagnetometer for studying axion-like particles are detailed in Section 6.5.

typically compensated via a linear transformation [177]. We propose to follow the same approach and introduce a linear description for our Faraday readout. To this end, rather than directly reporting the transverse spin amplitude $F_{\perp}^{(f)}$ and azimuth angle $\theta_0^{(f)}$ (see fit model in Eqs. (5.11)), it is more convenient to use the corresponding in-phase $I^{(f)}$ and in-quadrature $Q^{(f)}$ components:

$$I^{(f)} = F_{\perp}^{(f)} \cos(\theta_0^{(f)}) \,, \tag{8.1a}$$

$$Q^{(f)} = F_{\perp}^{(f)} \sin(\theta_0^{(f)}) \,. \tag{8.1b}$$

In terms of these, the linear crosstalk compensation can be described via a 4×4 matrix transformation:

$$\begin{pmatrix} \mathcal{I}^{(1)} \\ \mathcal{Q}^{(1)} \\ \mathcal{I}^{(2)} \\ \mathcal{Q}^{(2)} \end{pmatrix} = \begin{pmatrix} C_{11} & C_{12} & C_{13} & C_{14} \\ C_{21} & C_{22} & C_{23} & C_{24} \\ C_{31} & C_{32} & C_{33} & C_{34} \\ C_{41} & C_{42} & C_{43} & C_{44} \end{pmatrix} \begin{pmatrix} I^{(1)} \\ Q^{(1)} \\ I^{(2)} \\ Q^{(2)} \end{pmatrix} \tag{8.2}$$

where $\hat{C}$ is the compensation matrix that connects the measured ($I^{(f)}$ and $Q^{(f)}$) and compensated ($\mathcal{I}^{(f)}$ and $\mathcal{Q}^{(f)}$) components . The compensation matrix needs to be calibrated but it is experimentally easier to determine its inverse $\hat{C}^{-1}$. To this end, four separate state preparations and Faraday readouts are required. We outline the process below:

(i) Prepare the SBEC in state $\xi/\sqrt{N_A} = \hat{R}_0^{(1)}[\pi/2](1,0,0)^T \oplus \mathbf{0}_5^T$ and perform a Faraday measurement on both hyperfine manifolds. The measured components is used to construct the first column of $\hat{C}^{-1}$:

$$\begin{pmatrix} C_{11}^{-1} \\ C_{12}^{-1} \\ C_{13}^{-1} \\ C_{14}^{-1} \end{pmatrix} = \frac{1}{\sqrt{[I^{(1)}]^2 + [Q^{(1)}]^2}} \begin{pmatrix} I^{(1)} \\ Q^{(2)} \\ I^{(2)} \\ Q^{(2)} \end{pmatrix} \tag{8.3}$$

(ii) Prepare the SBEC in state $\xi/\sqrt{N_A} = \hat{R}_{\pi/2}^{(1)}[\pi/2](1,0,0)^T \oplus \mathbf{0}_5^T$ and perform a simultaneous Faraday measurement on both hyperfine manifolds. The measured $I^{(f)}$ and $Q^{(f)}$ components are used to construct the second column of $\hat{C}^{-1}$:

$$\begin{pmatrix} C_{21}^{-1} \\ C_{22}^{-1} \\ C_{23}^{-1} \\ C_{24}^{-1} \end{pmatrix} = \frac{1}{\sqrt{[I^{(1)}]^2 + [Q^{(1)}]^2}} \begin{pmatrix} I^{(1)} \\ Q^{(2)} \\ I^{(2)} \\ Q^{(2)} \end{pmatrix} \tag{8.4}$$

(iii) Prepare the SBEC in state $\xi/\sqrt{N_A} = \mathbf{0}_3^T \oplus \hat{R}_0^{(2)}[\pi/2](1,0,0,0,0)^T$ and perform a simultaneous Faraday measurement on both hyperfine manifolds. The measured $I^{(f)}$ and $Q^{(f)}$ components are used to construct the third column of $\hat{C}^{-1}$:

$$\begin{pmatrix} C_{31}^{-1} \\ C_{32}^{-1} \\ C_{33}^{-1} \\ C_{34}^{-1} \end{pmatrix} = \frac{1}{\sqrt{[I^{(2)}]^2 + [Q^{(2)}]^2}} \begin{pmatrix} I^{(1)} \\ Q^{(2)} \\ I^{(2)} \\ Q^{(2)} \end{pmatrix} \tag{8.5}$$

(iv) Prepare the SBEC in state $\xi/\sqrt{N_A} = \mathbf{0}_3^T \oplus \hat{R}_{\pi/2}^{(2)}[\pi/2](1,0,0,0,0)^T$ and perform a simultaneous Faraday measurement on both hyperfine manifolds. The measured $I^{(f)}$ and $Q^{(f)}$ components are used to construct the fourth column of $\hat{C}^{-1}$:

$$\begin{pmatrix} C_{41}^{-1} \\ C_{42}^{-1} \\ C_{43}^{-1} \\ C_{44}^{-1} \end{pmatrix} = \frac{1}{\sqrt{[I^{(2)}]^2 + [Q^{(2)}]^2}} \begin{pmatrix} I^{(1)} \\ Q^{(2)} \\ I^{(2)} \\ Q^{(2)} \end{pmatrix} \tag{8.6}$$

After completing the measurements, $\hat{C}^{-1}$ is numerically inverted to obtain $\hat{C}$, which now can be applied to compensate the raw Faraday readouts as described in Eq. (8.2). Note that the calibration matrix needs to be estimated again whenever the Larmor precession frequencies or the delay between the $f = 1$ and $f = 2$ Faraday pulses are modified.

Appendices

A

Effective volume for a Thomas-Fermi density distribution

In this thesis, the spatial dependence of the SBEC has been *integrated out* via the Single Mode Approximation (SMA), as explained in Chapter 2. The resulting vectorial order parameter is spatially independent, corresponding to a $\mathbb{C}^N$ vector, namely the spin amplitudes. However, the spatial density distribution is required for computing the effective volume, which is a prefactor of the contact-interaction energy under the SMA.

In the following we compute the density distribution and effective volume for a harmonically trapped SBEC. To estimate the density distribution of the SBEC, we solve the time-independent Gross-Pitaevskii equation [24]

$$\left(-\frac{\hbar^2\nabla^2}{2M} + V(\mathbf{r})\right)\Psi_{\mathrm{SMA}}(\mathbf{r}) + g_0 N_A \left|\Psi_{\mathrm{SMA}}(\mathbf{r})\right|^2 = \mu\Psi_{\mathrm{SMA}}(\mathbf{r}) \,, \tag{A.1}$$

where the satisfying eigenvalues and eigenfunctions are the chemical potential μ and the spatial wavefunction $\Psi_{\mathrm{SMA}}(\mathbf{r})$, respectively. The spin independent contact interaction is g_0, which we take to be $g_0^{(1)}$ (see Eq. (2.20a)). The time-independent Gross-Pitaevskii equation simplifies for BECs significantly larger than the density healing length, where the kinetic contribution to the total energy is neglected. This is known as the Thomas-Fermi approximation [178, 179, 180] and the resulting density reads:

$$N_A|\Psi_{\mathrm{SMA}}(\mathbf{r})|^2 = \begin{cases} \frac{\mu - V(\mathbf{r})}{g_0^{(1)}} & \text{when } V(\mathbf{r}) < \mu \\ 0 & \text{otherwise} \end{cases} \tag{A.2}$$

where $V(\mathbf{r})$ is the underlying spin-independent trapping potential. The chemical potential μ is obtained by normalizing the spatial wave function as defined in Eq. (2.6a).

For the density profile in Eq. (A.2) and a harmonic trapping potential with mean trapping frequency $\bar{\omega}$, the effective volume $V_{\mathrm{eff}} = (\int dr^3 |\Psi_{\mathrm{SMA}}(\mathbf{r})|^4)^{-1}$ be-

comes:

$$V_{\text{eff}} = \frac{14}{15}\pi \bar{r}^3_{\text{TF}} \,, \tag{A.3}$$

$$\bar{r}_{\text{TF}} = \left(\frac{15}{4\pi} \frac{g_0^{(1)} N_A}{M\bar{\omega}^2} \right)^{1/5} \,, \tag{A.4}$$

where $\bar{r}_{\text{TF}}$ is the mean Thomas-Fermi radius.

B

Real-time rf source (code examples)

In the following sections we describe a subset of the programming examples given in the repository [110]. Please refer to the same repository for the documentation and source code of the Python API.

We structure the discussion as follows. We first show a code snipped for the initialization and execution commands which are common to all examples. After, the code for the distinct examples are presented, including the corresponding oscilloscope traces.

Initialization and execution

The code snippet B.1 is a general placeholder for the following examples. It first loads the required libraries, sets up the serial communication and creates an instance of the Python API. After, the example (i.e. sequence) is constructed and executed.

```
from __future__ import division
import serial
import time
import sys
sys.path.append('..')
import AD9958
####################################################
# Setting up serial communication
####################################################
RF_COM_PORT="COM7"
try:
  serRF   #Check if serial port is already open
except NameError:
  serRF=serial.Serial(RF_COM_PORT, 9600, timeout=0.2)
  print "Starting RF serial port."
  time.sleep(5) #Waiting for microcontroller to start
####################################################
#Initialization of AD9958 object & function stack
####################################################
print "Initialize AD9958 object."
```

```
RF=AD9958.AD9958_class(ser=serRF,ref_clk=25e6,PLL_multiplier=20,
    chipkit_clk=80e6)
RF.clearStack()
##################################################
# Start sequence (function stack)
##################################################
#
# Include code examples here
#
##################################################
# End sequence (function stack)
##################################################
print RF.checkLenRequest()
print RF.checkLenStack()
RF.runStack()
```

Code B.1: Common placeholder for the following code examples. It carries out the initialization tasks and the execution of the programmed sequence.

Single tone mode

In single tone mode, both channels of the AD9958 are configured to output a sinusoidal waveform with a constant amplitude, frequency and phase offset.

Single tone mode in continuous operation

This example corresponds to a typical mw manipulation, where the rf source is continuously operating and provides a gating (trigger) signal for the mw chain. To this end, the synthesized rf field and the triggerOut signal are fed into the rf and trigger ports described in Fig. 5.5.

In Code B.2 we program the rf source to operate in single tone mode. Both channels (ch0 and ch1) operate at 1 MHz, their amplitudesare set to 1[1] and the phase offset of ch0 and ch1 are set to 0° and 90°, respectively. Note that ch0 and ch1 are configured separately and that the internal phase accumulator of ch0 starts to run after the first call of *setFreq()*, while for ch1 this happens later, at the second call of *setFreq()*. As a result, their relative phase differers from the programmed 90°. For this reason, after configuring both channels we call *clearPhaseAccumulator()*. This clears the internal phase accumulators, sets them to the corresponding initial phase offset and simultaneously restarts their operation. We include a triggered execution, where after receiving an external triggerIn signal, triggerOut is enabled for 20 µs. The corresponding waveforms are shown in Fig. B.1.

```
1  ##################################################
2  # Start sequence (function stack)
3  ##################################################
4  print "Programming sequence."
5  RF.reset()
6  RF.resetTimer()
7  RF.configureSysClock()
8
9  #Channel 0 and 1
10 RF.setEnabledChannels(1,1) #Enables communication to ch0 and ch1
11 RF.setDACFullScale()
12 RF.setSingleToneMode()
13
14 #Channel 0
15 RF.setEnabledChannels(1,0)  #Enables communication only to ch0
16 RF.setFreq(0,1e6)
17 RF.setAmplitude(0,1)
18 RF.setPhase(0,0) #0 deg
19
20 #Channel 1
```

[1]The API uses relative units to for the amplitude, i.e. 1 corresponds to the full-scale output of the AD9958.

```
RF.setEnabledChannels(0,1) #Enables communication only to ch1
RF.setFreq(0,1e6)
RF.setAmplitude(0,1)
RF.setPhase(0,90) #90 deg

#Clearing phase accumulator
RF.setEnabledChannels(1,1)
RF.clearPhaseAccumulator()

#Triggered execution
RF.waitTriggerIn() #Waits for rising edge
RF.setTriggerOut(1)
RF.delayTimer(20e-6)
RF.setTriggerOut(0)
##################################################
# End sequence (function stack)
##################################################
```

Code B.2: Single tone mode in continuous operation. The full example is available in [110] under *Examples/singleTone.py*.

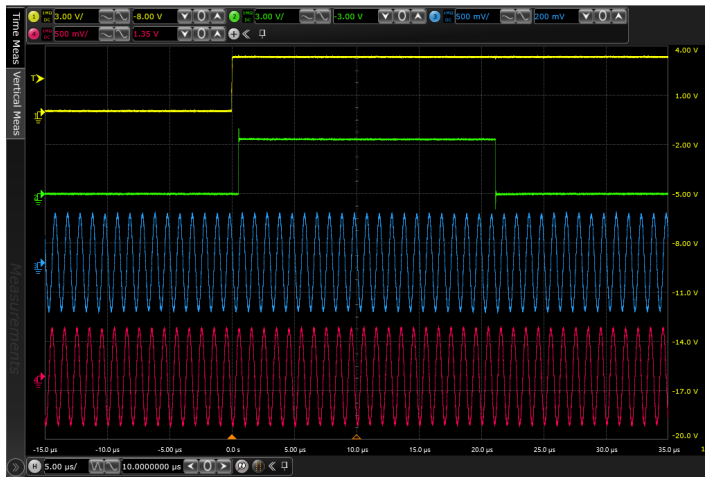

Figure B.1.: Oscilloscope screen capture for the rf driver sequence in Code B.2. The traces are: triggerIn (yellow), triggerOut (green), ch0 (blue) and ch1 (red).

Single tone mode with automatic amplitude ramp-up and ramp-down

This example corresponds to a typical rf manipulations, where the synthesized waveform is directly fed into the rf port of Fig. 5.3

In Code B.3 we perform rf-pulse generation using the the automatic ramp-up and ramp-down feature of the AD9958. This mode avoids abrupt changes in the output of the DDS, typically related to switching the amplitude from 0 (OFF) to its operational point (ON), and vice versa. To this end, the operational amplitudes are configured in the corresponding internal registers but their actual states (ON/OFF) are controlled separately via the profile pins P2 and P3, respectively. When a change in a profile pin is detected, the AD9958 initiates an automatic rising (falling) linear amplitude ramp until the ON (OFF) state is reached on the corresponding channel. The step size and clocking rate of the automatic amplitude ramp are configurable through the *enableAutomaticRURD()* method of the Python API. In this example, only ch0 is active and its full-scale automatic amplitude ramp time is 4.1 µs. As before, the central part of this example uses triggered execution. After a triggerIn signal has been received, the rf pulse generation is started by setting ch0 to the ON state. The pulse is set back to the OFF state 20 µs later. In this case, the trigger out port is used for monitoring purposes only. The corresponding waveforms are shown in Fig. B.2.

```
1  ###################################
2  # Start sequence (function stack)
3  ###################################
4  print "Programming sequence."
5  RF.reset()
6  RF.resetTimer()
7  RF.configureSysClock()
8
9  #Channel 0 and 1
10 RF.setEnabledChannels(1,1)
11 RF.setDACFullScale()
12 RF.setSingleToneMode()
13 RF.setAmplitude(0,0)
14
15 #Channel 0
16 RF.setEnabledChannels(1,0)
17 RF.enableAutomaticRURD(0,1)
18 RF.setAmplitude(0,1)
19 RF.setFreq(0,1e6)
20 RF.setPhase(0,0)
21
22 #Triggered execution
23 RF.waitTriggerIn() #Waits for rising edge
24 RF.setTriggerOut(1) #Outputs trigger for monitoring purposes
25 RF.setAutomaticRURDPins(1,0)
26 RF.delayTimer(20e-6)
```

```
RF.setAutomaticRURDPins(0,0)
RF.setTriggerOut(0)
####################################
# End sequence (function stack)
####################################
```

Code B.3: Single tone mode with automatic ramp-up and ramp-down enabled. The full example is available in [110] under *Examples/singleToneAutomaticRURD.py*.

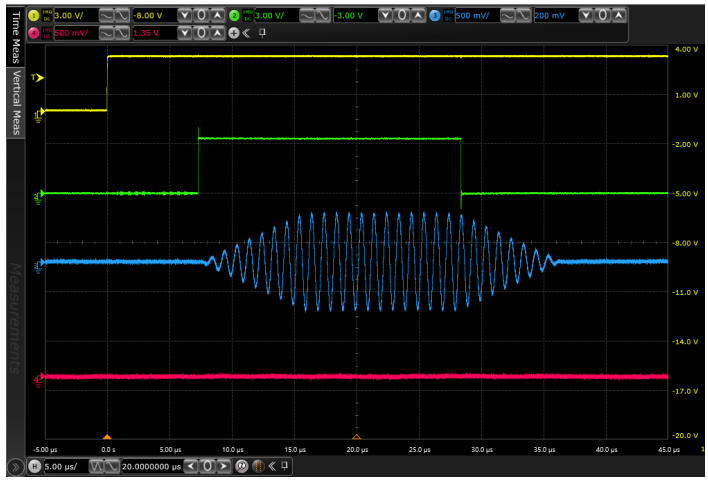

Figure B.2.: Oscilloscope screen capture for the rf driver sequence in Code B.3. The traces are: triggerIn (yellow), triggerOut (green), ch0 (blue) and ch1 (red).

Modulation mode

This functional mode is specially suited for application that require a fast reconfiguration of the waveform parameters. In Table 5.1 we have shown that a direct modulation based on an update of the profile pins only takes 100 ns while a reconfiguration of the AD9958 registers via SPI typically require 4 µs. The example in Code B.4 compares both operations by reconfiguring the frequency in ch0 via the profile pins and by performing the same operation on ch1 but using SPI. The sequence starts by configuring the modulation mode, and configuring the modulation levels for ch0 (0.5 MHz and 2 MHz). On the other hand, only a single frequency value is initially configured for ch1 (0.5 MHz). The central part of this example uses triggered execution. After a rising edge is detected on triggerIn, the frequencies on both channels are commuted from 0.5 MHz to 2 MHz by using direct modulation on ch0 and SPI register access on ch1. 20 µs later, the frequencies are commuted back to 2 MHz by the same means. Note, that we do not use the *delayTimer()* method but use *waitForTimer()* instead, which allows to synchronize the sequence based on the elapsed time since the last *resetTimer()* call. The trigger out port is used for monitoring purposes only. The corresponding waveforms are shown in Fig. B.3. We observe a 4 µs lag in the frequency reconfiguration of ch1 due to the SPI communication overhead.

```
1  ###################################
2  # Start sequence (function stack)
3  ###################################
4  print "Programming sequence."
5  RF.reset()
6  RF.resetTimer()
7  RF.configureSysClock()
8
9  #Channel 0 and 1
10 RF.setEnabledChannels(1,1)
11 RF.setDACFullScale()
12 RF.setModulationMode("frequency",2,0)
13 RF.setModulationRegister(0,0)
14
15 #Channel 0
16 RF.setEnabledChannels(1,0)
17 RF.setAmplitude(0,1)
18 RF.setFreq(0,0.5e6)   #Modulation level 0
19 RF.setFreq(1,2e6)     #Modulation level 1
20 RF.setPhase(0,0)
21
22 #Channel 1
23 RF.setEnabledChannels(0,1)
24 RF.setAmplitude(0,1)
25 RF.setFreq(0,0.5e6)
26 RF.setPhase(0,0)
27
```

```
28 RF.waitTriggerIn() #Waits for rising edge
29 t=0
30 RF.resetTimer()
31 RF.setTriggerOut(1)
32 RF.setModulationRegister(1,0)    #Direct modulation (ch 0)
33 RF.setFreq(0,2e6)                #SPI  (ch1)
34
35 t+=20e-6
36 RF.waitForTimer(t)
37 RF.setTriggerOut(0)
38 RF.setModulationRegister(0,0)    #Direct modulation (ch 0)
39 RF.setFreq(0,0.5e6)              #SPI  (ch1)
40 ####################################
41 # End sequence (function stack)
42 ####################################
```

Code B.4: Frequency modulation mode. This example is an adaptation of the source code in [110] under *Examples/frequencyModulation.py*.

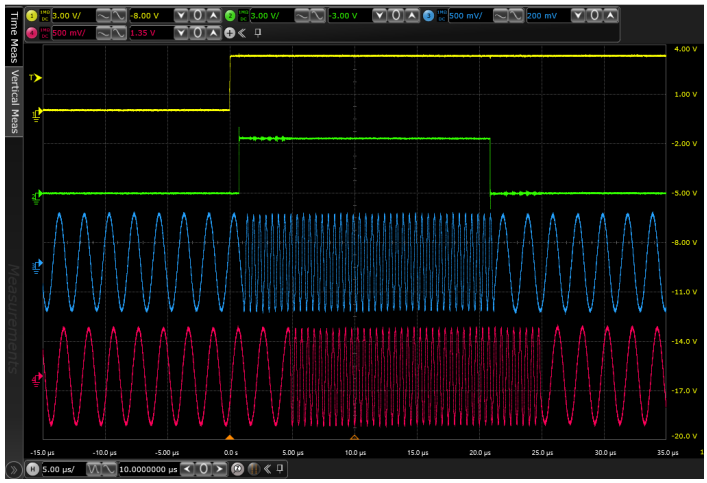

Figure B.3.: Oscilloscope screen capture for the rf driver sequence in Code B.4. The traces are: trigger in (yellow), trigger out (green), ch0 (blue) and ch1 (red).

Sweep mode

In Code B.5 we illustrate the sweep mode of the AD9958. Similarly to the automatic ramp-up and ramp-down mode, the sweep direction is configured via the profile P2 and P3 for ch0 and c1, respectively. We restrict this example to amplitude sweeps. The AD9958 has 4 configurable sweep parameters: the rising/falling sweep ramp rate and the rising/falling delta word. The Python API includes the *findOptimalRamp()* method which calculates these parameters based on the sweep endpoints and the rising/falling sweep durations. In this example we perform independent amplitude sweeps on ch0 and ch1. The start/end amplitude endpoints are 0.25/0.8 and 0.1/0.8 for ch0 and ch1, respectively. Their rising/-falling sweep durations are 10 µs/20 µs and 30 µs/10 µs. The sequence starts with the configuration of the ramps and by setting both channels to the lower frequency endpoint. After, the sequence is put on hold until an external trigger is received. At this point, ch0 is instructed to start a rising ramp and 10 µs later we do similarly for ch1. After an additional hold time of 10 µs, both channels start simultaneously a falling frequency ramp. The triggerOut port is used for monitoring purposes only. The corresponding waveforms are shown in Fig. B.4.

```
###################################
# Start sequence (function stack)
###################################
print "Programming sequence."
RF.reset()
RF.resetTimer()
RF.configureSysClock()

#Channel 0 and 1
RF.setEnabledChannels(1,1)
RF.setDACFullScale()
RF.setSweepMode("amplitude")
RF.setFreq(0,1e6)
RF.setPhase(0,0)
RF.setModulationRegister(0,0)

#Channel 0
RF.setEnabledChannels(1,0)
RF.setSweepParameters(0.25,0.8,10e-6,20e-6)

#Channel 1
RF.setEnabledChannels(0,1)
RF.setSweepParameters(0.1,0.8,30e-6,10e-6)

#Triggered execution
RF.waitTriggerIn() #Waits for rising edge
RF.setTriggerOut(1)
RF.setModulationRegister(1,0)
RF.delayTimer(10e-6)
RF.setModulationRegister(1,1)
```

```
RF.delayTimer(50e-6)
RF.setModulationRegister(0,0)
RF.setTriggerOut(0)
####################################
# End sequence (function stack)
####################################
```

Code B.5: Amplitude seep mode. The full example is available in [110] under *Examples/amplitudeSweep.py*.

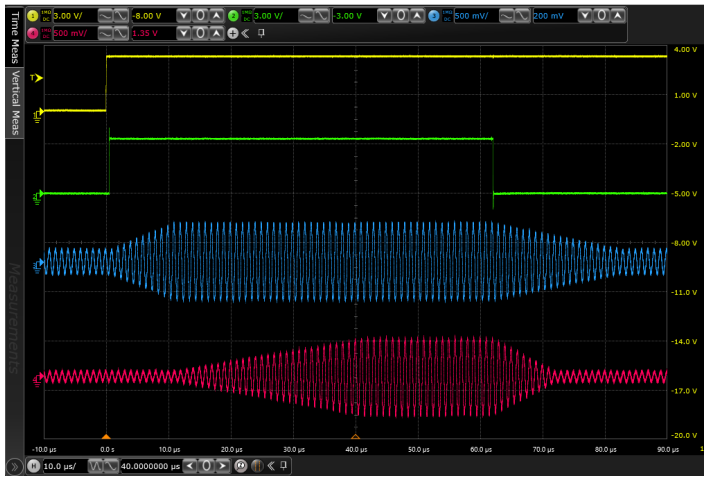

Figure B.4.: Oscilloscope screen capture for the rf driver sequence in Code B.5. The traces are: triggerIn (yellow), triggerOut (green), ch0 (blue) and ch1 (red).

C

Digital PLL laser lock (code example)

This Appendix is devoted to illustrate a basic configuration and operation of the digital PLL lock of the cooler and repumper laser. The source code for the chipKit uC32 firmware can be found in [118].

Loading of the PLL configuration

Instruction	Description
!	Restart FIFO buffers.
?	Return FIFO buffer contents.
c<setPoint>#	Queue jump to new cooler set-point.
r<setPoint>#	Queue jump to new repumper set-point.
c<sweepTime>;<setPoint>#	Queue sweep to new cooler set-point.
r<sweepTime>;<setPoint>#	Queue sweep to new repumper set-point.

Table C.1.: Serial instructions for the digital PLL laser locks. We write the new beat note frequency set-point (MHz) as **<setPoint>** and the sweep time (ms) as **<sweepTime>**. The first two instructions are issued immediately, while the remaining ones are queued to either the cooler or the repumper FIFO buffer.

Prior to running an experimental sequence, the required beat note frequency set-points for the cooler and repumper laser are sent to the microcontroller. The microcontroller features a pair of FIFO buffers, which hold up to 100 instructions for the cooler and repumper laser locks. Instructions are sent over serial interface (9600 baud) and have to be compliant with Table C.1. The instructions set include commands for restart and inspection of the FIFO buffers and for queuing

changes or sweeps in the beat note frequency set-points. In Code C.1 we give a working example on how to use the above instructions set to configure the cooler and repumper FIFO buffers.

```
import serial
import time
#####################################################
# Setting up serial communication
#####################################################
PLL_COM_PORT="COM8"
INFO_MAX_LEN=1000 #Upper bound for serial read
try:
  serPLL   #Check if serial port is already open
except NameError:
  serPLL=serial.Serial(PLL_COM_PORT, 9600, timeout=0.2)
  print("Starting PLL serial port.")
  time.sleep(5) #Waiting for microcontroller to start
#####################################################
# Define set-points and sweep times
#####################################################
cSetPointList  = [ 164,  250, -300, -100,  120]
cSweepTimeList = [   0,   20,    0,   10,    0]
rSetPointList  = [6600, 7000, 6500]
rSweepTimeList = [   0,   50,    0]
#####################################################
# Load FIFO buffers
#####################################################
serPLL.write(b"!")  #Restart
#Configure cooler FIFO buffer
for cSetPoint,cSweepTime in zip(cSetPointList,cSweepTimeList):
    serPLL.write(b"c{};{}#".format(cSetPoint,cSweepTime))
#Configure repumper FIFO buffer
for rSetPoint,rSweepTime in zip(rSetPointList,rSweepTimeList):
    serPLL.write(b"r{};{}#".format(rSetPoint,rSweepTime))
#Read out buffer contents (OPTIONAL)
serPLL.write(b"?")
info=ser.read(INFO_MAX_LEN) #Typically returns on timeout.
print(info)
```

Code C.1: Configuration of the PLL instructions buffers involving 5 (3) distinct frequency set-points for the cooler (repumper) lock.

We note that positive as well as negative beat note frequency set-points can be used and that the microcontroller automatically handles the polarity of the PLL output. While set-points of the same sign can be appended without restrictions in their frequencies and sweep times, this is not the case for set-points that feature distinct signs. When a positive (negative) set-point is appended to a negative (positive) one, the following restrictions apply:

(i) **Increasing order**. The absolute value of the set-points have to be requested in increasing order. That is, $|setPointList[i]| < |setPointList[i+$

$1]|$ results in a stable change while $|setPointList[i]| \geqslant |setPointList[i+1]|$ drives the system out of lock. Changes in the beat note frequency that violate this conditions can still be achieved by adding an auxiliary set-point in between. For example, the sequence $setPointList = [..., 250, -100, ...]$ can be achieved through $setPointList = [..., 250, -300, -100, ...]$, where we have introduced the auxiliary value of -300 to perform the transition from positive to negative set-points.

(ii) **Zero sweep time**. Changes in the beat note frequency set-point that involve switching the lock polarity shall be done by queuing a frequency jump (**c<setPoint>#** and **r<setPoint>#**), or equivalently by queueing a sweep with 0 sweep time (**c0;<setPoint>#** and **r0;<setPoint>#**).

Execution of the instruction buffer

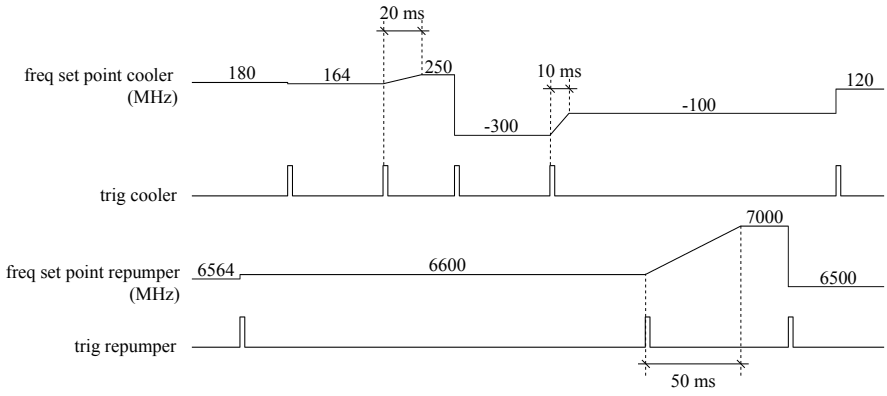

Figure C.1.: Execution of the PLL intruction buffers which got previously configured through Code C.1. After detecting a rising edge on the cooler (rempumper) trigger line, the cooler (repumper) PLL is configured based on the next entry of its instruction buffer.

Once the required beat note frequency set-points have been added to the instruction FIFO buffers, the device is ready to execute them upon trigger requests. This is, the cooler (repumper) PLL lock are programmed with the next buffered instruction whenever a rising edge is detected on the cooler (repumper) trigger line.

In Fig. C.1 we illustrate a typical execution of the cooler and repumper instruction buffers. This example is based on Code C.1, which requires 5 trigger

instructions for the cooler PLL and 3 trigger instructions for the repumper PLL. Note that the initial set-points are not defined by the Python sequence. This is because they are either automatically programmed to their default value when powering up the chipKit uC32, or they got set by a previously executed instruction buffer. In this example, the initial set-points are 180 MHz and 6564 MHz, which correspond to the default configuration of the cooler and repumper locks.

D

Phase-resolved parametric amplification

Optical parametric amplifiers use non-linear optical media to couple electric fields that oscillate at different frequencies [44]. At their input, an intense *pump* field is combined with a weak *signal* field, which respectively get attenuated and exponentially amplified within the non-linear medium. The excess energy and momentum are transferred to a third optical field, typically denoted as the *idler* field. The coupling between fields in an optical parametric amplifier is analogous to the spin mixing interaction within $f = 1$ SBECs, which couples the spin pair configurations $|1,0\rangle \otimes |1,0\rangle$ and $|1,-1\rangle \otimes |1,+1\rangle$. In this case, the atoms in $|1,0\rangle$ and $|1,\pm1\rangle$ take the role of pump and signal/idler fields. The exponential amplification of the fields in $|1,\pm1\rangle$ is influenced by the non-linear interaction strength as well as the QZS and trapping potential, which introduces an energy offset between the spin mixing input configuration ($|1,0\rangle \otimes |1,0\rangle$) and the output configuration ($|1,-1\rangle \otimes |1,+1\rangle$) [45, 46].

In this chapter, we demonstrate phase-resolved parametric amplification within our SBEC comagnetometer. The parametric amplification takes place within the $\{|2,0\rangle, |2,\pm1\rangle\}$ subspace of the $f = 2$ manifold, while the $f = 1$ manifold keeps track of the rotating reference frame.

Theoretical framework

We build upon the work by Klempt *et al.* [46, 47] and describe the pair creation in the $|2,\pm1\rangle$ states as spin excitations within a spherical potential well. The spatial wavefunctions of the spin excitations are most conveniently written in spherical coordinates:

$$\Psi(r,\theta,\phi) = Z^{-1/2} j_l\left(\beta_{n,l}\frac{r}{r_{\mathrm{TF}}}\right) Y_{l,m}(\theta,\phi)\,, \tag{D.1a}$$

$$Z = \int_0^{r_{\mathrm{TF}}} \left| j_l \left(\beta_{n,l} \frac{r}{r_{\mathrm{TF}}} \right) \right|^2 4\pi r^2 dr \tag{D.1b}$$

where j_l is the spherical Bessel function, $\beta_{n,l}$ its nth zero and r_{TF} is the Thomas-Fermi radius (see Appendix A). The angular dependency is given by the spherical harmonic $Y_{l,m}(\theta, \phi)$. Regarding the indices we have $n = 1, 2, 3, ...$, $l = 0, 1, 2, 3, ...$ and $m = -l, ... + l$, where only the first two are relevant for the spin excitation eigenenergy $E_{n,l}$:

$$E_{n,l} = \sqrt{(\epsilon_{n,l} + q)^2 - \Omega^2}\,, \tag{D.2a}$$

$$\epsilon_{n,l} = \frac{\hbar^2 \beta_{n,l}^2}{2m r_{\mathrm{TF}}^2}\,, \tag{D.2b}$$

$$\Omega = \frac{N_A \rho_0^{(2)}}{V_{\mathrm{eff}}} \left(3 g_1^{(2)} - \frac{g_2^{(2)}}{5} \right)\,. \tag{D.2c}$$

We refer to Eq. (2.20) for the definition of $g_1^{(2)}$ and $g_2^{(2)}$, and to Appendix A for the definition of V_{eff}. When $(\epsilon_{n,l} + q)^2 < \Omega^2$, the eigenenergy is imaginary and the atom number within the corresponding spin excitation gets parametrically (exponentially) amplified. Later in this chapter we will see that, for our experimental conditions, only the lowest energy eigenstate ($n = 1$, $l = 0$, $m = 0$) has an imaginary eigenenergy. In this case, the excitation wavefunction is $\Psi_{1,0,0}(\mathbf{r}) \propto \mathrm{sinc}(r/r_{\mathrm{TF}})$ and has a high overlap with the Thomas-Fermi density profile of the pump field $\Psi_{\mathrm{SMA}}(\mathbf{r}) \propto \sqrt{1 - (r/r_{\mathrm{TF}})^2}$. More precisely, the overlap is quantified through the integral

$$\langle \Psi_{n,l,m} | \Psi_{\mathrm{SMA}} \rangle = \delta_{l,0} \delta_{m,0} Z^{-1/2} \int_0^{r_{\mathrm{TF}}} j_l \left(\beta_{n,l} \frac{r}{r_{\mathrm{TF}}} \right) \Psi_{\mathrm{SMA}}(r)\, 4\pi r^2 dr\,, \tag{D.3}$$

which for the lowest energy eigenstate yields $\langle \Psi_{1,0,0} | \Psi_{\mathrm{SMA}} \rangle = 0.94$. Hence, for our experimental conditions, the pump and signal/idler fields can be described within the single-mode approximation by the spin amplitudes $\xi_0^{(2)}$ and $\xi_{\pm 1}^{(2)}$. In this case, parametric amplification corresponds to an exponential amplification of the original spin amplitudes in $\xi_{\pm 1}^{(2)}$.

Seeding mechanisms

We denote the original spin amplitudes in $\xi_{\pm 1}^{(2)}$ as *seeding fields*. Depending on their origin we distinguish between:

- *Coherent seeding.* This results from the coherent transfer of atomic population into the $\xi_{\pm1}^{(2)}$ fields. This type of seeding has a defined amplitude and relative phase to the pump field $\xi_0^{(2)}$. As a result, the parametrically amplified fields are equally deterministic in amplitude and phase.

- *Classical noise seeding.* Rf noise couples the ξ_0^2 and $\xi_{\pm1}^{(2)}$ fields and can provide and initial spin population in the latter ones. Since, both phase and instantaneous amplitude of the driving field are unknown, the resulting seeding fields are non-deterministic. This is reflected in a large variance in phase and amplitude of the parametrically amplified fields.

- *Quantum noise seeding.* An unavoidable seeding mechanism is vacuum fluctuations in the $\xi_{\pm1}^{(2)}$ fields. Similarly to the method above, the resulting amplified fields feature a large variance in amplitude and phase. The difference here is that the non-determinism is an inherent property of vacuum fluctuations and does not result from a *lack of control* in the driving field. For numerical calculations using the truncated Wigner method, vacuum fluctuations can be included through a normal distribution in the $\xi_{\pm1}^{(2)}$ fields with a mean seeding population of $\langle|\xi_{\pm1}^{(2)}|^2\rangle \approx 1/2$ [181, 182].

The classical and quantum noise floor define the smallest resolvable coherent seedings. Above that threshold, coherent seedings are deterministically magnified by the *gain* of the parametric amplifier. We note that the parametric amplification process is inherently phase-sensitive but for the typical experimental evolution times $t_{\mathrm{hold}} \gtrsim 20\,\mathrm{ms}$ [46, 47, 45] the phase information is *washed out* due to the environmental magnetic field fluctuations. E.g. the pioneering work by Sadler *et al.* [45] achieved a 30 dB amplification in their spin amplitudes but did not demonstrate that the reported spin orientations (i.e. phase information) stayed preserved during the process.

Magnetic noise cancellation and state preparation

In the following we prepare a $f = 2$ parametric spin amplifier within the SBEC comagnetometer described in Chapter 6. More precisely, we produce a coherent spin superposition where the parametric amplification occurs within $f = 2$, while the $f = 1$ manifold keeps track of the rotating reference frame resulting from the (fluctuating) external magnetic field.

The state preparation consists of a a set of resonant mw and rf pulses to obtain 60% of the atomic population within a magnetically sensitive superposition within $f = 1$ and the remaining 40% within the $f = 2$ pump, signal and idler fields $\{\xi_0^{(2)}, \xi_{\pm1}^{(2)}\}$. The pulse sequence is described in Table D.1, which is parametrized in

Item	Rotation	Type	Coupled levels	$\rho^{(1)}$	$\rho^{(2)}$
0				$(0,1,0)$	$(0,0,0,0,0)$
1	$R_0[\beta_1]$	rf	$\lvert f,m\rangle \leftrightarrow \lvert f,m\pm1\rangle$	$(\frac{1-\rho_0^{(2)}}{4}, \frac{1+\rho_0^{(2)}}{2}, \frac{1-\rho_0^{(2)}}{4})$	$(0,0,0,0,0)$
2	$R_0[\beta_2]$	mw	$\lvert 1,0\rangle \leftrightarrow \lvert 2,0\rangle$	$(\frac{1-\rho_0^{(2)}}{4}, \frac{1-\rho_0^{(2)}}{2}, \frac{1-\rho_0^{(2)}}{4})$	$(0,0,\rho_0^{(2)},0,0)$
3	$R_0[\beta_3]$	rf	$\lvert f,m\rangle \leftrightarrow \lvert f,m\pm1\rangle$	$(\frac{1-\rho_0^{(2)}}{4}, \frac{1-\rho_0^{(2)}}{2}, \frac{1-\rho_0^{(2)}}{4})$	$(0,\delta\rho,\rho_0^{(2)},\delta\rho,0)$

Table D.1.: Rf and mw pulse sequence for the generation of parametric amplifier in a SBEC comagnetometer. The required rotations are written as $R_\alpha[\beta]$, where β is the rotation angle and α is the azimuth angle of the rotation axis. We assume small seeding populations $\delta\rho \ll \rho_0^{(2)}$ for which the rotation angles are: $\beta_1 = \arcsin\left[((1-\rho_0^{(2)})/2)^{1/2}\right]$, $\beta_2 = 2\arcsin\left[(2\rho_0^{(2)}/(1+\rho_0^{(2)}))^{1/2}\right]$ and $\beta_3 = 3^{-1/2}\arcsin\left[(2\delta\rho/\rho_0^{(2)})^{1/2}\right]$.

terms of the relative atomic populations $\rho_0^{(2)} = 0.4$ and relative coherent seeding $\delta\rho \in [2\times10^{-6}, 5\times10^{-4}]$. The absolute atom number is $N_A = 92(2)\times10^3$, such that the coherent seeding atom numbers are within $\delta N_A = \delta\rho N_A \in [0.2, 50]$.

Resolution of the phase-resolved parametric amplifier

After state preparation, the system is allowed to freely evolve for 75 ms at a magnetic field of 282 mG. In these conditions, only the lowest energy excitation in Eqs. (D.2) becomes imaginary $E_{1,0} \approx i7.5$ Hz. The seedings in $\xi_{\pm1}^{(2)}$ are, as a result, exponentially amplified. After amplification, the $f = 2$ manifold has developed a transverse magnetisation, where the azimuth spin orientation angle $\theta^{(2)}$ relates to the relative phase between the $\xi_0^{(2)}$ and the $\xi_{\pm1}^{(2)}$ fields. However, a direct measurement of $\theta^{(2)}$ does not reveal the phase of the original seeding because of the magnetic field fluctuations during the 75 ms long amplification process. For this reason, we make use of the comagnetometer readout $\theta^{(12)} = \theta^{(1)} + \theta^{(2)}$, which does not depend on the magnetic field evolution and is a direct measurement of the phase of the original seeding fields.

In Fig. D.1 we show preliminary results on the resolution of our phase-resolving parametric amplifier and estimate the smallest resolvable coherent seed below which the non-deterministic contributions (rf noise and vacuum fluctuations) become dominant. To this end, we compute the sharpness S (see Section 6.4) of the comagnetometer readout as a function of the seeding atom number δN_A. The transition between non-deterministic ($S \sim 0$) and deterministic seeding ($S \sim 1$)

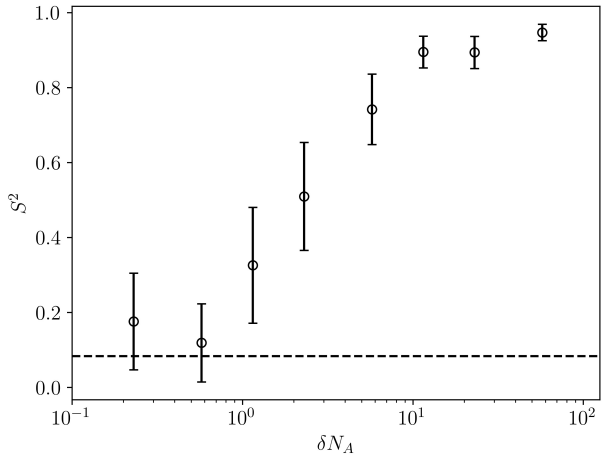

Figure D.1.: Evolution of S^2, where $S \equiv |\langle \exp[i\theta] \rangle|$ is the sharpness, as a function of the coherent seeding of the parametric amplifier δN_A. Averages are taken over $K = 12$ samples. Error bars are the statistical uncertainty and the dashed line is the lower bound $S^2 = 1/K$.

happens at $\delta N_A \sim 5$ or equivalently $\delta\rho \sim 5 \times 10^{-5}$. We note that the latter value is above an order of magnitude smaller than the seedings reported for SU(1,1) SBEC interferometers [49, 50, 51].

E

Experimental sequences for measuring the interhyperfine interaction in ^{87}Rb

Interaction parameter $g_2^{(12)}$

(See Fig. E.1 top) After all-optical evaporation, a SBEC is obtained in the $\xi^{(1)}/\sqrt{N} = (0,1,0)^T$ state. The ensemble is coherently transferred into an equal superposition $\xi/\sqrt{N_A} = (0,1/\sqrt{2},0)^T \oplus (0,0,0,0,1/\sqrt{2})^T$ by means of a resonant radio frequency (rf) $\pi/2$ rotation around the x-axis and a sequence of microwave (mw) π pulses (I, II and III). Thereafter, the magnetic field is ramped up to 381.5 mG in order to raise the differential LZS to $(p^{(1)} + p^{(2)})/h = -1.06$ kHz. A Ramsey-like sequence, consisting of two rf $\pi/8$ pulses (rotating about $\mathbf{x}$) separated by 462 µs is used to produce a net $\pi/4$ rotation of the $f = 1$ manifold, and zero net rotation of the $f = 2$ manifold. The resulting state is given in Eq. (7.3). The magnetic field is rapidly ramped down to 119.6 mG, ensuring a modest QZS during the subsequent many-body (MB) evolution. After a variable hold time t, the magnetizations in $f = 1$ and $f = 2$ are detected by Faraday rotation. A first pulse ($\Delta^{(10')}/2\pi = -270$ MHz) probes the $f = 1$ transverse magnetization. A rf $\pi/2$ pulse is then applied to rotate the $f = 2$ stretched state $\xi^{(2)}/\sqrt{N_A} = (0,0,0,0,1/\sqrt{2})^T$ into the transverse plane for detection with a second pulse ($\Delta^{(23')}/2\pi = 360$ MHz). The damped oscillatory signals illustrate the recorded Faraday signals described in Eqs. (5.11).

Interaction parameter $g_1^{(12)}$

(See Fig. E.1 bottom) The sequence starts with a SBEC in $\xi^{(1)}/\sqrt{N} = (0,1,0)^T$ which is coherently split by a rf $\pi/2$ pulse into $\xi^{(1)}/\sqrt{N} = (1/\sqrt{2},0,1/\sqrt{2})^T$. Subsequently, either the initial state $\xi_{0,A}$ or $\xi_{0,B}$ is prepared via mw pulses (I, II and III) and a rf $\pi/6$ rotation around the $\mathbf{x}$ axis. Hereafter, the many-body

(MB) evolution begins. For the applied constant magnetic field of 119.6 mG the LZS is $p^{(2)}/h \approx -p1^{(1)}/h = 84\,\text{kHz}$ with a differential frequency of $p^{(1)}/h + p^{(2)}/h = -334\,\text{Hz}$. The insets illustrate how the $f = 1$ and $f = 2$ transverse spin orientations ($\theta_A^{(1)}$ and $\theta_A^{(2)}$ or $\theta_B^{(1)}$ and $\theta_B^{(2)}$) rapidly evolve due to the LZS. The differential is represented by the green comagnetometer readouts, which depending on the state preparation are labeled by $\theta_A^{(12)}$ and $\theta_B^{(12)}$. After a variable hold time of up to 200 ms, the transverse magnetization is interrogated . First the Faraday probe of $f = 1$ is applied, from which, depending on the state preparation, the spin orientation $\theta_A^{(1)}$ or $\theta_B^{(1)}$ is obtained. Next, and without any additional rf pulse, the $f = 2$ manifold is probed, yielding $\theta_A^{(2)}$ or $\theta_B^{(2)}$. The comagnetometer readout is obtained by $\theta_X^{(12)} \equiv \theta_X^{(1)} + \theta_X^{(2)}$, where $X \in \{A, B\}$. Faraday probing frequencies and atom-light coupling factors are identical to the previous section.

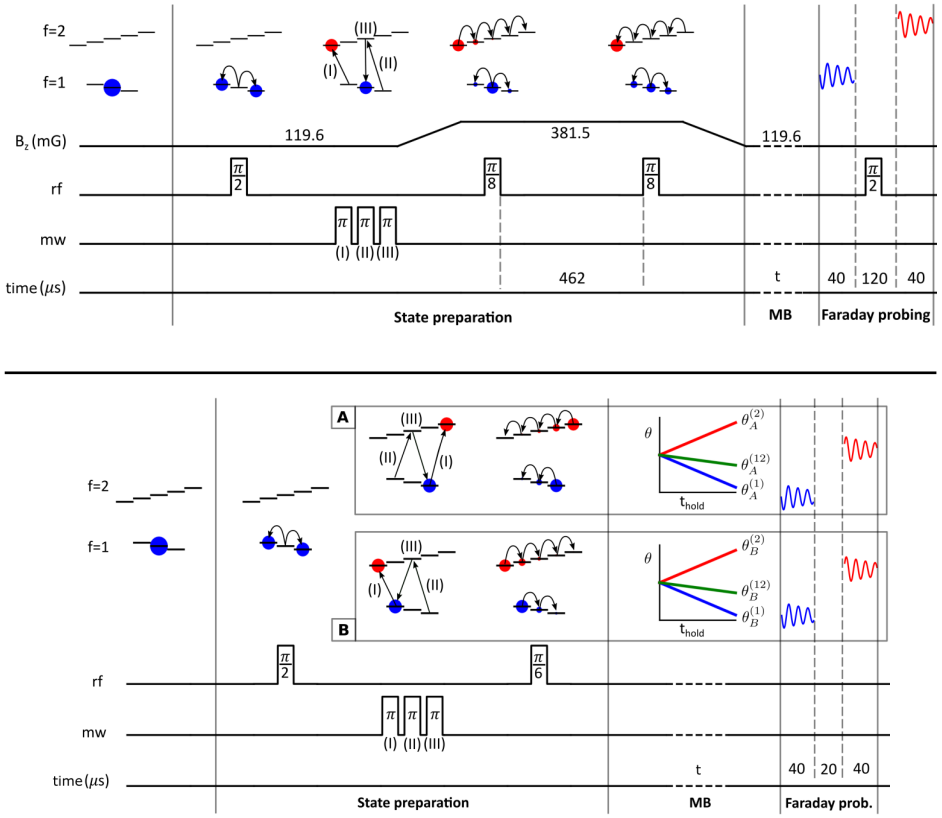

Figure E.1.: Experimental sequences for the determination of the interhyperfine interaction parameters $g_2^{(12)}$ (top) and $g_1^{(12)}$ (bottom). The relative spin populations $\rho^{(1)}$ and $\rho^{(2)}$ are represented by the blue and red circles. The oscillatory traces at the end of both sequences illustrate the consecutive Faraday readouts of the transverse magnetization in each hyperfine manifold. Note that the bottom sequence branches into A or B for the many-body (MB) evolution of a SBEC initially prepared in $\xi_{0,A}$ or $\xi_{0,B}$, respectively. The insets of this latter sequence show the angular evolution of the transverse spins $\theta_A^{(f)}$ and $\theta_B^{(f)}$, as well as the corresponding comagnetometer readouts ($\theta_A^{(12)}$ and $\theta_B^{(12)}$).

List of publications

(i) P. Gomez, F. Martin, C. Mazzinghi, D. Benedicto Orenes, S. Palacios, and M. W. Mitchell, *Bose-Einstein Condensate Comagnetometer*, Phys. Rev. Lett., vol. 124, p. 170401, 2020.

(ii) P. Gomez, C. Mazzinghi, F. Martin, S. Coop, S. Palacios, and M. W. Mitchell, *Interferometric measurement of interhyperfine scattering lengths in* ^{87}Rb, Phys. Rev. A, vol. 100, p. 032704, 2019.

(iii) V. Prakash, L .C. Bianchet, M. T. Cuairan, P. Gomez, N. Bruno, and M. W. Mitchell, *Narrowband photon pairs with independent frequency tuning for quantum light-matter interactions*, Optics Express, vol. 27, no. 26, pp. 38463–38478, 2019.

(iv) S. Coop, S. Palacios,P. Gomez, Y. N. M. de Escobar, T. Vanderbruggen, and M. W. Mitchell, *Floquet theory for atomic light-shift engineering with near-resonant polychromatic fields*, Optics Express, vol. 25, no. 26, pp. 32550–32559, 2017.

(v) S. Palacios, S. Coop, P. Gomez, T. Vanderbruggen, Y. N. M. de Escobar, M. Jasperse, and M. W. Mitchell, *Multi-second magnetic coherence in a single domain spinor Bose–Einstein condensate*, New Journal of Physics, vol. 20, no. 5, p. 053008, 2018.

Bibliography

[1] C. C. Bradley, C. A. Sackett, J. J. Tollett, and R. G. Hulet, "Evidence of Bose-Einstein Condensation in an Atomic Gas with Attractive Interactions," Phys. Rev. Lett., vol. 75, pp. 1687–1690, Aug 1995.

[2] K. B. Davis, M. O. Mewes, M. R. Andrews, N. J. van Druten, D. S. Durfee, D. M. Kurn, and W. Ketterle, "Bose-Einstein Condensation in a Gas of Sodium Atoms," Phys. Rev. Lett., vol. 75, pp. 3969–3973, Nov 1995.

[3] Anderson, M. H. and Ensher, J. R. and Matthews, M. R. and Wieman, C. E. and Cornell, E. A., "Observation of bose-einstein condensation in a dilute atomic vapor," Science, vol. 269, no. 5221, pp. 198–201, 1995.

[4] D. Han, R. Wynar, P. Courteille, and D. Heinzen, "Bose-Einstein condensation of large numbers of atoms in a magnetic time-averaged orbiting potential trap," Physical Review A, vol. 57, no. 6, p. R4114, 1998.

[5] U. Ernst, A. Marte, F. Schreck, J. Schuster, and G. Rempe, "Bose-Einstein condensation in a pure Ioffe-Pritchard field configuration," EPL (Europhysics Letters), vol. 41, no. 1, p. 1, 1998.

[6] T. Esslinger, I. Bloch, and T. W. Hänsch, "Bose-einstein condensation in a quadrupole-ioffe-configuration trap," Phys. Rev. A, vol. 58, pp. R2664–R2667, Oct 1998.

[7] D. S. Jin, J. R. Ensher, M. R. Matthews, C. E. Wieman, and E. A. Cornell, "Collective Excitations of a Bose-Einstein Condensate in a Dilute Gas," Phys. Rev. Lett., vol. 77, pp. 420–423, Jul 1996.

[8] M. R. Andrews, D. M. Kurn, H.-J. Miesner, D. S. Durfee, C. G. Townsend, S. Inouye, and W. Ketterle, "Propagation of Sound in a Bose-Einstein Condensate," Phys. Rev. Lett., vol. 79, pp. 553–556, Jul 1997.

[9] D. M. Stamper-Kurn, H.-J. Miesner, S. Inouye, M. R. Andrews, and W. Ketterle, "Collisionless and Hydrodynamic Excitations of a Bose-Einstein Condensate," Phys. Rev. Lett., vol. 81, pp. 500–503, Jul 1998.

[10] K. W. Madison, F. Chevy, W. Wohlleben, and J. Dalibard, "Vortex Formation in a Stirred Bose-Einstein Condensate," Phys. Rev. Lett., vol. 84, pp. 806–809, Jan 2000.

[11] J. Abo-Shaeer, C. Raman, J. Vogels, and W. Ketterle, "Observation of vortex lattices in Bose-Einstein condensates," Science, vol. 292, no. 5516, pp. 476–479, 2001.

[12] M. Andrews, C. Townsend, H.-J. Miesner, D. Durfee, D. Kurn, and W. Ketterle, "Observation of interference between two Bose condensates," Science, vol. 275, no. 5300, pp. 637–641, 1997.

[13] D. S. Hall, M. R. Matthews, C. E. Wieman, and E. A. Cornell, "Measurements of Relative Phase in Two-Component Bose-Einstein Condensates," Phys. Rev. Lett., vol. 81, pp. 1543–1546, Aug 1998.

[14] L. Deng, E. W. Hagley, J. Wen, M. Trippenbach, Y. Band, P. S. Julienne, J. Simsarian, K. Helmerson, S. Rolston, and W. D. Phillips, "Four-wave mixing with matter waves," Nature, vol. 398, no. 6724, pp. 218–220, 1999.

[15] J. Denschlag, J. E. Simsarian, D. L. Feder, C. W. Clark, L. A. Collins, J. Cubizolles, L. Deng, E. W. Hagley, K. Helmerson, W. P. Reinhardt, S. L. Rolston, B. I. Schneider, and W. D. Phillips, "Generating Solitons by Phase Engineering of a Bose-Einstein Condensate," Science, vol. 287, no. 5450, pp. 97–101, 2000.

[16] C. J. Pethick and H. Smith, "Bose–Einstein condensation in dilute gases," Cambridge university press, 2001.

[17] L. Pitaevskii and S. Stringari, "Bose–Einstein Condensation," Oxford university press, 2003.

[18] F. Dalfovo, S. Giorgini, L. P. Pitaevskii, and S. Stringari, "Theory of Bose-Einstein condensation in trapped gases," Rev. Mod. Phys., vol. 71, pp. 463–512, Apr 1999.

[19] A. J. Leggett, "Bose-Einstein condensation in the alkali gases: Some fundamental concepts," Rev. Mod. Phys., vol. 73, pp. 307–356, Apr 2001.

[20] D. S. Hall, M. R. Matthews, J. R. Ensher, C. E. Wieman, and E. A. Cornell, "Dynamics of Component Separation in a Binary Mixture of Bose-Einstein Condensates," Phys. Rev. Lett., vol. 81, pp. 1539–1542, Aug 1998.

[21] D. M. Stamper-Kurn, M. R. Andrews, A. P. Chikkatur, S. Inouye, H.-J. Miesner, J. Stenger, and W. Ketterle, "Optical Confinement of a Bose-Einstein Condensate," Phys. Rev. Lett., vol. 80, pp. 2027–2030, Mar 1998.

[22] J. Stenger, S. Inouye, D. Stamper-Kurn, H.-J. Miesner, A. Chikkatur, and W. Ketterle, "Spin domains in ground-state Bose–Einstein condensates," Nature, vol. 396, no. 6709, p. 345, 1998.

[23] M. D. Barrett, J. A. Sauer, and M. S. Chapman, "All-optical formation of an atomic bose-einstein condensate," Phys. Rev. Lett., vol. 87, p. 010404, Jun 2001.

[24] Y. Kawaguchi and M. Ueda, "Spinor Bose-Einstein condensates," Physics Reports, vol. 520, no. 5, pp. 253–381, 2012.

[25] D. M. Stamper-Kurn and M. Ueda, "Spinor Bose gases: Symmetries, magnetism, and quantum dynamics," Rev. Mod. Phys., vol. 85, pp. 1191–1244, Jul 2013.

[26] S. Wildermuth, S. Hofferberth, I. Lesanovsky, E. Haller, L. M. Andersson, S. Groth, I. Bar-Joseph, P. Krüger, and J. Schmiedmayer, "Microscopic magnetic-field imaging," Nature, vol. 435, no. 7041, pp. 440–440, 2005.

[27] S. Wildermuth, S. Hofferberth, I. Lesanovsky, S. Groth, P. Krüger, J. Schmiedmayer, and I. Bar-Joseph, "Sensing electric and magnetic fields with Bose-Einstein condensates," Applied physics letters, vol. 88, no. 26, p. 264103, 2006.

[28] Y. Eto, H. Saito, and T. Hirano, "Observation of Dipole-Induced Spin Texture in an ^{87}Rb Bose-Einstein Condensate," Phys. Rev. Lett., vol. 112, p. 185301, May 2014.

[29] Y. Eto, H. Ikeda, H. Suzuki, S. Hasegawa, Y. Tomiyama, S. Sekine, M. Sadgrove, and T. Hirano, "Spin-echo-based magnetometry with spinor Bose-Einstein condensates," Phys. Rev. A, vol. 88, p. 031602, Sep 2013.

[30] J. M. Higbie, L. E. Sadler, S. Inouye, A. P. Chikkatur, S. R. Leslie, K. L. Moore, V. Savalli, and D. M. Stamper-Kurn, "Direct Nondestructive Imaging of Magnetization in a Spin-1 Bose-Einstein Gas," Phys. Rev. Lett., vol. 95, p. 050401, Jul 2005.

[31] M. Vengalattore, J. M. Higbie, S. R. Leslie, J. Guzman, L. E. Sadler, and D. M. Stamper-Kurn, "High-Resolution Magnetometry with a Spinor Bose-Einstein Condensate," Phys. Rev. Lett., vol. 98, p. 200801, May 2007.

[32] M. Vengalattore, S. R. Leslie, J. Guzman, and D. M. Stamper-Kurn, "Spontaneously Modulated Spin Textures in a Dipolar Spinor Bose-Einstein Condensate," Phys. Rev. Lett., vol. 100, p. 170403, May 2008.

[33] S. Palacios, S. Coop, P. Gomez, T. Vanderbruggen, Y. N. M. de Escobar, M. Jasperse, and M. W. Mitchell, "Multi-second magnetic coherence in a single domain spinor Bose–Einstein condensate," New Journal of Physics, vol. 20, no. 5, p. 053008, 2018.

[34] M. W. Mitchell and S. Palacios Alvarez, "Colloquium: Quantum limits to the energy resolution of magnetic field sensors," Rev. Mod. Phys., vol. 92, p. 021001, Apr 2020.

[35] A. Widera, F. Gerbier, S. Fölling, T. Gericke, O. Mandel, and I. Bloch, "Precision measurement of spin-dependent interaction strengths for spin-1 and spin-2 87 Rb atoms," New Journal of Physics, vol. 8, no. 8, p. 152, 2006.

[36] M.-S. Chang, Q. Qin, W. Zhang, L. You, and M. S. Chapman, "Coherent spinor dynamics in a spin-1 Bose condensate," Nature Physics, vol. 1, pp. 111 EP –, Oct 2005. Article.

[37] A. T. Black, E. Gomez, L. D. Turner, S. Jung, and P. D. Lett, "Spinor Dynamics in an Antiferromagnetic Spin-1 Condensate," Phys. Rev. Lett., vol. 99, p. 070403, Aug 2007.

[38] D. M. Harber, H. J. Lewandowski, J. M. McGuirk, and E. A. Cornell, "Effect of cold collisions on spin coherence and resonance shifts in a magnetically trapped ultracold gas," Phys. Rev. A, vol. 66, p. 053616, Nov 2002.

[39] S. Knoop, T. Schuster, R. Scelle, A. Trautmann, J. Appmeier, M. K. Oberthaler, E. Tiesinga, and E. Tiemann, "Feshbach spectroscopy and analysis of the interaction potentials of ultracold sodium," Phys. Rev. A, vol. 83, p. 042704, Apr 2011.

[40] K. M. Mertes, J. W. Merrill, R. Carretero-González, D. J. Frantzeskakis, P. G. Kevrekidis, and D. S. Hall, "Nonequilibrium Dynamics and Superfluid Ring Excitations in Binary Bose-Einstein Condensates," Phys. Rev. Lett., vol. 99, p. 190402, Nov 2007.

[41] M. Egorov, B. Opanchuk, P. Drummond, B. V. Hall, P. Hannaford, and A. I. Sidorov, "Measurement of s-wave scattering lengths in a two-component Bose-Einstein condensate," Phys. Rev. A, vol. 87, p. 053614, May 2013.

[42] Y. Eto, H. Shibayama, H. Saito, and T. Hirano, "Spinor dynamics in a mixture of spin-1 and spin-2 Bose-Einstein condensates," Phys. Rev. A, vol. 97, p. 021602, Feb 2018.

[43] N. Irikura, Y. Eto, T. Hirano, and H. Saito, "Ground-state phases of a mixture of spin-1 and spin-2 Bose-Einstein condensates," Phys. Rev. A, vol. 97, p. 023622, Feb 2018.

[44] M. Fox, "Quantum optics: an introduction," OUP Oxford, vol. 15, 2006.

[45] S. R. Leslie, J. Guzman, M. Vengalattore, J. D. Sau, M. L. Cohen, and D. M. Stamper-Kurn, "Amplification of fluctuations in a spinor Bose-Einstein condensate," Phys. Rev. A, vol. 79, p. 043631, Apr 2009.

[46] C. Klempt, O. Topic, G. Gebreyesus, M. Scherer, T. Henninger, P. Hyllus, W. Ertmer, L. Santos, and J. J. Arlt, "Parametric Amplification of Vacuum Fluctuations in a Spinor Condensate," Phys. Rev. Lett., vol. 104, p. 195303, May 2010.

[47] M. Scherer, B. Lücke, G. Gebreyesus, O. Topic, F. Deuretzbacher, W. Ertmer, L. Santos, J. J. Arlt, and C. Klempt, "Spontaneous Breaking of Spatial and Spin Symmetry in Spinor Condensates," Phys. Rev. Lett., vol. 105, p. 135302, Sep 2010.

[48] B. Yurke, S. L. McCall, and J. R. Klauder, "SU(2) and SU(1,1) interferometers," Phys. Rev. A, vol. 33, pp. 4033–4054, Jun 1986.

[49] D. Linnemann, H. Strobel, W. Muessel, J. Schulz, R. J. Lewis-Swan, K. V. Kheruntsyan, and M. K. Oberthaler, "Quantum-Enhanced Sensing Based on Time Reversal of Nonlinear Dynamics," Phys. Rev. Lett., vol. 117, p. 013001, Jun 2016.

[50] D. Linnemann, J. Schulz, W. Muessel, P. Kunkel, M. Prüfer, A. Frölian, H. Strobel, and M. Oberthaler, "Active SU (1, 1) atom interferometry," Quantum Science and Technology, vol. 2, no. 4, p. 044009, 2017.

[51] J. P. Wrubel, A. Schwettmann, D. P. Fahey, Z. Glassman, H. K. Pechkis, P. F. Griffin, R. Barnett, E. Tiesinga, and P. D. Lett, "Spinor Bose-Einstein-condensate phase-sensitive amplifier for SU(1,1) interferometry," Phys. Rev. A, vol. 98, p. 023620, Aug 2018.

[52] P. Gomez, F. Martin, C. Mazzinghi, D. Benedicto Orenes, S. Palacios, and M. W. Mitchell, "Bose-Einstein Condensate Comagnetometer," Phys. Rev. Lett., vol. 124, p. 170401, Apr 2020.

[53] P. Gomez, C. Mazzinghi, F. Martin, S. Coop, S. Palacios, and M. W. Mitchell, "Interferometric measurement of interhyperfine scattering lengths in ^{87}Rb," Phys. Rev. A, vol. 100, p. 032704, Sep 2019.

[54] M. D. Barrett, J. A. Sauer, and M. S. Chapman, "All-Optical Formation of an Atomic Bose-Einstein Condensate," Phys. Rev. Lett., vol. 87, p. 010404, Jun 2001.

[55] T.-L. Ho, "Spinor Bose Condensates in Optical Traps," Phys. Rev. Lett., vol. 81, pp. 742–745, Jul 1998.

[56] T. Ohmi and K. Machida, "Bose-Einstein condensation with internal degrees of freedom in alkali atom gases," Journal of the Physical Society of Japan, vol. 67, no. 6, pp. 1822–1825, 1998.

[57] D. A. Steck, "Rubidium 87 D line data," 2001.

[58] S. Bize, Y. Sortais, M. Santos, C. Mandache, A. Clairon, and C. Salomon, "High-accuracy measurement of the 87Rb ground-state hyperfine splitting in an atomic fountain," EPL (Europhysics Letters), vol. 45, no. 5, p. 558, 1999.

[59] "Fundamental Physiscs Constants," CODATA, 2018.

[60] E. Arimondo, M. Inguscio, and P. Violino, "Experimental determinations of the hyperfine structure in the alkali atoms," Rev. Mod. Phys., vol. 49, pp. 31–75, Jan 1977.

[61] E. Majorana, "Atomi orientati in campo magnetico variabile," Il Nuovo Cimento (1924-1942), vol. 9, no. 2, pp. 43–50, 1932.

[62] G. Colangelo, R. J. Sewell, N. Behbood, F. M. Ciurana, G. Triginer, and M. W. Mitchell, "Quantum atom–light interfaces in the Gaussian description for spin-1 systems," New Journal of Physics, vol. 15, no. 10, p. 103007, 2013.

[63] E. G. M. van Kempen, S. J. J. M. F. Kokkelmans, D. J. Heinzen, and B. J. Verhaar, "Interisotope Determination of Ultracold Rubidium Interactions from Three High-Precision Experiments," Phys. Rev. Lett., vol. 88, p. 093201, Feb 2002.

[64] N. N. Klausen, J. L. Bohn, and C. H. Greene, "Nature of spinor Bose-Einstein condensates in rubidium," Phys. Rev. A, vol. 64, p. 053602, Oct 2001.

[65] P. Gómez https://github.com/dspsandbox/GPE_SMA_F12.

[66] S. Tojo, T. Hayashi, T. Tanabe, T. Hirano, Y. Kawaguchi, H. Saito, and M. Ueda, "Spin-dependent inelastic collisions in spin-2 Bose-Einstein condensates," Phys. Rev. A, vol. 80, p. 042704, Oct 2009.

[67] G. Nogues, A. Rauschenbeutel, S. Osnaghi, M. Brune, J. Raimond, and S. Haroche, "Seeing a single photon without destroying it," Nature, vol. 400, no. 6741, p. 239, 1999.

[68] M. Koschorreck, M. Napolitano, B. Dubost, and M. W. Mitchell, "Sub-Projection-Noise Sensitivity in Broadband Atomic Magnetometry," Phys. Rev. Lett., vol. 104, p. 093602, Mar 2010.

[69] J. Guzman, G.-B. Jo, A. N. Wenz, K. W. Murch, C. K. Thomas, and D. M. Stamper-Kurn, "Long-time-scale dynamics of spin textures in a degenerate $F = 1$ ^{87}Rb spinor Bose gas," Phys. Rev. A, vol. 84, p. 063625, Dec 2011.

[70] U. Volz and H. Schmoranzer, "Precision lifetime measurements on alkali atoms and on helium by beam–gas–laser spectroscopy," Physica Scripta, vol. 1996, no. T65, p. 48, 1996.

[71] J. Ye, S. Swartz, P. Jungner, and J. L. Hall, "Hyperfine structure and absolute frequency of the 87 Rb 5P 3/2 state," Optics letters, vol. 21, no. 16, pp. 1280–1282, 1996.

[72] M. O. Scully and M. S. Zubairy, "Quantum optics," 1999.

[73] J. M. Geremia, J. K. Stockton, and H. Mabuchi, "Tensor polarizability and dispersive quantum measurement of multilevel atoms," Phys. Rev. A, vol. 73, p. 042112, Apr 2006.

[74] B. E. Saleh and M. C. Teich, "Fundamentals of photonics," John Wiley & Sons, 1991.

[75] F. Brennecke, T. Donner, S. Ritter, T. Bourdel, M. Köhl, and T. Esslinger, "Cavity QED with a Bose–Einstein condensate," Nature, vol. 450, no. 7167, p. 268, 2007.

[76] D. Budker, W. Gawlik, D. F. Kimball, S. M. Rochester, V. V. Yashchuk, and A. Weis, "Resonant nonlinear magneto-optical effects in atoms," Rev. Mod. Phys., vol. 74, pp. 1153–1201, Nov 2002.

[77] G. A. Smith, S. Chaudhury, A. Silberfarb, I. H. Deutsch, and P. S. Jessen, "Continuous weak measurement and nonlinear dynamics in a cold spin ensemble," Physical review letters, vol. 93, no. 16, p. 163602, 2004.

[78] M. Koschorreck, M. Napolitano, B. Dubost, and M. W. Mitchell, "Quantum Nondemolition Measurement of Large-Spin Ensembles by Dynamical Decoupling," Phys. Rev. Lett., vol. 105, p. 093602, Aug 2010.

[79] M. Koschorreck, "Generation of Spin Squeezing in an ensemble of Cold Rubidium 87," ICFO (UPC), 2011.

[80] R. Loudon, "The quantum theory of light," OUP Oxford, 2000.

[81] M. H. Levitt, "Composite pulses," Wiley Online Library, 2007.

[82] M. H. Levitt and R. Freeman, "NMR population inversion using a composite pulse," Journal of Magnetic Resonance (1969), vol. 33, no. 2, pp. 473–476, 1979.

[83] M. H. Levitt and R. Ernst, "Composite pulses constructed by a recursive expansion procedure," Journal of Magnetic Resonance (1969), vol. 55, no. 2, pp. 247–254, 1983.

[84] H. Imai, Y. Otsubo, and A. Morinaga, "Evaluation of the geometric phase of a two-level atom manipulated on the Bloch sphere using a time-domain atom interferometer," Phys. Rev. A, vol. 76, p. 012116, Jul 2007.

[85] C. L. Webb, R. M. Godun, G. S. Summy, M. K. Oberthaler, P. D. Featonby, C. J. Foot, and K. Burnett, "Measurement of Berry's phase using an atom interferometer," Phys. Rev. A, vol. 60, pp. R1783–R1786, Sep 1999.

[86] M. V. Berry, "Quantal phase factors accompanying adiabatic changes," Proceedings of the Royal Society of London. A. Mathematical and Physical Sciences, vol. 392, no. 1802, pp. 45–57, 1984.

[87] F. Bloch, "Nuclear Induction," Phys. Rev., vol. 70, pp. 460–474, Oct 1946.

[88] V. Natarajan, "Modern Atomic Physics," 2015.

[89] M. Born and V. Fock, "Beweis des Adiabatensatzes," Zeitschrift für Physik, vol. 51, no. 3-4, pp. 165–180, 1928.

[90] T. Kato, "On the adiabatic theorem of quantum mechanics," Journal of the Physical Society of Japan, vol. 5, no. 6, pp. 435–439, 1950.

[91] D. J. Griffiths and D. F. Schroeter, "Introduction to Quantum Mechanics," 2018.

[92] L. D. Landau, "Zur theorie der Energieubertragung ii," Z. Sowjetunion, vol. 2, pp. 46–51, 1932.

[93] C. Zener, "Non-adiabatic crossing of energy levels," Proceedings of the Royal Society of London. Series A, Containing Papers of a Mathematical and Physical Character, vol. 137, no. 833, pp. 696–702, 1932.

[94] A. Messiah, "Quantum mechanics: volume ii," North-Holland Publishing Company Amsterdam, 1962.

[95] S. Palacios Álvarez, "Single domain spinor Bose-Einstein condensate," ICFO (UPC), 2017.

[96] S. Coop, "Nonlinear behaviour of ultracold atoms in optical dipole traps," ICFO (UPC), 2018.

[97] A. Keshet and W. Ketterle, "A distributed, graphical user interface based, computer control system for atomic physics experiments," Review of Scientific Instruments, vol. 84, no. 1, p. 015105, 2013.

[98] A. Keshet, "A next-generation apparatus for lithium optical lattice experiments," Massachusetts Institute of Technology, 2012.

[99] E. Raab, M. Prentiss, A. Cable, S. Chu, and D. E. Pritchard, "Trapping of neutral sodium atoms with radiation pressure," Physical Review Letters, vol. 59, no. 23, p. 2631, 1987.

[100] P. D. Lett, R. N. Watts, C. I. Westbrook, W. D. Phillips, P. L. Gould, and H. J. Metcalf, "Observation of atoms laser cooled below the doppler limit," Physical review letters, vol. 61, no. 2, p. 169, 1988.

[101] J. Dalibard and C. Cohen-Tannoudji, "Laser cooling below the Doppler limit by polarization gradients: simple theoretical models," JOSA B, vol. 6, no. 11, pp. 2023–2045, 1989.

[102] W. Petrich, M. H. Anderson, J. R. Ensher, and E. A. Cornell, "Behavior of atoms in a compressed magneto-optical trap," JOSA B, vol. 11, no. 8, pp. 1332–1335, 1994.

[103] R. Grimm, M. Weidemüller, and Y. B. Ovchinnikov, "Optical dipole traps for neutral atoms," arXiv preprint physics/9902072, 1999.

[104] S. Coop, S. Palacios, P. Gomez, Y. N. M. de Escobar, T. Vanderbruggen, and M. W. Mitchell, "Floquet theory for atomic light-shift engineering with near-resonant polychromatic fields," Optics Express, vol. 25, no. 26, pp. 32550–32559, 2017.

[105] W. Gerlach and O. Stern, "Das magnetische Moment des Silberatoms," Zeitschrift für Physik, vol. 9, no. 1, pp. 353–355, 1922.

[106] M. O. Scully, W. E. Lamb Jr, and A. Barut, "Theory of the Stern-Gerlach apparatus," Foundations of Physics, vol. 17, no. 6, pp. 575–583, 1987.

[107] J. Luan, "Closed-loop control of magnetic fields for atomic physics experiments," Master's thesis, Universitat Politècnica de Catalunya, 2017.

[108] "AD9958 2-Channel, 500 MSPS DDS with 10-Bit DACs," Analog Devices, 2016. Rev. C.

[109] "Chipkit Max32 Online Reference Manual," Digilent.

[110] P. Gómez https://github.com/dspsandbox/AD9958-real-time-rf-source.

[111] "Evaluation Board for 2-Channel 500 MSPS DDS with 10-Bit DACs," Analog Devices, 2006. Rev. 0.

[112] P. Gómez https://github.com/dspsandbox/PWM.

[113] B. Naylor, M. Brewczyk, M. Gajda, O. Gorceix, E. Maréchal, L. Vernac, and B. Laburthe-Tolra, "Competition between Bose-Einstein Condensation and Spin Dynamics," Phys. Rev. Lett., vol. 117, p. 185302, Oct 2016.

[114] L. Sadler, J. Higbie, S. Leslie, M. Vengalattore, and D. Stamper-Kurn, "Spontaneous symmetry breaking in a quenched ferromagnetic spinor Bose–Einstein condensate," Nature, vol. 443, no. 7109, pp. 312–315, 2006.

[115] N. Navon, A. L. Gaunt, R. P. Smith, and Z. Hadzibabic, "Critical dynamics of spontaneous symmetry breaking in a homogeneous Bose gas," Science, vol. 347, no. 6218, pp. 167–170, 2015.

[116] V. Negnevitsky and L. D. Turner, "Wideband laser locking to an atomic reference with modulation transfer spectroscopy," Optics Express, vol. 21, no. 3, pp. 3103–3113, 2013.

[117] Y. N. M. de Escobar, S. P. Álvarez, S. Coop, T. Vanderbruggen, K. T. Kaczmarek, and M. W. Mitchell, "Absolute frequency references at 1529 and 1560 nm using modulation transfer spectroscopy," Optics Letters, vol. 40, no. 20, pp. 4731–4734, 2015.

[118] P. Gómez https://github.com/dspsandbox/offsetLock.

[119] F. M. Ciurana, G. Colangelo, R. J. Sewell, and M. W. Mitchell, "Real-time shot-noise-limited differential photodetection for atomic quantum control," Optics letters, vol. 41, no. 13, pp. 2946–2949, 2016.

[120] C. F. Gauß, "Intensitas vis magneticae terrestris ad mensuram absolutam revocata," 1832.

[121] G. D. Garland, "The contributions of Carl Friedrich Gauss to geomagnetism," Historia Mathematica, vol. 6, no. 1, pp. 5–29, 1979.

[122] M. C. Weisskopf, J. P. Carrico, H. Gould, E. Lipworth, and T. S. Stein, "Electric Dipole Moment of the Cesium Atom. A New Upper Limit to the Electric Dipole Moment of the Electron," Phys. Rev. Lett., vol. 21, pp. 1645–1648, Dec 1968.

[123] T. E. Chupp, P. Fierlinger, M. J. Ramsey-Musolf, and J. T. Singh, "Electric dipole moments of atoms, molecules, nuclei, and particles," Rev. Mod. Phys., vol. 91, p. 015001, Jan 2019.

[124] G. Vasilakis, J. M. Brown, T. W. Kornack, and M. V. Romalis, "Limits on New Long Range Nuclear Spin-Dependent Forces Set with a $\mathbf{K}-^3$He Comagnetometer," Phys. Rev. Lett., vol. 103, p. 261801, Dec 2009.

[125] L. Hunter, J. Gordon, S. Peck, D. Ang, and J.-F. Lin, "Using the Earth as a Polarized Electron Source to Search for Long-Range Spin-Spin Interactions," Science, vol. 339, no. 6122, pp. 928–932, 2013.

[126] M. Bulatowicz, R. Griffith, M. Larsen, J. Mirijanian, C. B. Fu, E. Smith, W. M. Snow, H. Yan, and T. G. Walker, "Laboratory Search for a Long-Range T-Odd, P-Odd Interaction from Axionlike Particles Using Dual-Species Nuclear Magnetic Resonance with Polarized ^{129}Xe and ^{131}Xe Gas," Phys. Rev. Lett., vol. 111, p. 102001, Sep 2013.

[127] K. Tullney, F. Allmendinger, M. Burghoff, W. Heil, S. Karpuk, W. Kilian, S. Knappe-Grüneberg, W. Müller, U. Schmidt, A. Schnabel, F. Seifert, Y. Sobolev, and L. Trahms, "Constraints on Spin-Dependent Short-Range Interaction between Nucleons," Phys. Rev. Lett., vol. 111, p. 100801, Sep 2013.

[128] J. Lee, A. Almasi, and M. Romalis, "Improved Limits on Spin-Mass Interactions," Phys. Rev. Lett., vol. 120, p. 161801, Apr 2018.

[129] B. J. Venema, P. K. Majumder, S. K. Lamoreaux, B. R. Heckel, and E. N. Fortson, "Search for a coupling of the Earth's gravitational field to nuclear spins in atomic mercury," Phys. Rev. Lett., vol. 68, pp. 135–138, Jan 1992.

[130] D. F. J. Kimball, I. Lacey, J. Valdez, J. Swiatlowski, C. Rios, R. Peregrina-Ramirez, C. Montcrieffe, J. Kremer, J. Dudley, and C. Sanchez, "A dual-isotope rubidium comagnetometer to search for anomalous long-range spin-mass (spin-gravity) couplings of the proton," Annalen der Physik, vol. 525, no. 7, pp. 514–528, 2013.

[131] D. F. Jackson Kimball, J. Dudley, Y. Li, D. Patel, and J. Valdez, "Constraints on long-range spin-gravity and monopole-dipole couplings of the proton," Phys. Rev. D, vol. 96, p. 075004, Oct 2017.

[132] S. K. Lamoreaux, J. P. Jacobs, B. R. Heckel, F. J. Raab, and E. N. Fortson, "New limits on spatial anisotropy from optically-pumped ^{201}Hg and ^{199}Hg," Phys. Rev. Lett., vol. 57, pp. 3125–3128, Dec 1986.

[133] D. Bear, R. E. Stoner, R. L. Walsworth, V. A. Kostelecký, and C. D. Lane, "Limit on Lorentz and CPT Violation of the Neutron Using a Two-Species Noble-Gas Maser," Phys. Rev. Lett., vol. 85, pp. 5038–5041, Dec 2000.

[134] F. Canè, D. Bear, D. F. Phillips, M. S. Rosen, C. L. Smallwood, R. E. Stoner, R. L. Walsworth, and V. A. Kostelecký, "Bound on Lorentz and CPT Violating Boost Effects for the Neutron," Phys. Rev. Lett., vol. 93, p. 230801, Nov 2004.

[135] J. M. Brown, S. J. Smullin, T. W. Kornack, and M. V. Romalis, "New Limit on Lorentz- and CPT-Violating Neutron Spin Interactions," Phys. Rev. Lett., vol. 105, p. 151604, Oct 2010.

[136] M. Smiciklas, J. M. Brown, L. W. Cheuk, S. J. Smullin, and M. V. Romalis, "New Test of Local Lorentz Invariance Using a ^{21}Ne–Rb–$\mathbf{K}$ Comagnetometer," Phys. Rev. Lett., vol. 107, p. 171604, Oct 2011.

[137] F. Allmendinger, W. Heil, S. Karpuk, W. Kilian, A. Scharth, U. Schmidt, A. Schnabel, Y. Sobolev, and K. Tullney, "New Limit on Lorentz-Invariance- and CPT-Violating Neutron Spin Interactions Using a Free-Spin-Precession ^{3}He-^{129}Xe Comagnetometer," Phys. Rev. Lett., vol. 112, p. 110801, Mar 2014.

[138] K. Woodman, P. Franks, and M. Richards, "The nuclear magnetic resonance gyroscope: a review," The Journal of Navigation, vol. 40, no. 3, pp. 366–384, 1987.

[139] T. W. Kornack, R. K. Ghosh, and M. V. Romalis, "Nuclear Spin Gyroscope Based on an Atomic Comagnetometer," Phys. Rev. Lett., vol. 95, p. 230801, Nov 2005.

[140] M. E. Limes, D. Sheng, and M. V. Romalis, "^{3}He–^{129}Xe Comagnetometery using ^{87}Rb Detection and Decoupling," Phys. Rev. Lett., vol. 120, p. 033401, Jan 2018.

[141] L. Jiang, W. Quan, R. Li, W. Fan, F. Liu, J. Qin, S. Wan, and J. Fang, "A parametrically modulated dual-axis atomic spin gyroscope," Applied Physics Letters, vol. 112, no. 5, p. 054103, 2018.

[142] T. W. Kornack and M. V. Romalis, "Dynamics of Two Overlapping Spin Ensembles Interacting by Spin Exchange," Phys. Rev. Lett., vol. 89, p. 253002, Dec 2002.

[143] D. Sheng, A. Kabcenell, and M. V. Romalis, "New Classes of Systematic Effects in Gas Spin Comagnetometers," Phys. Rev. Lett., vol. 113, p. 163002, Oct 2014.

[144] M. P. Ledbetter, S. Pustelny, D. Budker, M. V. Romalis, J. W. Blanchard, and A. Pines, "Liquid-State Nuclear Spin Comagnetometers," Phys. Rev. Lett., vol. 108, p. 243001, Jun 2012.

[145] T. Wu, J. W. Blanchard, D. F. Jackson Kimball, M. Jiang, and D. Budker, "Nuclear-Spin Comagnetometer Based on a Liquid of Identical Molecules," Phys. Rev. Lett., vol. 121, p. 023202, Jul 2018.

[146] H. Schmaljohann, M. Erhard, J. Kronjäger, M. Kottke, S. van Staa, L. Cacciapuoti, J. J. Arlt, K. Bongs, and K. Sengstock, "Dynamics of $F = 2$ Spinor Bose-Einstein Condensates," Phys. Rev. Lett., vol. 92, p. 040402, Jan 2004.

[147] D. W. Berry, H. M. Wiseman, and J. K. Breslin, "Optimal input states and feedback for interferometric phase estimation," Phys. Rev. A, vol. 63, p. 053804, Apr 2001.

[148] C. Gross, "Spin squeezing, entanglement and quantum metrology with Bose–Einstein condensates," Journal of Physics B: Atomic, Molecular and Optical Physics, vol. 45, no. 10, p. 103001, 2012.

[149] F. Gerbier, A. Widera, S. Fölling, O. Mandel, and I. Bloch, "Resonant control of spin dynamics in ultracold quantum gases by microwave dressing," Phys. Rev. A, vol. 73, p. 041602, Apr 2006.

[150] J. Lodewyck, P. G. Westergaard, and P. Lemonde, "Nondestructive measurement of the transition probability in a sr optical lattice clock," Phys. Rev. A, vol. 79, p. 061401, Jun 2009.

[151] M. H. Schleier-Smith, I. D. Leroux, and V. Vuletic, "States of an Ensemble of Two-Level Atoms with Reduced Quantum Uncertainty," Phys. Rev. Lett., vol. 104, p. 073604, Feb 2010.

[152] J. Lee, G. Vrijsen, I. Teper, O. Hosten, and M. A. Kasevich, "Many-atom–cavity QED system with homogeneous atom–cavity coupling," Opt. Lett., vol. 39, pp. 4005–4008, Jul 2014.

[153] J. E. Moody and F. Wilczek, "New macroscopic forces?," Phys. Rev. D, vol. 30, pp. 130–138, Jul 1984.

[154] G. Raffelt, "Limits on a *cp*-violating scalar axion-nucleon interaction," Phys. Rev. D, vol. 86, p. 015001, Jul 2012.

[155] A. K. Petukhov, G. Pignol, D. Jullien, and K. H. Andersen, "Polarized ^{3}He as a Probe for Short-Range Spin-Dependent Interactions," Phys. Rev. Lett., vol. 105, p. 170401, Oct 2010.

[156] A. P. Serebrov, O. Zimmer, P. Geltenbort, A. K. Fomin, S. N. Ivanov, E. A. Kolomensky, I. A. Krasnoshekova, M. S. Lasakov, V. M. Lobashev, A. N. Pirozhkov, V. E. Varlamov, A. V. Vasiliev, O. M. Zherebtsov, E. B. Aleksandrov, S. P. Dmitriev, and N. A. Dovator, "Search for macroscopic CP violating forces using a neutron EDM spectrometer," JETP Letters, vol. 91, no. 1, pp. 6–10, 2010.

[157] M.-S. Chang, C. Hamley, M. Barrett, J. Sauer, K. Fortier, W. Zhang, L. You, and M. Chapman, "Observation of spinor dynamics in optically trapped Rb 87 Bose-Einstein condensates," Physical review letters, vol. 92, no. 14, p. 140403, 2004.

[158] D. Jacob, L. Shao, V. Corre, T. Zibold, L. De Sarlo, E. Mimoun, J. Dalibard, and F. Gerbier, "Phase diagram of spin-1 antiferromagnetic Bose-Einstein condensates," Physical Review A, vol. 86, no. 6, p. 061601, 2012.

[159] M. Vengalattore, J. Guzman, S. Leslie, F. Serwane, and D. Stamper-Kurn, "Periodic spin textures in a degenerate f= 1 rb 87 spinor Bose gas," Physical Review A, vol. 81, no. 5, p. 053612, 2010.

[160] M. Scherer, B. Lücke, J. Peise, G. Gebreyesus, F. Deuretzbacher, W. Ertmer, L. Santos, C. Klempt, J. J. Arlt, et al., "Spontaneous symmetry breaking in spinor Bose-Einstein condensates," Physical Review A, vol. 88, no. 5, p. 053624, 2013.

[161] S. De, D. Campbell, R. Price, A. Putra, B. M. Anderson, and I. Spielman, "Quenched binary Bose-Einstein condensates: Spin-domain formation and coarsening," Physical Review A, vol. 89, no. 3, p. 033631, 2014.

[162] J.-y. Choi, W. J. Kwon, and Y.-i. Shin, "Observation of topologically stable 2D skyrmions in an antiferromagnetic spinor Bose-Einstein condensate," Physical review letters, vol. 108, no. 3, p. 035301, 2012.

[163] M. W. Ray, E. Ruokokoski, S. Kandel, M. Möttönen, and D. Hall, "Observation of Dirac monopoles in a synthetic magnetic field," Nature, vol. 505, no. 7485, p. 657, 2014.

[164] S. B. Papp, J. M. Pino, and C. E. Wieman, "Tunable Miscibility in a Dual-Species Bose-Einstein Condensate," Phys. Rev. Lett., vol. 101, p. 040402, Jul 2008.

[165] G. Thalhammer, G. Barontini, L. De Sarlo, J. Catani, F. Minardi, and M. Inguscio, "Double Species Bose-Einstein Condensate with Tunable Interspecies Interactions," Phys. Rev. Lett., vol. 100, p. 210402, May 2008.

[166] D. J. McCarron, H. W. Cho, D. L. Jenkin, M. P. Köppinger, and S. L. Cornish, "Dual-species Bose-Einstein condensate of ^{87}Rb and ^{133}Cs," Phys. Rev. A, vol. 84, p. 011603, Jul 2011.

[167] W. Muessel, H. Strobel, D. Linnemann, D. B. Hume, and M. K. Oberthaler, "Scalable Spin Squeezing for Quantum-Enhanced Magnetometry with Bose-Einstein Condensates," Phys. Rev. Lett., vol. 113, p. 103004, Sep 2014.

[168] W. Muessel, H. Strobel, D. Linnemann, T. Zibold, B. Juliá-Díaz, and M. K. Oberthaler, "Twist-and-turn spin squeezing in Bose-Einstein condensates," Phys. Rev. A, vol. 92, p. 023603, Aug 2015.

[169] R. Schmied, J.-D. Bancal, B. Allard, M. Fadel, V. Scarani, P. Treutlein, and N. Sangouard, "Bell correlations in a Bose-Einstein condensate," Science, vol. 352, no. 6284, pp. 441–444, 2016.

[170] M. Fadel, T. Zibold, B. Décamps, and P. Treutlein, "Spatial entanglement patterns and Einstein-Podolsky-Rosen steering in Bose-Einstein condensates," Science, vol. 360, no. 6387, pp. 409–413, 2018.

[171] F. Anders, L. Pezzè, A. Smerzi, and C. Klempt, "Phase magnification by two-axis countertwisting for detection-noise robust interferometry," Phys. Rev. A, vol. 97, p. 043813, Apr 2018.

[172] W. Muessel, H. Strobel, M. Joos, E. Nicklas, I. Stroescu, J. Tomkovič, D. B. Hume, and M. K. Oberthaler, "Optimized absorption imaging of mesoscopic atomic clouds," Applied Physics B, vol. 113, pp. 69–73, Oct 2013.

[173] P. Altin, G. McDonald, D. Doering, J. Debs, T. Barter, J. Close, N. Robins, S. Haine, T. Hanna, and R. Anderson, "Optically trapped atom interferometry using the clock transition of large ^{87}Rb Bose–Einstein condensates," New Journal of Physics, vol. 13, no. 6, p. 065020, 2011.

[174] Y.-Q. Zou, B. Bakkali-Hassani, C. Maury, E. Le Cerf, S. Nascimbene, J. Dalibard, and J. Beugnon, "Magnetic Dipolar Interaction between Hyperfine Clock States in a Planar Alkali Bose Gas," Phys. Rev. Lett., vol. 125, p. 233604, Dec 2020.

[175] M. Gajdacz, A. J. Hilliard, M. A. Kristensen, P. L. Pedersen, C. Klempt, J. J. Arlt, and J. F. Sherson, "Preparation of Ultracold Atom Clouds at the Shot Noise Level," Phys. Rev. Lett., vol. 117, p. 073604, Aug 2016.

[176] F. Martin Ciurana, G. Colangelo, L. Slodička, R. J. Sewell, and M. W. Mitchell, "Entanglement-Enhanced Radio-Frequency Field Detection and Waveform Sensing," Phys. Rev. Lett., vol. 119, p. 043603, Jul 2017.

[177] D. Schrand, "Cross-Talk Compensation Using Matrix Methods," Sensors and Transducers Journal, vol. 79, p. 1157, May 2007.

[178] G. Baym and C. J. Pethick, "Ground-State Properties of Magnetically Trapped Bose-Condensed Rubidium Gas," Phys. Rev. Lett., vol. 76, pp. 6–9, Jan 1996.

[179] F. Dalfovo, L. Pitaevskii, and S. Stringari, "Order parameter at the boundary of a trapped Bose gas," Phys. Rev. A, vol. 54, pp. 4213–4217, Nov 1996.

[180] E. Lundh, C. J. Pethick, and H. Smith, "Zero-temperature properties of a trapped Bose-condensed gas: Beyond the Thomas-Fermi approximation," Phys. Rev. A, vol. 55, pp. 2126–2131, Mar 1997.

[181] H. Saito, Y. Kawaguchi, and M. Ueda, "Topological defect formation in a quenched ferromagnetic Bose-Einstein condensates," Phys. Rev. A, vol. 75, p. 013621, Jan 2007.

[182] A. A. Norrie, R. J. Ballagh, and C. W. Gardiner, "Quantum turbulence and correlations in Bose-Einstein condensate collisions," Phys. Rev. A, vol. 73, p. 043617, Apr 2006.

Acknowledgements

The last lines of this thesis are devoted to the many people I owe a sincere *thank you*.

I want to express my gratitude to Morgan, who gave me (as a 3rd year undergraduate student) the opportunity to work for a summer in a Quantum Optics laboratory. That experience turned out to be very persuasive and I rapidly left behind the original idea of becoming a theoretical physicist. In fact, a few years later I became a PhD student in his group and started to learn about the beauties, the open questions, the magic, the patience and management of frustration that an experiment in ultracold atoms requires. Since then, Morgan helped me to think critically and he gave me the freedom to try out new ideas, to make mistakes and to expand my knowledge even beyond the scope of this thesis. Examples of the latter are multiple hardware programming projects, which led to a dedicated microcontroller or FPGA in almost every part of the experimental setup (including the PhD hats of my former colleagues). I also want to thank him for the chance of working on this manuscript while pursuing a career in Industry and the many detailed comments and corrections I got during this time.

Within Morgan's group, I specially want to thank Silvana, who owns the credit for our all-optical SBEC. She patiently taught me how to operate the experimental setup while playing *Sex Over the Phone*. Also a big thank you to Simon, a firm supporter of the do-it-yourself approach and very skilled in analogue and digital electronics. He enjoys listening to Solomun's *Boiler Room DJ Set* and Nightmares on Wax's *Sunset Set*. Chiara joined the group a few years later than me, but I am very happy about her help in the acquisition of the data of this thesis, her systematic mindset and for forcing me to properly round our experimental data. She typically listens to classical music and gives excellent culinary recommendations. Regarding our postdocs, I am indebted to Ferran. He helped me defining the roadmap for [52, 53], fed me with cookies every morning and guided me through the feared *Valley of Shit*, the typical state of mind during the second half of a PhD. Thank you Martijn and Daniel for your help at the beginning and at the end of my time in Morgan's group.

On behalf of ICFO staff, I am grateful to José Carlos and the electronic workshop for their help with analogue electronics and their guidance during my first FPGA projects. Also Xavi and the mechanical workshop were extremely responsive and it was always fun to chat with them. The purchasing unit, human resources and academic affairs took care that my PhD was not an administrative nightmare.

Within ICFO and on a more personal note, I want to mention my friends Ferran, Silvana, Roland, Lisa, Miquel, Juan and Míriam. We spent countless

beers and funny evenings together, which I am already missing.

For my time at Quside, I thank Carlos and José. I appreciated the flexibility and dedicated time to work on my thesis. I am very thankful to Marc and Xio for becoming part of Keysight's Quantum Solution Team while writing the last chapters of this manuscript.

Finally, I want to thank my family. My mother, my father, my sister and my grandparents have always supported me along this journey. Thank you for your love, for a childhood full of curiosity and inventions, and for planting the seeds of my passion for Physics. Josep, thank you for always being there and for bringing me back to Barcelona. Carla, probably you are the only nurse that knows what a SBEC Comagnetometer is. Thank you for the notes and stickers every morning, for your patience and support during the last years and for showing me the little things in life that really matter.